

Numerical Simulation of Multiphase Flows Under
Electrohydrodynamic Effects

by

Amin Rahmat

Submitted to
the Graduate School of Engineering and Natural Sciences
in partial fulfillment of the requirements for the degree of
Doctor of Philosophy

Sabanci University

August 2017

Numerical Simulation of Multiphase Flows under the Electrohydrodynamics
Effects

APPROVED BY:

Assoc. Prof. Dr. Mehmet Yildiz
(Thesis Supervisor)



Assoc. Prof. Dr. Bahattin Koc



Asst. Prof. Dr. Eralp Demir



Prof. Dr. Afzal Suleman



Prof. Dr. Omer Goren



Prof. Dr. Ali Kosar



DATE OF APPROVAL: 01/08/2017

Numerical Simulation of Multiphase Flows Under Electrohydrodynamic Effects

Amin Rahmat

Ph.D. Dissertation, August 2017

Thesis Supervisor: Prof. Dr. Mehmet Yildiz

Multiphase flow problems are one of the main categories of fluid dynamics problems with a broad range of applications in industrial practices. Thus, it is crucial to control multiphase flow problems to maintain desirable flow regimes in those industrial applications. The electrohydrodynamics can be used to control multiphase flow problems due to its simplicity, wide range of applicability and its high precision controllability. One of possible approaches to investigate the influence of electrohydrodynamics on multiphase flow problems is to utilize numerical methods for simulating the interaction between electric and hydrodynamic forces in complex multiphase systems. In this thesis, the numerical investigations of electrohydrodynamics effects on multiphase flow problems are carried out by developing the Smoothed Particle Hydrodynamics (SPH) method, as well as extending a commercial Computational Fluid Dynamics (CFD) software. The simulation of multiphase flows and electrohydrodynamics is implemented by the Continuum Surface Force (CSF) and leaky dielectric models, respectively. The SPH method is a Lagrangian particle-based mesh-less method which can simulate interfacial multiphase flows with no additional computational costs. The in-house SPH code is initially validated by comparing present numerical results with those of Laplace equation for the implementation of surface tension, and with analytical solutions of Taylor and Feng theories for the deformation of a stationary droplet in the presence of electric field. Moreover, the method is extensively validated for each of the following problems with available numerical, analytical and experimental data in literature. The first problem is the Rayleigh-Taylor Instability (RTI) that allows performing a phenomenological study on a fundamental multiphase flow problem. The influence of various electrohydrodynamic forces is investigated by comparing the role of Coulomb and polarization forces. Then, the method is extended to bubble rising of an oil/water system by investigating the influence of electric forces on the deformation of a rising bubble and its rise velocity. The SPH method is also used to simulate the electro-coalescence of binary droplets. Thus, the SPH

method is extended for the simulation of droplet coalescence by developing a multiphase algorithm based on the lubrication theory and film drainage model. The algorithm is used to simulate the head-on and head-off coalescence of approaching binary droplets as well as the electro-coalescence of stationary droplets. The second approach to the simulation of multiphase flows under the electrohydrodynamic effects is the development of a commercial CFD software, the ANSYS-Fluent. The software is extended by writing complex User Defined Functions (UDFs) for the simulation of electrohydrodynamics. In addition to the initial comparison of the numerical tool with available numerical and analytical results for the electrohydrodynamic deformation of a suspended droplet, the numerical tool is extensively validated with available data in literature for various test-cases of the following problems. The developed ANSYS-Fluent code is used to simulate the bubble rising of an air/water system for the formation of toroidal rising bubbles by investigating the combined effects of domain confinement and electrohydrodynamics. Finally, the electro-jet printing which is an industrial scale problem is simulated for variations of different dimensionless parameters to provide guidelines for the design of electro-jet printing setups.

Keywords: Numerical simulations, Computational Fluid Dynamics (CFD), The Smoothed Particle Hydrodynamics method, Multiphase flows, The Electrohydrodynamics, The SPH method, The EHD, Bubble dynamics.

Elektrohidrodinamik Etkiler Altında Çok Fazlı Akımların Sayısal Simülasyonu

Amin Rahmat

Doctora Tez, Ağustos 2017

Tez Danışmanı: Prof. Dr. Mehmet Yıldız

Akışkanlar dinamiğinin başlıca konularından biri olan çok fazlı akış problemleri endüstriyel uygulamalarda geniş bir yelpazeye sahiptir. Bu nedenle, endüstriyel uygulamalarda istenilen akış rejimini sürdürebilmek için çok fazlı akış problemi kontrol etmek önem arz etmektedir. Elektrohidrodinamik, kolaylığı, çeşitli sayıda uygulama alanı ve yüksek hassasiyette kontrol özelliği nedeniyle çok fazlı akış problemlerini kontrol etmek için kullanılır. Elektrohidrodinamiğin çok fazlı akış problemleri üzerindeki etkisini araştırmak için olası yaklaşımlardan biri ise, karmaşık çok fazlı sistemlerde elektrik ve hidrodinamik kuvvetler arasındaki etkileşimi simüle etmek için kullanılan sayısal yöntemlerdir. Bu tezde, çok fazlı akış problemleri üzerindeki elektrohidrodinamik etkilerin sayısal incelemeleri, Düzleştirilmiş Tanecik Hidrodinamiği (SPH) yönteminin geliştirilmesi ve Hesaplamalı Akışkanlar Dinamiğinin (CFD) ticari yazılımından yararlanılarak yapılan çalışmalardan bahsedilmektedir. çok fazlı akışların ve elektrohidrodinamik simülasyonları sırasıyla Sürekli Yüzey Kuvveti (CSF) ve sızdıran dielektrik modeller tarafından gerçekleştirilmiştir. Düzleştirilmiş Tanecik Hidrodinamiği (SPH) yöntemi, ek hesaplama maliyeti olmaksızın arayüzler arası çok fazlı akışları simüle edebilen Lagrangian parçacık tabanlı, ağ-içermeyen bir yöntemdir. Mevcut Düzleştirilmiş Tanecik Hidrodinamiği (SPH) kodu ile yüzey geriliminin uygulanması için mevcut sayısal sonuçlar Laplace denklemi ile karşılaştırılmış ve elektrik alan varlığında durağan damlacık deformasyonu için Taylor ve Feng teorilerinin analitik çözümleri ile birlikte doğrulanmıştır. Ek olarak, yöntem, literatürdeki mevcut sayısal, analitik ve deneysel verilere dayanan aşağıdaki problemlerin her biri için geçerlidir. İlk problem, çok fazlı bir akış problemi üzerinde fenomenolojik bir çalışmanın yapılmasına izin veren Rayleigh-Taylor Kararsızlığıdır (RTI). Coulomb ve polarizasyon kuvvetlerinin rolü karşılaştırılarak çeşitli elektrohidrodinamik kuvvetlerin etkisi araştırılmıştır. Daha sonra, yağ/su sistemindeki kabarcık yükselişi sırasında elektrik kuvvetlerinin yükselen bir kabarcığın deformasyon ve

yükselme hızı üzerindeki etkisi araştırılmıştır. Düzleştirilmiş Tanecik Hidrodinamiği (SPH) yöntemi, ikili damlacıkların elektro-birleşmesini simüle etmek için de kullanılır. Bu nedenle, Düzleştirilmiş Tanecik Hidrodinamiği metodu, yağlama kuramı ve film drenaj modeline dayalı çok fazlı bir algoritma geliştirerek ikili kaynaşmanın simülasyonu için genişletilmiştir. Algoritma, duran damlacıkların elektro-birleşmesinin yanı sıra, yaklaşan ikili damlacığın doğrudan ve başaşağı kaynaşmasını simüle etmek için kullanılmıştır. Elektrohidrodinamik etkiler altında çok fazlı akış simülasyonuna ikinci yaklaşım ise, ticari bir hesaplamalı akışkanlar dinamiği yazılımı olan ANSYS-Fluent' in geliştirilmesidir. Yazılım, elektrohidrodinamik simülasyonu için karmaşık Kullanıcı Tanımlı Fonksiyonlar (UDFs) yazılarak genişletilmiştir. Bir asılı damlacığın elektrohidrodinamik deformasyonu için sayısal aracın mevcut sayısal ve analitik sonuçlarla karşılaştırılmasına ek olarak, sayısal araç aşağıdaki problemlerin farklı vakaları için literatürdeki mevcut verilerle geniş çapta doğrulanmıştır. Geliştirilmiş olan ANSYS-Fluent kodu, alan kısıtlamasının ve elektrohidrodinamiğin birleşmiş etkilerini inceleyerek halka şeklinde yükselen kabarcıkların oluşumu için hava/su sisteminin kabarcık yükselişini simüle etmek için kullanılmıştır. Son olarak, endüstriyel ölçekli bir problem olan elektro-jet baskı, farklı boyutsuz parametrelerin varyasyonları için simüle edilerek, elektro-jet baskı sistemlerinin tasarımı için kılavuz bilgiler sağlanmıştır.

Anahtar kelimeler: Sayısal simülasyonlar, Hesaplamalı Akışkanlar Dinamiği (CFD), Düzleştirilmiş Parçacık Hidrodinamiği yöntemi, çok Fazlı Akımlar, Elektrohidrodinamik, SPH Metodu, EHD, Kabarcık Dinamiği.

Acknowledgements:

I believe it is impossible to accomplish Ph.D. studies without the help and support from other people. Thus, I would like to express my gratitude towards:

- my supervisor, Professor Dr. Mehmet Yildiz, for his exquisite pieces of advice and professional support,
- thesis jury members for their valuable comments and suggestions to improve the quality of this dissertation,
- all my friends in Sabanci University, especially my seniors and group members for their technical cooperation,
- Sabanci University for providing an international academic environment and financial support,
- my parents and my brother for their precious and magnificent support and eternal love, and
- my wife, Shiva, for her fascinating patience, emotional support and endless love.

Contents

List of Figures	ix
List of Tables	xiv
Nomenclature	xv
1 Introduction	1
1.1 Multiphase Flows	1
1.2 Electrohydrodynamics	2
1.3 Numerical Simulation of Multiphase Flows	4
1.4 State-Of-The-Art	5
1.4.1 The Smoothed Particle Hydrodynamics (SPH) method	6
1.4.2 ANSYS Fluent	8
1.4.3 The SPH method versus the ANSYS Fluent	8
2 Governing Equations	10
2.1 Mechanical balance laws of continua	10
2.2 Electrohydrodynamics Balance Laws	11
2.3 Leaky dielectric model	14
3 SPH Principles	16
3.1 The SPH Principles	16
3.2 Numerical Algorithm of the In-house Code	20
3.3 Numerical Algorithm of the ANSYS-Fluent	22
4 Numerical Validation	23
4.1 Numerical Validation	23
4.1.1 Validation of the in-house SPH code	23
4.1.1.1 Validation of surface tension force	24
4.1.1.2 Validation of electrohydrodynamics	25
4.1.2 EHD validation of the Fluent code	27
5 Results	29
5.1 Rayleigh-Taylor Instability (RTI)	29
5.1.1 Problem Set-up	30
5.1.2 The Comparison of Interfacial Forces	32

5.1.3	The Effect of the applied electric field on the instability . . .	35
5.1.4	Effect of Electric Permittivity Variations	38
5.1.5	Effect of Electric Field Strength Variations	42
5.2	Bubble rising	46
5.2.1	Bubble rising of an oil-water system	48
5.2.1.1	Problem set-up	48
5.2.1.2	Effect of Electro-capillary number	51
5.2.1.3	Effect of Reynolds number	54
5.2.1.4	Effect of Bond number	55
5.2.1.5	The EHD interaction between a pair of rising bubble	58
5.2.2	Bubble rising of an air-water system	61
5.2.2.1	Problem set-up	61
5.2.2.2	Effect of Electro-capillary number	65
5.2.2.3	Effect of confinement ratio	69
5.2.2.4	The combined effect of confinement ratio and Electro- capillary number	72
5.3	Droplet coalescence	75
5.3.1	Lubrication theory and film drainage model	77
5.3.2	Problem Set-up	79
5.3.3	Binary droplet coalescence	83
5.3.3.1	Head-on coalescence	84
5.3.3.2	Head-off coalescence	87
5.3.3.3	Electro-coalescence	89
5.4	Electro-jet printing	93
5.4.1	Problem set-up	95
5.4.2	The EHD jet printing process	98
5.4.3	Effect of Reynolds number	99
5.4.4	Effect of Electro-Weber number	100
5.4.5	Unstable regimes	100
6	Conclusion	104
6.1	Concluding remarks	104
6.2	Future works	110
	Bibliography	112

List of Figures

4.1	The comparison of numerically computed pressure jumps as a function of surface tension coefficient with that calculated by the analytical equation, namely, Laplace's law.	24
4.2	Comparison the deformation index of present numerical results (square marks) with Lin <i>et al.</i> [42] (circle marks) and Taylor's theory [82] (dashed and solid lines) for the deformation of a neutrally buoyant bubble; The parameters are set to $\mathcal{D} = 1$, $\mathcal{V} = 1$, $\mathcal{C} = 5$, and $\text{Ec} = 0.4$	27
5.1	Initial condition used for simulations. (left) Whole domain; solid line shows the intended interface as defined in (5.1); heavy fluid on top, light fluid at the bottom. (right) Close up view of the portion included between the dashed lines on the right showing the initial particle positions in the vicinity of the interface. Solid line shows the intended interface profile while dashed line is the acquired interface profile calculated as 0.5 level contour of the color function.	31
5.2	Comparison of components of the resultant electric force at $t = 4.74$; (left column) case B; (right column) case C. The left sub-column shows polarization forces while the right sub-column gives electric field forces. The direction and magnitude of the forces are respectively indicated by arrows and filled contour levels.	33
5.3	Comparison of the resultant electric force and surface tension force at $t = 4.74$; (left column) case B; (right column) case C. The left sub-column shows the resultant electric force while the right sub-column gives surface tension forces. The direction and magnitude of the forces are respectively indicated by arrows and filled contour levels.	33
5.4	The evolution of the instability, represented by the 0.5 level contour of color function, for (top row) case A; (middle row) case B; (bottom row) case C. From left to right, snapshots are taken at spike positions of $h_s = 1.66, 1.32, 0.98, 0.64$ and 0.30	36
5.5	Normalized distance versus time for cases A, B and C (table 5.2); (top) spike tip position; (bottom) bubble tip position.	37
5.6	Snapshots of 0.5 level contour of color function at $h_s = 0.3$ for (top row) D series; (bottom row) E series. From left to right, snapshots correspond to case numbers 1 through 5 as set in table 5.3.	40
5.7	Normalized distance versus time for cases D-1, D-3 and D-5 (table 5.3); (top) spike tip position; (bottom) bubble tip position.	41

5.8	Normalized distance versus time for cases E-1, E-3 and E-5 (table 5.3); (top) spike tip position; (bottom) bubble tip position.	42
5.9	The evolution of the instability for different electric field strength, which is shown for $h_s = 0.3$ for all cases. The sub-figures at the top row represent the cases F-1 to F-5 of table 5.3, and the sub-figures at the bottom row represents the case G-1 to G-5 of the same table.	44
5.10	Normalized distance versus time for cases F-1, F-3 and F-5 (table 5.4); (top) spike tip position; (bottom) bubble tip position.	45
5.11	Normalized distance versus time for cases G-1, G-3, and G-5 (table 5.4); (top) spike tip position; (bottom) bubble tip position.	45
5.12	Schematic of the test case.	49
5.13	The comparison of the bubble shape and centroid velocities for non-electrified (a,c) and electrified (b,d) cases of the present study with Mahlmann <i>et al.</i> [21] where the solid line corresponds to the results of the current study.	50
5.14	The temporal evolution of centroid positions and velocities of the validation test case with dimensionless parameters of $Re = 400$, $Bo = 12$ and $Ec = 5$ for six different particle resolutions.	50
5.15	Bubble shapes and velocity streamlines for non-electrified and electrified cases at five early instants of the rising; The upper row shows the non-electrified case $Ec = 0$ at (a) $t = 0.4$, (b) $t = 10$, (c) $t = 5$, (d) $t = 9$ and (e) $t = 13$ while the bottom one represents the electrified case ERB , at (f) $t = 0.4$, (g) $t = 1$, (h) $t = 2$, (i) $t = 2.4$ and (j) $t = 4$	52
5.16	The temporal variation of aspect ratio A_r as a function of electrical capillary number Ec for six test cases.	53
5.17	Temporal variations of centroid velocity v_c at left and bottom velocity v_b at right for different electrical capillary numbers Ec	54
5.18	Temporal variation of aspect ratio A_r for four different Reynolds numbers.	55
5.19	Temporal variations of centroid velocities v_c at left and bottom velocity v_b at right for four different Reynolds numbers.	55
5.20	Temporal variations of aspect ratio A_r for six different Bond numbers.	56
5.21	Temporal variations of centroid velocities v_c at left and bottom velocity v_b at right for six different Bond numbers.	57
5.22	Bubble shape and velocity streamlines at $y = 7.5$ for five various cases; (a) $Ec = 1$, (b) ERB , (c) $Re = 100$, (d) $Bo = 4$, and (e) $Ec = 1$	57

5.23	The interaction of two bubbles with $\theta = 0$ (vertically in-line) for four cases of $P01$, $P02$, $P03$, and $P04$; The left sub-figure shows the distance between bubble centroids for these cases versus the centroid position of the upper bubble; the solid lines indicate the moments in which the bubbles are not merged and dash lines show the merged instances. The right sub-figure shows the difference between upper to lower centroid velocities during evolution time for two cases of $P03$ and $P04$	59
5.24	The interaction of two bubbles with $\theta = \pi/4$; The bubble interface is shown for three different instants of the rising motion, namely, $t = 0$, $t = 4$ and $t = 8$, for $P11$ at the left and for $P12$ at the right.	60
5.25	The center to center distance of bubbles (left) and corresponding angle (θ) (right) for two cases of $P11$ and $P12$	60
5.26	Schematic of the test case.	62
5.27	The grid resolution study for the test case VT3 from table 5.7 for bubble shape (at left) and vertical rise velocity (at right), employing four different resolutions of $MR1 = 24\chi_p$, $MR2 = 32\chi_p$, $MR3 = 48\chi_p$, and $MR14 = 64\chi_p$ where $n\chi_p$ indicates the number of grids per initial bubble diameter.	64
5.28	The history of bubble shapes at $t = 0, 1, 2, 3, 4, 5$ in confinement ratio of $Cr = 2$ for variations of Electro-capillary number; (a) $Ec = 1.0$, (b) $Ec = 1.5$, (c) $Ec = 2.0$, (d) $Ec = 2.5$	65
5.29	The electric forces per unit volume normalized by $\varepsilon_f E_\infty^2/d$ shown by vector field (on the left half) and contours (on the right half) on the interface of the bubble at $t = 1$ in confinement ratio of $Cr = 2$ and for (a) $Ec = 1.0$, (b) $Ec = 1.5$, (c) $Ec = 2.0$, (d) $Ec = 2.5$; In order to compare force magnitudes, the electric field intensity for normalizing the forces E_n is taken equal to 1.	66
5.30	The vertical rise velocity versus time for constant confinement ratio $Cr = 2$ at different Electro-capillary ratios, $Ec = 1.0, 1.5, 2.0$ and 2.5 .	67
5.31	The velocity streamlines and bubble shapes for confinement ratio for $Cr = 2$ and different Electro-capillary numbers; (a) $Ec = 1.0$, (b) $Ec = 1.5$, (c) $Ec = 2.0$, (d) $Ec = 2.5$ and (e) their corresponding wall shear stress; The bubbles are shown in a half domain for the moment when their centroids are at $z = 5$	68
5.32	The history of bubble shapes at $t = 0, 1, 2, 3, 4, 5$ in Electro-capillary number of $Ec = 1.35$ for various confinement ratios; (a) $Cr = 2$, (b) $Cr = 3$, (c) $Cr = 4$, (d) $Cr = 5$	69
5.33	The vertical rise velocity versus time for constant Electro-capillary numbers $Ec = 1.35$ at different confinement ratios, $Cr = 2, 3, 4$ and 5 .	70
5.34	The velocity streamlines and bubble shapes for Electro-capillary number of $Ec = 2.5$ and different confinement ratios; (a) $Cr = 2$, (b) $Cr = 3$, (c) $Cr = 4$, (d) $Cr = 5$ and (e) their corresponding wall shear stress; The bubbles are shown in a half domain for the moment when their centroids are at $z = 5$	71

5.35	Three-dimensional demonstration of terminal bubble shape for variations of Electro-capillary numbers and confinement ratios.	72
5.36	The map of the test cases for variations of Electro-capillary numbers and confinement ratios simulated in present study; the circle marks indicate the cases wherein the rising bubble remains non-pierced while the plus marks represent the pierced cases. The red solid line indicates the transition region where the bubble pierces.	73
5.37	Variations of Terminal Reynolds number as a function of Electro-capillary number for different confinement ratios.	74
5.38	The variations of normalized diameter of the bubble ring D_r in time for CE1 [Cr = 5, Ec = 2.5], CE2 [Cr = 5, Ec = 2], CE3 [Cr = 5, Ec = 1.5], CE4 [Cr = 4, Ec = 2.5], CE5 [Cr = 3, Ec = 2.5], and CE6 [Cr = 2, Ec = 2.5].	74
5.39	The schematic representation of bubble position and	77
5.40	Schematic of the test case in sub-figure (a) and the schematic of the initial particle positions for droplets and their surrounding fluid (not full domain representation) presented with different colors in sub-figure (b).	80
5.41	The comparison of the results with experimental findings of Qian <i>et al.</i> [121] and numerical findings from a FVM tool for simulation conditions [We = 0.2, Re = 14.8, $\beta = 0.20$] at different simulation times; (a) present numerical result, (b) experimental findings, (c) FVM results.	81
5.42	The comparison of the results with experimental findings of Qian <i>et al.</i> [121] and numerical findings from a FVM tool for simulation conditions [We = 15.2, Re = 139.8, $\beta = 0.08$] at different simulation times; (a) present numerical result, (b) experimental findings, (c) FVM results.	82
5.43	The particle resolution study for VT-I (sub-figures a and b) at $t = 0.1$ and $t = 0.2$, and VT-II (sub-figures c and d) at $t = 1.0$ and $t = 3.0$ for four different resolutions; $\Pi = 40$ x/d (green solid line), $\Pi = 50$ x/d (red solid line), $\Pi = 60$ x/d (blue solid line) and $\Pi = 70$ x/d (black solid line)	82
5.44	SPH particles of a head-on test-case with the simulation conditions of [We = 5.0, Re = 100, $\mathcal{D} = 1000$, $\mathcal{V} = 100$] at two different times after coalescence for the original results (without the drainage mode) in column A, and the modified model (including the drainage model) in column B; Magenta, green and black points represent upper droplet, lower droplet and surrounding fluid particles respectively.	84
5.45	The evolution of head-on coalescence ($\beta = 0$) at different simulation times; The Reynolds number is set to Re = 100 and Weber number increase from left to right columns by We = 2.0, We = 5.0, We = 20.0 and We = 30.0.	85
5.46	The variation of deformation index of coalesced droplets in time for different head-on cases shown in table 5.8.	86

5.47	The evolution of head-off coalescence ($\beta = 0$) at different simulation times for four test-cases from table 5.9; The Reynolds and Weber numbers are set to $Re = 100$ and $We = 10.0$, and the impact parameter is increased from left to right, $\beta = 0.2$, $\beta = 0.4$, $\beta = 0.6$ and $\beta = 0.8$	88
5.48	The time evolution of droplet interface for electro-coalescence for two different cases; (A) an oblate deformation case of droplets corresponding to edc-1 of table 5.10, and (B) a prolate deformation case corresponding to edc-2 of table 5.10.	90
5.49	Droplet interface of edc-1 and edc-2 test-cases from table 5.10; velocity vectors and streamlines of particles are shown by black arrows and red lines in the left and right halves of the figure, respectively, the upper row (sub-figures A and C) represents the droplets before the coalescence and bottom row (sub-figures B and D) represents the coalesced droplet after coalescence.	91
5.50	Comparison of droplet distance \mathcal{L} and droplet center to center distance l^* for different oblate deformation cases edc-1, edc-3 and edc-4 of table 5.10.	92
5.51	Comparison of droplet distance l^* for prolate deformation coalescence cases of table 5.10.	93
5.52	The schematic figure of the solution domain.	95
5.53	The grid resolution study for simulation condition of [$Re = 0.02$, $Ew = 300$] at $t = 0.3$; (a) the wide view, and (b) the zoomed view of the dashed box in (a) for four different cases $\chi_p = 60$, $\chi_p = 80$, $\chi_p = 100$ and $\chi_p = 120$ which χ_p represents the number of nodes per nozzle diameter. The wide view in (a) is shown for the resolution of $\chi = 100$	97
5.54	Instants of the printing process for simulation condition of [$Re = 0.02$, $Ew = 400$] at (a) $t = 1.511$, (b) $t = 1.566$, and (c) $t = 1.593$	98
5.55	The surface tension force (at the left) and the electric force (at the right) for simulation condition of [$Re = 0.02$, $Ew = 400$] at $t = 1.593$	99
5.56	The variations of jet diameter for variations of Reynolds number in $Ew = 400$; (a) $Re = 0.02$, (b) $Re = 0.05$, (c) $Re = 0.10$, and (d) $Re = 0.20$	100
5.57	The variations of jet diameter for various Electro-Weber number in a $Re = 0.02$; (a) $Ew = 300$, (b) $Ew = 400$, (c) $Ew = 500$, (d) $Ew = 600$, (e) $Ew = 700$, and (f) $Ew = 800$	101
5.58	The unstable regimes of printing obtained for three cases, (a) $Re = 0.10$ and $Ew = 600$, (b) $Re = 0.10$ and $Ew = 700$, (c) $Re = 0.10$ and $Ew = 800$	101
5.59	The normalized diameter of the measure thickness of the printing jet for variations of Ew and Re numbers.	102
5.60	The dimensionless touching time for variations of Reynolds and Electro-Weber numbers.	103

List of Tables

4.1	The comparison of Taylor’s and Feng’s analytical solutions with present ISPH results for the deformation index D for different combinations of conductivity and permittivity ratios.	26
5.1	Simulation parameters for comparison of forces due to the applied electric field	32
5.2	Simulation parameters for assessing the effect of electric force on the instability. Cases B and C are retabulated for the ease of comparison.	35
5.3	The comparison of various electric permittivity values	39
5.4	The comparison of various electric field strengths	43
5.5	The dimensionless parameters and their corresponding magnitudes and/or ranges that is being used in this study	51
5.6	The dimensionless parameters and their corresponding magnitudes, which have been used to investigate the interaction of bubbles for different orientations and initial center to center distances.	58
5.7	Validation of Numerical code with the experiments of Bhaga <i>et al.</i> [111] and Hua <i>et al.</i> [65] for three test cases; VT1: $Re = 33.02$ and $Bo = 116$, VT2: $Re = 135.4$ and $Bo = 116$, and VT3: $Re = 15.24$ and $Bo = 243$	63
5.8	The magnitudes of the simulation conditions for head-on coalescence cases.	86
5.9	The magnitudes of the simulation conditions for head-on and head-off coalescence cases.	87
5.10	The magnitudes of the simulation conditions for electro-coalescence cases.	89
5.11	The normalized jet diameter for variations of Re and Ew numbers; the Reynolds number varies from $Re = 0.02$ to $Re = 0.02$ and the Electro-Weber number varies from $Ew = 300$ to $Ew = 800$	102

Nomenclature

Mathematical symbols

- \cdot Dot product operator
- Δ Delta (difference) of a variable
- $\frac{D}{Dt}$ Material time derivative
- ∇ Gradient operator
- \int Integral operator
- lim Limit operator
- \otimes Dyadic product operator
- \sum Summation operator
- \times Cross product operator
- $exp()$ Exponential operator

Subscript/Superscript symbols

- $\dot{\square}$ Rate of change
- \square^+ Dimensional variables
- \square^* Intermediate values
- $\square^{(n)}$ Properties at the n-th time step
- \square_i Associated to particle of interest i
- \square_j Associated to the neighboring particle j
- \square_b Associated properties to bubble phase

\square_d	Associated properties to droplet phase
\square_f	Associated properties to background fluid phase
\square_h	Associated properties to heavier phase
\square_{in}	Associated properties to inner phase
\square_l	Associated properties to lighter phase
\square_{out}	Associated properties to outer phase

Physical variables

α	Threshold cut-off factor for unit normal vectors
$\delta \mathbf{r}$	Artificial particle displacement vector
χ	Coefficient of kernel function
χ_p	Number of grid points
δv	Velocity difference of interacting bubbles
δ	Dirac delta function
δ_t	Dimensional thickness of printing film
η	Coefficient of artificial particle displacement vector
γ	Surface tension coefficient
$\hat{\mathbf{n}}$	Unit normal vector
\hat{c}	Unsmoothed color function
κ	Curvature
Λ	Volume Fraction
λ	Wave length
\mathcal{B}	CFL coefficient
\mathcal{K}	Coefficient of smoothing length
\mathcal{L}	Distance between droplet interfaces
\mathcal{S}	Normalized diameter of printing film

\mathcal{X}	Symbolic representation of any physical variable
d	Diameter of bubble/droplet
$d\mathbf{r}_j$	Differential volume element
D_r	Normalized diameter of toroidal droplet
h_b	Tip position of bubble
h_s	Tip position of spike
r	R coordinate of axisymmetric system
u	Approaching velocity
v	Vertical rise velocity
W	Width of computational domain
z	Z coordinate of axisymmetric system
μ	Viscosity
μ_M	Magnetic permeability
Ω	Total bounded volume
∂	Partial derivative
ϕ	Electric potential
Π	Number of particles per unit diameter of droplet
ψ	Number density
ρ	Density
σ	Electrical conductivity
τ	Viscous stress tensor
τ_w	Wall shear stress
θ	Angle between interacting bubbles
ε	Electrical permittivity
φ_F	Feng discrimination function

φ_T	Taylor discrimination function
ϱ	Horizontal diameter of the deformed bubble/diameter
ς	Vertical diameter of the deformed bubble/droplet
B	Magnetic field vector
D	Displacement vector
E	Electric field vector
$\mathbf{f}_{(b)}$	Body force
$\mathbf{f}_{(e)}$	Electrical force
$\mathbf{f}_{(s)}$	Surface tension force
g	Gravitational acceleration vector
I	Identity matrix
J	Total volume current
j	Volume conduction charge current
$\mathbf{T}_{(e)}$	Maxwell stress tensor
u	Velocity vector
x	Position vector
ξ_s	Disturbance amplitude
ζ	Symbolic representation of any physical variable
a^{xy}	Second rank corrective tensor
c	Smoothed color function
d_{in}	Inlet nozzle diameter
E_∞	Undisturbed electric field
f	Any arbitrary function
H	Height of computational domain
h	Smoothing length

h^l	Half of the thickness of the lubrication film
h_d	Initial distance of bubble/droplet center from bottom boundary
h_{in}	Inlet nozzle height
J_n	Total number of neighboring particles
k	Wave number
l^*	Center to center distance of bubbles/droplets
L_c	Capillary length scale
l_c	Characteristic length scale
m	mass
p	Pressure
q	Normalized distance between particles
q^v	Volume charge density
r	Radius of bubble/droplet
r^l	Particle position in coalescence coordinate system
r_{ij}	Position vector
r_{avg}	Average particle spacing
t	Time
t^E	Bulk relaxation time
t^μ	Viscous time scale
U^*	Dimensionless velocity scale
u^l	Lubrication velocity
u_c	Characteristic velocity
u_d	Dielectrophoretic velocity
u_g	Gravitational velocity
U_t	Terminal rise velocity

u_{max}	Largest particle velocity
v_b	Undisturbed electric field
v_c	Height of computational domain
W_{ij}	Kernel function
x'	X coordinate of the coalescence coordinate system
$x_{(s)}$	Interface x coordinate
y'	Y coordinate of the coalescence coordinate system
y_c	Position of center of bubble
$y_{(s)}$	Interface y coordinate
z_d	Projection of distance between droplet centroids

Dimensionless parameters

At	Atwood number
β	Impact parameter
Bo	Bond number
Cr	Confinement ratio
Ec	Electro-capillary number
Eg	Electro-gravitational number
Ew	Electro-Weber number
\mathcal{C}	Electrical conductivity ratio
\mathcal{D}	Density ratio
\mathcal{P}	Electrical permittivity ratio
\mathcal{V}	Viscosity ratio
D	Deformation index
Re	Reynolds number
Re*	Reynolds number (experimental)

Re_c^* Reynolds number (based on rise velocity)

We Weber number

A_r Aspect ratio

Chapter 1

Introduction

1.1 Multiphase Flows

Multiphase flows can be referred to any system consisting more than one component or phase. However, it should be declared that the components or phases are assumed to be well mixed above the molecular level, or in other words, the length scale in multiphase flows is presumed to be much greater than that in molecular scale. Considering the above definition, multiphase flows are frequently observed in numerous industrial practices and natural events; in refining processes where the separation of phases is of interest, in internal combustion engines where fuel is sprayed into and exhaust is drained out from the combustion chamber, in boiling, in ink-jet printing and drug-delivery. In nature, examples of multiphase flows include sedimentation of particles in fluids, blood flow, rain and snow.

According to their applications, multiphase flows can be classified based on the physical properties of phases into liquid-liquid, gas-liquid, solid-liquid and gas-solid categories. Multiphase flows can also be categorized based on the topology of the interface between phases into (i) disperse flow where a finite number of particles/drops/bubbles are distributed in a background continuous fluid, (ii) separated flow where two or more continuous phases are separated by an interface, and (iii) mixed flow where there is no explicit interface between different phases and phases are in a mixed system.

In order to control a multiphase flow system, numerous approaches are tested and implemented. For example, adding surfactants to a multiphase system may change

the coefficient of surface tension to maintain a desirable flow regime [1, 2]. However, adding surfactants to a multiphase flow system has several restrictions which hinders its practice to a general extent. By adding surfactants, the coefficient of surface tension can be increased or decrease to a certain level but it is generally not practical to maintain a wide range of surface tension coefficient by adding surfactants. Utilizing surfactants in multiphase flows is also restricted due to their physical and chemical properties. They should be chemically and physically compatible to all fluidic phases, and in many occasions they should be non-hazardous or non-corrosive [3]. Another important drawback of surfactants in controlling multiphase flow systems is that they cannot usually be controlled dynamically in real time. A multiphase flow system can be controlled by magnetic forces, as well [4, 5]. The magnetohydrodynamics effect is also limited to certain extents. For example, not all materials are magnetizable and the application of magnetohydrodynamics is restricted to certain magnetic materials. This is despite the fact that there are attempts to enhance the magnetization effect of fluids by adding nano-magnetic particles. The Electrohydrodynamics is a suitable alternative for controlling a multiphase flow system. The imposition of electric potential is practical and feasible for a wide range of applications of multiphase flows. Moreover, the multiphase system can be controlled dynamically by adjusting the applied electric field.

1.2 Electrohydrodynamics

Electrohydrodynamic (EHD) is referred to the interactions between electrostatic forces and other interfacial and volumetric forces in fluid dynamics. Applications of the EHD within the framework of multiphase flow problems include charge distribution in the formation of thunderstorms in meteorology, filtering materials and extracting contaminants from industrial exhaust, heat transfer enhancement, polymers and poly-electrolytes, and in electro-spinning and electro-printing.

Based on the electrical properties, fluids can be classified into three different categories, (i) the perfect conductors in which electric charges can be conducted freely in the matter (ii) perfect dielectrics (insulator) where no electric charges can be conducted and (iii) leaky dielectrics. The later case is normally used for those type of fluids with finite electrical conductivity which allows the accumulation of electrostatic charges on the interface between fluids.

The deformation of a quiescent bubble in another fluid due to the imposition of electric field is a benchmark test cases which has been in the canon of electrohydrodynamic studies. This test case is important due to the fundamental discussions on electrohydrodynamics, while being observed in many applications, as well. Moreover, due to its geometrical simplicity, analytical solutions for the deformation of the bubble can be formulated. The perfect dielectric model [6, 7] was the first model developed to predict the behaviour of a suspended bubble under electrohydrodynamics effects in a quiescent fluid. Within the framework of perfect dielectric model, the electrostatic force is generated due to the difference between the electric permittivity of fluid phases across the interface, and the induced EHD force always acts perpendicular to the interface, deforming the bubble into a prolate shape in the direction of electric field. Later, Taylor [8] proposed the leaky dielectric model which considers a finite electrical conductivity for fluids. Due to the presence of electric currents in a finite conductive medium, electric charges accumulate on the interface, providing a tangential electric stress. This tangential electric stress generates hydrodynamic stress on the interface, resulting the bubble to deform both in oblate and prolate formations. The analytical results of Taylor's leaky dielectric model was validated by comparing with experimental results of Vizika *et al.* [9] and Torza *et al.* [10].

Extensive numerical simulation validated the Taylor's leaky dielectric model in literature. Feng *et al.* [11] carried out a numerical study on the EHD deformation of a bubble under the leaky dielectric assumption and proposed a new analytical formula to predict bubble deformation in two-dimensional coordinate. The EHD bubble deformation was simulated by Hua *et al.* [12] for both perfect and leaky dielectric models in a wide range of EHD parameters such as permittivity and conductivity ratios and the electric field strength. They showed that three possible regimes can be achieved based on the selection of electric permittivity and conductivity ratios considering the leaky dielectric model. It is also found that for the leaky dielectric model, the numerical results deviates from analytical solution of Taylor in large deformations. The reason lies behind the fact that the analytical solutions are derived based on the assumption in which the bubble remains almost spherical that is not valid for large bubble deformations. Shadloo *et al.* [13] modeled the bubble deformation for the leaky dielectric model and compared the numerical results with Taylor and Feng theories. They showed that Taylor's theory gives better results when the bubble oblates while the Feng's theory is closer to numerical results in large prolate deformations.

These analytical, experimental and numerical studies on the effect of bubble deformation provided sufficient background to investigate the electrohydrodynamic effects on other practices in multiphase flow problems. The breakup of Newtonian and non-Newtonian droplets [14–16], fluid-fluid emulsions [17, 18], stability of liquid bridges [19, 20] and bubble rising [21, 22] are just some examples. The electrohydrodynamics is also successfully investigated on some industrial applications such as electro-spinning [23–25] and electro-jet printing [26–28]. However, the electrohydrodynamics is not extensively studied in the field of multiphase flows and many questions are still remained unanswered.

1.3 Numerical Simulation of Multiphase Flows

Numerical study of physical problems is a growing approach in various disciplines of science. In the scope of fluid dynamics, the Computational Fluid Dynamics (CFD) is developed and extended in the past couple of decades with the advances in computational power. The CFD has been utilized to simulate many problems in industry and academy ranging from aerodynamic [29, 30], combustion [31, 32], turbo-machinery [33, 34] and rheology [35, 36].

In CFD, numerical methods can be generally classified into two main independent and complementary approaches, the Eulerian approach and the Lagrangian approach. In the Eulerian approach, the frame of the computational domain is fixed on a certain spacial coordinate where the flow is studied. In contrast, the Lagrangian approach solves the constitutive equations of motion by following individual fluid material particles. Each of these approaches have their own advantages and disadvantages, and are suitable for certain number of applications. Based on each of these numerical approaches, Finite Volume, Finite Element and Finite Difference methods are developed which solve governing equations of fluid dynamics over discretized domain volumes, elements, and grids, respectively. Alternatively, the governing equations of fluid dynamics can be solved over discrete material points which can freely move in the computational domain. The methods based the later approach are often referred to meshless or meshfree methods.

The Computational Fluid Dynamics is extensively implemented on multiphase flow problems. For dispersed phase and continuous phase problems, different front-tracking [37, 38] and front-capturing [39, 40] methods are developed to identify the interface between fluid phases. One of the main challenges in the simulation of multiphase flows is the implementation of the interfacial forces such as surface

tension. Several methods have been applied to calculate surface tension force such as Continuum Surface Stress (CSS), and Continuum Surface Force (CSF) models. The later which is developed by Brackbill *et al.* [41] was extensively implemented on multiphase flow problems such as bubble dynamics [12, 42], fluid instabilities [43, 44], and free surface flows [45, 46], amongst others.

1.4 State-Of-The-Art

In this part, the important features of this Ph.D. dissertation and its significance to scientific community and industrial applications are presented. Moreover, the numerical test-cases are introduced and their importance in the field of multiphase flow problems and electrohydrodynamics is briefly discussed. The numerical method is also introduced and its advantages and drawbacks are concisely discussed.

In this study, several dispersed flow and continuous flow multiphase problems are investigated using the Smoothed Particle Hydrodynamics method and a commercial CFD tool, under the effects of electrohydrodynamics. These problems are the Rayleigh-Taylor instability, bubble rising, droplet coalescence and electro-jet printing. These problems are interesting from different perspectives, such as their practical applications and their length-scales. Regarding the electrohydrodynamic aspects of this study, it is important to realize how multiphase flow systems behave under the impact of electric forces and how to control multiphase flow systems using electrohydrodynamics.

The Rayleigh-Taylor Instability is a physical instability between two sheets of fluids where the gravitational force is applied normal to the interface between fluid phases from heavier to lighter phase. Thus, in the presence of a small perturbation on the interface, spikes of heavier and bubbles of lighter phase penetrate into the lighter and heavier fluids, respectively. A phenomenological study is performed on the Rayleigh Taylor Instability, and the action of electrohydrodynamics on multiphase flow systems and the impact of different electrostatic parameters are investigated. The study of Rayleigh Taylor Instability gives general idea on the effects of electrohydrodynamics and is essential for understanding the influence of electrohydrodynamics on other problems.

The bubble rising occurs when a lighter dispersed phase travels in a heavier fluid due to the gravitational force. The bubble rising which can be a meso-scale or

a micro-scale phenomenon, is well-studied in literature, but the effect of electric forces on this problem is not comprehensively investigated. It is important to investigate the controlling behaviour of electrohydrodynamics on bubble rising which can be implemented in many industrial applications. The droplet coalescence is a similar problem to bubble rising in terms of both industrial and phenomenological importance, but had less attention due to its natural complexity.

The electro-jet printing is an industrial application of electrohydrodynamics on multiphase flows where an injected fluid is printed to maintain a desirable deposition film thickness (usually thinner than the injector diameter). The electro-jet printing is a micro-scale problem where the influence of surface forces are more pronounced. Numerical studies on the electro-jet printing is not extensively carried out, although it has great potentials in many industrial applications.

1.4.1 The Smoothed Particle Hydrodynamics (SPH) method

In order to simulate the problems described above, the meshless Smoothed Particle Hydrodynamics (SPH) method is selected. In the SPH method, the domain is discretized into material particles and the governing equations of fluid dynamics are solved for individual particles. The interactions between particles are made via a kernel function with a finite domain of influence, smoothing the physical properties over that domain. Based on the relative proximity of particles, the influence of a neighboring particle on a particle of interest is determined.

The SPH method delivers certain advantages compared to conventional mesh-dependant schemes. It does not require initial meshing and consequently, the pre-processing of the SPH method is relatively simple for complex geometries. The SPH method is a relatively simple-to-implement method compared to other mesh-dependant methods such as Finite Element and Finite Volume methods. Since many problems undergo large deformations during simulations, the SPH method does not require remeshing or dynamic mesh adaptation which results in massive computational cost for large-scale problems. Another important feature of the SPH method is in the modelling of multiphase flows. The SPH method treats large density ratios with no additional cost, and the interface between fluid phases is a natural outcome of the SPH method, thus no interface reconstruction is required.

The Smoothed Particle Hydrodynamics (SPH) method was initially developed by Gingold and Monaghan [47] for astronomical purposes, but the method has been

successfully applied to a wide range of fluid dynamics problems. In the framework of fluid dynamic, the method was initially developed for simulating single phase flow problems [48]. Soon after, Monaghan [49] showed that the method is capable of simulating multiphase flow problems as well. Morris [50] extended the method for simulation of surface tension force in the SPH method. He implemented the continuum Surface Force (CSF) model introduced by Brackbill *et al.* [41] for this purpose. Thereafter, the SPH method was successfully tested for multiphase flow problems such as bubble rising, bubble under shear flow, and Rayleigh Taylor Instability [44, 51, 52], amongst others. Details of the developments in the SPH method can be found in [53, 54] for more interested readers.

Initially, the SPH method was introduced as a compressible method. In order to impose incompressibility for incompressible fluid dynamics, an equation of motion was solved to obtain the pressure as a function of density variations and an artificial speed of sound, named as the Weakly Compressible SPH (WCSPH) method. However and in spite of improvements to increase its accuracy and performance, the method suffers from artificial pressure fluctuation. Moreover, in order to keep density variations in an acceptable range, time-steps should be taken sufficiently small and consequently, the Courant-Friedrichs-Lewy (CFL) condition was not only dependant on the fluid velocity, but also the speed of sound. Cummins *et al.* [55] introduced the SPH projection method which is based on solving a pressure Poisson equation to obtain the pressure field and impose the incompressibility, which is later introduced as the Incompressible SPH (ISPH) method. Despite being computationally more expensive to solve the Poisson equation compared to the equation of state for pressure, the ISPH method allows much larger time steps and provides non-fluctuating pressure field compared to the WCSPH method. Yet, both the WCSPH and the ISPH methods are attractive to researchers and their performance, accuracy, robustness and implementation are widely discussed, and their results are compared to a broad extent. In this work, a numerical algorithm based on the incompressible SPH method is used.

Recent studies on the simulation of multiphase flows using the SPH method are performed in various directions, including improvements on the method as well as applying existing schemes into different multiphase flow problems. Breinlinger *et al.* [56] proposed a model for gas-liquid surface tension and the contact angle and triple point on the wetted surfaces in the SPH method. Recently, Tartakovsky *et al.* [57] introduced a Pairwise Force SPH method for modelling surface tension and contact line by applying the Young-Laplace boundary condition for fluid-fluid interface. Other investigations on modelling multiphase problems using the SPH

method are the simulation of porous media [58, 59], and heat transfer [60, 61], amongst others. A review of recent applications of the SPH method on different problems can be found in [62]. However, the multiphase flow problems are not investigated under the effects of electrohydrodynamics with the SPH method to date.

Although the SPH method has numerous advantages compared to other numerical schemes, it has its own limitations and restrictions. The SPH method, for example is not capable of handling axi-symmetric problems due to its particle based nature. Another drawback of the SPH method is the difficulty in simulation inlet-outlet boundaries. Thus, in order to simulate multiphase flows with the aforementioned characteristics, a commercial CFD tool is used.

1.4.2 ANSYS Fluent

The ANSYS-Fluent is a commercial CFD tool developed to simulate fluid flow problems using the Finite Volume method, and the simulation of multiphase flows for continuous and dispersed phases are treated using the Volume Of Fluid (VOF) model. The ANSYS Fluent provides various solution schemes and method for spatial and temporal discretizations and pressure-velocity couplings. The software is equipped with useful modules to facilitate the simulation of a broad range of problems. However, the electrohydrodynamic module has not developed, yet. In order to simulate electrohydrodynamics forces, User Define Functions (UDFs) are developed to calculate the electric and displacement fields, surface charges and electric forces over the solution domain and the resultant electric forces are added to the momentum equation as a source term.

1.4.3 The SPH method versus the ANSYS Fluent

In this study, the focus is on the development and implementation of the SPH method for controlling a wide range of multiphase flow problems using the electrohydrodynamics. Thus, the SPH method is developed and tuned for the simulation of Rayleigh-Taylor Instability, bubble rising of an oil/water system, coalescence of binary approaching droplets and electro-coalescence of binary stationary droplets. On the other hand, it is observed that there are interesting unfolded physics behind the bubble rising of an air/water system and the electro-jet printing. The

simulation of these problems by the SPH method encountered numerous problems, thus a commercial CFD software is utilized for those simulations.

One of the main limitations in the simulation of the aforementioned problems using the SPH method is the computational cost of these problems. For the simulation of bubble rising with the two-dimensional 180×300 particles resolution (the selected resolution), it takes approximately around 800 minutes of computational time for 0.1 seconds of simulation time on an Intel Xeon E5-2690 2.60 GHz CPU. The computational cost of three-dimensional simulations would be around three order of magnitude larger which hinders the simulation of three-dimensional test-cases. Thus, all simulations are performed in two-dimensional framework to reduce computational cost. On the other hand, for the simulation of bubble rising with large density ratios, it is reported in literature [63–65] that the bubble may deform into a toroidal shape in large Reynolds and Bond numbers magnitudes. However, this is not observed in two-dimensional simulations such as [66, 67] where separations alternatively occurs from the side tails of the rising bubble. In order to observe this phenomena, an axi-symmetric system can be developed which keeps the computational cost much smaller than full three-dimensional frameworks. Since the implementation of axi-symmetric systems is not feasible within the framework of the SPH method, the development of commercial CFD packages becomes the resolution to simulate the bubble rising with a high density ratio. This CFD package is also employed to the electro-jet printing due to the limitations of SPH method in inlet-outlet boundaries problems which has been discussed earlier.

Chapter 2

Governing Equations

2.1 Mechanical balance laws of continua

All constituents of the multiphase system are considered to be viscous, Newtonian and incompressible liquids with constant material properties. According to these assumptions, the Navier-Stokes equation for the conservation of mass and momentum can be written in the form of

$$\nabla \cdot \mathbf{u} = 0, \quad (2.1)$$

$$\rho \frac{D\mathbf{u}}{Dt} = -\nabla p + \nabla \cdot \boldsymbol{\tau} + \mathbf{f}_{(s)} + \mathbf{f}_{(e)} + \mathbf{f}_{(b)}, \quad (2.2)$$

where \mathbf{u} is the velocity vector, and ρ and p are density and pressure. t is time and $\frac{D}{Dt}$ is the material time derivative represented as, $D/Dt = \partial/\partial t + \mathbf{u} \cdot (\partial/\partial \mathbf{x})$, while $\boldsymbol{\tau}$ is the viscous stress tensor which can be expressed as

$$\boldsymbol{\tau} = \mu [\nabla \mathbf{u} + (\nabla \mathbf{u})^T], \quad (2.3)$$

where μ denotes viscosity. In the above equation, the superscript T represents the transpose operation. It should be noted that the surface tension force $\mathbf{f}_{(s)}$ is a local surface force and the calculation of which requires the solution of the jump condition for the momentum balance. For the sake of computational convenience and efficiency, it is a common practice to express the local surface force $\mathbf{f}_{(s)}$ as an equivalent volumetric force (force per unit volume). This has been introduced

by Brackbill *et al.* [41] proposing the Continuum Surface Force (CSF) method. The basic concept behind this approach is to replace the sharp interface between two fluids with a transition region of a finite thickness which is also referred to as a diffusive interface. This can be fulfilled through multiplying the local surface tension force with a Dirac delta function δ , and the effect of surface tension can be consequently included in the momentum balance equation in the form of an external force term as [68, 69]

$$\mathbf{f}_{(s)} = \gamma \kappa \hat{\mathbf{n}} \delta. \quad (2.4)$$

In this equation, γ is the surface tension coefficient taken to be constant in this study, κ is the surface curvature equal to $-\nabla \cdot \hat{\mathbf{n}}$ where $\hat{\mathbf{n}}$ is the unit normal vector. In equation 2.2, $\mathbf{f}_{(b)}$ is the body force for imposing the gravitational force equal to $\mathbf{f}_{(b)} = \rho \mathbf{g}$ where \mathbf{g} is the gravitational acceleration vector, and $\mathbf{f}_{(e)}$ is the electric force which is added to the momentum equation as a source term. It is important to mention that all material and field properties in this chapter are dimensional. In order to differentiate between dimensional and dimensionless properties in next chapters, a plus sign is explicitly introduced and used for dimensional properties.

2.2 Electrohydrodynamics Balance Laws

Electrohydrodynamics (EHD) is a science concerned with the interactions of electric fields and electric charges in fluids. The electrical conductivity of fluids may range from exceedingly low value to high value hence allowing for a fluid to be classified as extremely good insulator (dielectrics) or highly conducting. In electrohydrodynamics transport phenomena, due to the transient nature of the problems, the electric current distribution is not steady. Therefore, in accordance with the Ampere-Maxwell's law,

$$\nabla \times \mathbf{B} = \mu_M \mathbf{J} + \mu_M \varepsilon \frac{\partial \mathbf{E}}{\partial t}, \quad (2.5)$$

dynamic currents in the system give rise to a time-varying induced magnetic field. Here, \mathbf{B} and \mathbf{E} respectively are magnetic and electric field vectors, μ_M is the magnetic permeability, and \mathbf{J} is total volume current. In electrohydrodynamics,

the dynamic currents are so small that the influence of magnetic induction is negligible whereby the electromagnetic part of the system can be described by a *quasi-static electric field model*. Additionally, in the system considered, there is no externally applied time-varying magnetic field. In light of these assumptions, the coupling between the electric and magnetic field quantities in the Faraday's law $\nabla \times \mathbf{E} = -\partial \mathbf{B} / \partial t$ disappears which requires that the electric field vector be irrotational as [70]

$$\nabla \times \mathbf{E} = \mathbf{0}, \quad (2.6)$$

which necessitates that the gradient of the electric field vector be a symmetric tensor, namely, $\nabla \mathbf{E} = (\nabla \mathbf{E})^T$. The total volume current is defined as

$$\mathbf{J} = q^v \mathbf{u} + \mathbf{j}, \quad (2.7)$$

where the first term on the right hand side is the convection current due to the free charges, q^v is the volume-charge density of free charges, and \mathbf{j} is the volume conduction current density, ohmic current, which is related to electric field vector through

$$\mathbf{j} = \sigma \mathbf{E}, \quad (2.8)$$

where σ is the electrical conductivity.

The Gauss' law for electricity in a dielectric material with the absolute permittivity (hereafter referred to as the permittivity) ε can be written in terms of the electric displacement vector, $\mathbf{D} = \varepsilon \mathbf{E}$ as

$$\nabla \cdot \mathbf{D} = q^v. \quad (2.9)$$

On taking the divergence of the differential form of Ampere's law, and using the entity $\nabla \cdot \nabla \times \mathbf{B} = 0$ (the divergence of the curl is equal to zero) together with the Gauss' law (Eq. (2.9)) for electricity, one can write the charge conservation as

$$\frac{Dq^v}{Dt} + \nabla \cdot \mathbf{j} = 0. \quad (2.10)$$

Considering a homogeneous fluid with the constant permittivity and the electrical conductivity, and then substituting the Gauss' law for electricity in a dielectric material (Eq. (2.9)) together with the volume conduction current density (Eq. (2.8)) into the charge conservation equation (Eq. (2.10)), one can write

$$\dot{q}^v = -q^v \frac{\sigma}{\varepsilon}. \quad (2.11)$$

The integration of this differential equation produces

$$q^v = q_o^v \exp\left(\frac{-t}{t^E}\right), \quad (2.12)$$

which describes the time relaxation of the net free charges along fluid particles line. Hence, homogeneous fluids support no net free charges. However, in inhomogeneous materials, free charges can be generated by an electric field component along the gradients of conductivity and/or permittivity. Here, $t^E = \varepsilon/\sigma$ is referred to as the bulk relaxation time. For electrohydrodynamics problems, the time t can be considered as the viscous time scale of the fluid motion, which is defined as $t^\mu = \rho l_c^2/\mu$, where l_c is the characteristic length scale. A two-fluid system can be classified as dielectric-dielectric, dielectric-conducting, or conducting-conducting by comparing the magnitude of t^E with t^μ where the last case is the focus of this work.

As stated previously, the electrostatics and hydrodynamics of a fluid system can be coupled together in the momentum balance equation through the Maxwell stress tensor which accounts for the stress induced in an incompressible liquid medium due to the presence of an electric field. The Maxwell stress tensor can be written as [70, 71]

$$\mathbf{T}_{(e)} = \mathbf{D} \otimes \mathbf{E} - 0.5(\mathbf{D} \cdot \mathbf{E})\mathbf{I}, \quad (2.13)$$

where in Eq. (2.13), \otimes and \mathbf{I} represent the dyadic product and identity matrix, respectively, while the contribution from the induced magnetic field was neglected. Upon taking the divergence of the Maxwell stress tensor and then using Eq. (2.9) and the symmetry of the gradient of the electric field vector as well as the product rule of differentiation, one can obtain the electric force $\mathbf{f}_{(e)}$ per unit volume as [70, 71]

$$\mathbf{f}_{(e)} = q^v \mathbf{E} - 0.5 \mathbf{E} \cdot \mathbf{E} \nabla \varepsilon, \quad (2.14)$$

Here, the first term on the right hand side of Eq. (2.14) is the electric force acting along the direction of the electric field due to the interaction of the free charges with the electric field while the second term accounts for the polarization force due to the pairs of charges, which acts along the normal direction to the interface as a result of term $\nabla \varepsilon$.

2.3 Leaky dielectric model

For a two-fluid system with finite electrical conductivities in a quasistatic electric field and $t^\mu \gg t^E$ and in the absence of buoyancy forces, volume charge conservation can attain steady state condition (i.e., $Dq^v/Dt = 0$) in a time scale much smaller than the viscous time scale of the fluid motion. Such a system can be referred to as conducting-conducting. Therefore, relying on the quasistatic assumption, the conservation of charge in Eq. (2.10) can be simplified to

$$\nabla \cdot (\sigma \mathbf{E}) = 0. \quad (2.15)$$

Additionally, since the electric field is irrotational ($\nabla \times \mathbf{E} = 0$), due to the mathematical entity of $\nabla \times \nabla \phi = 0$ (the curl of the gradient is equal to zero), which holds for any arbitrary scalar field, the electric field vector can be expressed in terms of electric potential as

$$\mathbf{E} = -\nabla \phi, \quad (2.16)$$

where ϕ is the electric potential. This would mean that the charge conservation equation (Eq. (2.15)) in the domain can be re-written as

$$\nabla \cdot (\sigma \nabla \phi) = 0. \quad (2.17)$$

With the solution of Eq. (2.17), the electric potential can be obtained, and then the electric field strength is calculated by $\mathbf{E} = -\nabla \phi$. Based on Eq. (2.9), we can obtain the distribution of volume charge density as $q^v = \nabla \cdot (\varepsilon \mathbf{E})$. Having

calculated the distributions of electric charge density and electric field strength, the electric force within the liquid bulk in the vicinity of interface can then be determined through Eq. (2.14) for incompressible fluid.

Upon combining Eq. (2.2) with Eqs. (2.4) and (2.14), one can obtain the equation of motion including volumetric surface tension and electric field forces as

$$\rho \frac{D\mathbf{u}}{Dt} = -\nabla p + \mu \nabla^2 \mathbf{u} + \gamma \kappa \mathbf{n} \delta + q^v \mathbf{E} - 0.5 \mathbf{E} \cdot \mathbf{E} \nabla \varepsilon + \rho \mathbf{g}. \quad (2.18)$$

Chapter 3

Numerical Methodology

3.1 The SPH Principles

Smoothed Particle Hydrodynamics (SPH) method is a meshless particle based approach which was originally introduced separately by and Gingold *et al.* [47], and Lucy [72] to simulate astrophysical problems. Later on, it was adapted to be able to carry out simulations in other fields of engineering and natural sciences, especially fluid dynamics and solid mechanics. Recent developments empowered this method to model more complicated physical phenomena such as multiphase flows, and fluid-solid interactions. Benefiting from its particle based nature, distributed particles in the continuum are influenced by their neighboring particles by means of a weighting or kernel function $W(r_{ij}, h)$, or in a concise notation, W_{ij} . Any arbitrary kernel function W_{ij} , which satisfies certain conditions [73, 74], can relate the particle of interest i to its neighboring particles j through the magnitude of the distance vectors for pairs of particles $r_{ij} = |\mathbf{r}_{ij}|$ and the smoothing length h , where $\mathbf{r}_{ij} = \mathbf{r}_i - \mathbf{r}_j$. A particle j is called a neighbor particle to i as long as $r_{ij} < \mathcal{K}h$ where \mathcal{K} is a constant associated with the particular weighting function and $\mathcal{K}h$ is referred to as a smoothing radius (cut-off distance, support or localized domain) beyond which the weighting function goes to zero. For the clarity of the presentation, it is worthy of introducing notational conventions to be used in the rest of this article. Latin italic indices ($i ; j$) are used only as particle identifiers to denote particles and will always be placed as subscripts that are not summed unless used under the summation symbol. When a vector is written in a component form, suffix notation is employed with Latin italic indices placed as superscripts.

As well, throughout this article the Einstein summation convention is employed whereby any repeated component index is summed over the range of the index.

The integral approximation of any arbitrary function for particle i , f_i , can be written as

$$f_i \cong \langle f_i \rangle \equiv \int_{\Omega} f_j W_{ij} d\mathbf{r}_j, \quad (3.1)$$

where $d\mathbf{r}_j$ is a differential volume element and Ω represents the total bounded volume of the domain. Upon replacing the integral operation over the volume of the bounded domain by the mathematical summation operation over all neighboring particles j of the particle of interest i , and the differential volume element by the inverse of the number density ψ_j for a particle j , one thus obtains a discrete representation of Eq. (3.1) as

$$f_i = \sum_{j=1}^{J_n} \frac{1}{\psi_j} f_j W_{ij}. \quad (3.2)$$

The number density for the particle i can be calculated as

$$\psi_i = \sum_{j=1}^{J_n} W_{ij}. \quad (3.3)$$

It may also be expressed in terms of the particle density ρ and the mass m by

$$\psi_i = \rho_i / m_i. \quad (3.4)$$

Upon substituting f_j by $\partial f_j / \partial x_j^k$ in Eq. (3.1) and then performing the integration by parts, then converting the following volume integral $\int_{\Omega} \partial(f_j W_{ij}) / \partial x_j^k d\mathbf{r}_j$ to the surface integral through using the divergence theorem and noting that this surface integral should be zero due to the fact that the kernel function goes to zero beyond its support domain, and finally knowing that $\partial W_{ij} / \partial x_j^k = -\partial W_{ij} / \partial x_i^k$, one may obtain the simplest form of the SPH discretization for the gradient of the arbitrary function f_i as

$$\frac{\partial f_i}{\partial x_i^k} = \sum_{j=1}^{J_n} \frac{1}{\psi_j} f_j \frac{\partial W_{ij}}{\partial x_i^k}. \quad (3.5)$$

The above SPH approximation for the spatial discretization of a gradient operation has been known to be incapable of providing sufficient accuracy, wherefore more accurate discretization schemes have been proposed in literature. One of them is known as a corrective SPH gradient discretization [68] which can be obtained upon using a Taylor series expansion and the properties of a second-rank isotropic tensor, and written for an arbitrary vector valued function as

$$\frac{\partial f_i^p}{\partial x_i^k} a_i^{ks} = \sum_{j=1}^{J_n} \frac{1}{\psi_j} (f_j^p - f_i^p) \frac{\partial W_{ij}}{\partial x_i^s}, \quad (3.6)$$

where $a_i^{ks} = \sum_{j=1}^{J_n} \frac{1}{\psi_j} r_{ji}^k \frac{\partial W_{ij}}{\partial x_i^s}$ is a second rank tensor. The SPH Laplacian formulation can be written in two different ways as,

$$\frac{\partial}{\partial x_i^k} (\zeta_i \frac{\partial f_i^p}{\partial x_i^k}) = 8(a_i^{pm})^{-1} \sum_{j=1}^{J_n} \frac{2}{\psi_j} \frac{\zeta_i \zeta_j}{\zeta_i + \zeta_j} f_{ij}^p \frac{r_{ij}^p}{r_{ij}^2} \frac{\partial W_{ij}}{\partial x_i^m}, \quad (3.7)$$

$$\frac{\partial}{\partial x_i^k} (\zeta_i \frac{\partial f_i^p}{\partial x_i^k}) = \frac{8}{(2 + a_i^l)} \sum_{j=1}^{J_n} \frac{2}{\psi_j} \frac{\zeta_i \zeta_j}{\zeta_i + \zeta_j} f_{ij}^p \frac{r_{ij}^s}{r_{ij}^2} \frac{\partial W_{ij}}{\partial x_i^s}. \quad (3.8)$$

In above equations, ζ might denote μ , ρ^{-1} , ε or σ , and $f_{ij}^p = f_i^p - f_j^p$. In this work, Eq. (3.7) is used for the Laplacian of velocity while Eq. (3.8) is used for the Laplacian of pressure in the Poisson pressure equation. In a multiphase system, the accurate treatment of the jump in transport parameters across the interface is important for the accuracy and robustness of the SPH scheme wherefore a weighted harmonic mean interpolation is applied in above equations as

$$\zeta_i = 2\zeta_i \zeta_j / (\zeta_i + \zeta_j). \quad (3.9)$$

It has been previously noted that the smoothing kernel has to satisfy several conditions. The first one is the *normalization condition* that requires

$$\int_{\Omega} W(r_{ij}, h) d\mathbf{r}_j = 1. \quad (3.10)$$

The second one is the *Dirac-delta function* property. That is, as the smoothing length approaches to zero, the Dirac-delta function is recovered. Hence,

$$\lim_{h \rightarrow 0} W(r_{ij}, h) = \delta(r_{ij}). \quad (3.11)$$

The third one is the compactness or *compact support* property, which necessitates that the kernel function be zero beyond its compact support domain.

$$W(r_{ij}, h) = 0 \quad \text{when } r_{ij} > \mathcal{K}h, \quad (3.12)$$

and be positive within the support domain.

The fourth one is that the kernel function has to be spherically symmetric even function

$$W(r_{ij}, h) = W(-r_{ij}, h). \quad (3.13)$$

Finally, the value of the smoothing function should decay with increasing distance away from the center particle.

In literature, it is possible to find a variety of kernel function which satisfies above-listed conditions. Most commonly used ones are spline kernel (for instance, cubic or quintic) and Gaussian functions. The smoothing kernels might be considered as discretization schemes in mesh dependent techniques such as finite difference and volume. The stability, accuracy and the speed of the SPH simulation heavily depend on the choice of the smoothing kernel function as well as the smoothing length. Considering the stability and the accuracy of the simulations, throughout the present work, the compactly supported two-dimensional quintic spline kernel is used at the expense of higher computational cost. For example, the utilization of the higher order quintic spline in simulations is at least two times computationally more expensive than that of the cubic spline. The two-dimensional quintic spline kernel function has the form of

$$W_{ij} = \chi \begin{cases} (3 - q)^5 - 6(2 - q)^5 + 15(1 - q)^5 & 0 \leq q \leq 1 \\ (3 - q)^5 - 6(2 - q)^5 & 1 \leq q \leq 2 \\ (3 - q)^5 & 2 \leq q \leq 3 \\ 0 & 3 \leq q \end{cases} \quad (3.14)$$

where $q = r_{ij}/h$ and χ is $\frac{7}{478}\pi h^2$ for 2-D simulations.

In order to implement multiphase flow problem, a color function \hat{c} is defined to distinguish between different phases, such that it assumes a value of zero for one phase and unity for the other. The color function is then smoothed out across the phase boundaries as

$$c_i = \sum_{j=1}^{J_n} \frac{\hat{c}_j W_{ij}}{\psi_i}, \quad (3.15)$$

to ensure smooth transition between the properties of each phase when used for their interpolation. Interpolation of phase properties is carried out using Weighted Arithmetic Mean (WAM),

$$\mathcal{X}_i = c_i \mathcal{X}_1 + (1 - c_i) \mathcal{X}_2, \quad (3.16)$$

where \mathcal{X} may denote density or viscosity of the fluids and numeric subscripts represent different phase properties. The smoothed color function is also utilized to evaluate $\delta \simeq |\nabla c|$, $\kappa = -\nabla \cdot \hat{\mathbf{n}}$ and $\hat{\mathbf{n}} = \nabla c / |\nabla c|$ in equation (2.4). In this formulation, a constraint has to be enforced to avoid possible erroneous normals [50]. In this study, only gradient values exceeding a certain threshold, $|\nabla c| \simeq \alpha/h$, are used in surface tension force calculations. A α value of 0.08 has been found to provide accurate results without removing too much detail [75].

3.2 Numerical Algorithm of the In-house Code

A predictor-corrector scheme is employed to advance the governing equations of flow in time using a first-order Euler approach with variable timestep according to Courant-Friedrichs-Lewy condition, $\Delta t = \mathcal{B}h/u_{\max}$, where u_{\max} is the largest particle velocity magnitude and \mathcal{B} is taken to be equal to 0.25 [75]. In predictor step, particles are displaced to their intermediate positions using

$$\mathbf{r}_i^* = \mathbf{r}_i^{(n)} + \mathbf{u}_i^{(n)} \Delta t + \delta \mathbf{r}_i^{(n)}, \quad (3.17)$$

followed by an update in transport properties due to movement of the interface. Here, the \square^* represents an intermediate value and superscript (n) denotes values at the n -th time step. Artificial particle displacement vector in (3.17) is implemented through $\delta \mathbf{r}_i^{(n)}$ as

$$\delta \mathbf{r}_i^{(n)} = \eta \left[u_{\max} \sum_{j=1}^{J_n} \left(\frac{\mathbf{r}_{ij}}{r_{ij}^3} r_{\text{avg},i}^2 \right) \right]^{(n)} \Delta t, \quad (3.18)$$

which ensures orderly particle distribution. Average particle spacing is found via $r_{\text{avg},i} = \sum_{j=1}^{J_n} r_{ij} / J_n$ while a value of $\eta = 0.06$ is employed throughout this study to ensure satisfactory particle distribution and stabilizing effect [76].

Intermediate velocities are found by calculating the right-hand side of Eq. 2.2 excluding pressure gradients at the intermediate particle locations as

$$\mathbf{u}_i^* = \mathbf{u}_i^{(n)} + \frac{1}{\rho_i^{(n)}} (\nabla \cdot \boldsymbol{\tau}_i + \mathbf{f}_{(s)i} + \mathbf{f}_{(e)i} + \mathbf{f}_{(b)i})^{(n)} \Delta t, \quad (3.19)$$

while intermediate densities are calculated employing the following relations

$$\psi_i^* = \sum_{j=1}^{J_n} W_{ij}^*, \quad (3.20)$$

$$\rho^* = m_i \psi_i^*. \quad (3.21)$$

In the corrector step, pressure at the next time step is found by solving Poisson equation subject to zero gradient boundary condition using intermediate values

$$\nabla \cdot \left(\frac{1}{\rho_i^*} \nabla p_i^{(n+1)} \right) = \frac{\nabla \cdot \mathbf{u}_i^*}{\Delta t}. \quad (3.22)$$

The velocity of the particles are corrected using the pressure at the new time step as

$$\mathbf{u}_i^{(n+1)} = \mathbf{u}_i^* - \frac{1}{\rho_i^*} \nabla p_i^{(n+1)} \Delta t, \quad (3.23)$$

and then the particles are moved to their final positions using their corrected velocities

$$\mathbf{r}_i^{(n+1)} = \mathbf{r}_i^{(n)} + \frac{1}{2} \left(\mathbf{u}_i^{(n)} + \mathbf{u}_i^{(n+1)} \right) \Delta t + \boldsymbol{\delta} \mathbf{r}_i^{(n)}. \quad (3.24)$$

3.3 Numerical Algorithm of the ANSYS-Fluent

The ANSYS-Fluent (Fluent) software is a commercial package for solving the fluid flow problems. The Finite Volume Method (FVM) is used to discretize the governing equations with the associated boundary conditions. The software provides variety of solution options to solve fluid flow problems. In order to solve the dispersed phase multiphase flow problems, the Volume of Fluid (VOF) method is used. In this method, the volume fraction Λ is calculated by solving an evolution equation as,

$$\frac{\partial \Lambda}{\partial t} + \mathbf{u} \cdot \nabla \Lambda = 0, \quad (3.25)$$

and fluid properties are smoothed on the interface by,

$$\mathcal{X} = \Lambda \mathcal{X}_1 + (1 - \Lambda) \mathcal{X}_2, \quad (3.26)$$

where \mathcal{X} can be any physical fluid property such as density, viscosity, electrical conductivity or permittivity whichever is appropriate.

The momentum equation (eq. 2.2) is solved by a second-order upwind formulation both in time and space. The Pressure Implicit with Splitting of Operator (PISO) method [77] is employed to calculate the pressure field, and the pressure and velocity fields are coupled using the improved SIMPLE scheme [78]. In addition to the continuity and momentum equations, a Laplace equation needs to be solved to obtain the electric field (eq. 2.15) in the domain. This has been carried out using a User Defined Function (UDF). Then, the electric field is evaluated as the gradient of the electric potential in the entire domain and relevant forces are calculated. Then the forces are added as a source term to the momentum equation.

Chapter 4

Numerical Validation

4.1 Numerical Validation

The present in-house ISPH code has been used to simulate a wide variety of multi-phase flow problems including fluid-solid interaction, Rayleigh-Taylor Instability, and bubble rising in the studies of the former members of our group [68, 69, 79, 80]. Nonetheless, results of numerical validation of the in-house SPH code as well as the Fluent software are presented. The validations are made with credential available numerical, experimental and analytical results in literature. These validations are performed to present the accuracy and robustness of the in-house ISPH code for calculating surface tension and electric forces as well as those of Fluent software for simulating electrohydrodynamics. Further validations are performed in the next chapter for each problem to show the validity of numerical results for various physical test-cases.

4.1.1 Validation of the in-house SPH code

In order to validate the in-house SPH code for both surface tension and electrohydrodynamic forces, a square computational domain with the dimension of $H = 4d$ is considered where d is the diameter of the droplet, and the droplet is located at its center. No-slip boundary condition along with a potential difference of $\Delta\phi = E_\infty/H$ is applied to top and bottom walls while the periodicity condition is implemented on the side boundaries. Here, E_∞ is the undisturbed electric field where in the absence of the droplet in the computational domain, the periodic

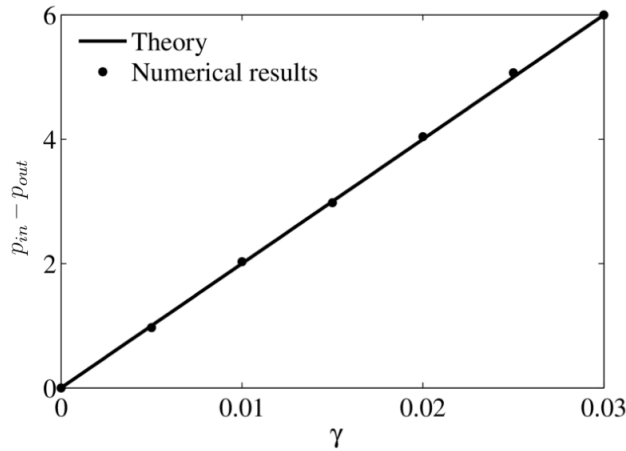


FIGURE 4.1: The comparison of numerically computed pressure jumps as a function of surface tension coefficient with that calculated by the analytical equation, namely, Laplace’s law.

boundary condition for the electric potential produces a uniform downward electric field parallel to the side boundaries. The validations are done in constant values of density and viscosity for both fluids, thus the density and viscosity ratios of fluid phases are set to $\mathcal{D} = 1$ and $\mathcal{V} = 1$, respectively. The numerical validation for the surface tension force is done in the absence of electric force, so E_∞ is set equal to zero. However, for the validation of electrohydrodynamic force, E_∞ as well as the electric permittivity \mathcal{P} and conductivity \mathcal{C} ratios are set properly to maintain desired simulation conditions.

4.1.1.1 Validation of surface tension force

The deformation of a static circular droplet under the surface tension force is a commonly utilized test case for validating the accuracy of numerically computed pressure jump across the interface in multiphase systems, which can also be calculated analytically from $p_{in} - p_{out} = 2\gamma/d$. This relation is known as the Laplace’s law that relates pressure difference between inside and outside of the droplet to the surface tension coefficient and the curvature. The simulations are performed for several values of the surface tension coefficient γ . Pressure jumps computed across the interface for various surface tension coefficients are presented in Fig. 4.1 together with the results of the analytical solution, where the linear continuous line represents the results obtained from the analytical relation while the outcomes of the numerical simulations are shown with filled-in circles. It is shown that the numerical results are in good agreement with analytical solutions.

4.1.1.2 Validation of electrohydrodynamics

In order to validate the code for implementation of the electric forces, the deformation of a stationary droplet in a quiescent fluid is compared with analytical solutions of Taylor [8] and Feng [11]. Accordingly, the deformation index of the droplet D is calculated as the fraction of the difference of droplet vertical (ς) and horizontal (ϱ) diameters over their summation

$$D = \frac{\varsigma - \varrho}{\varsigma + \varrho}. \quad (4.1)$$

It should be noted that the positive values of deformation index indicates the deformation of the droplet in the direction of electric field (prolate deformation) and its negative values represents the deformation perpendicular to the direction of the electric field (oblate deformation). Similar data can be obtained from analytical results of Taylor which can predict the deformation index as

$$D = \frac{9}{32(2 + \mathcal{C})^2} \frac{\varphi_T}{\gamma} \frac{\varepsilon_f E_\infty^2 d}{\gamma} = \frac{9}{32(2 + \mathcal{C})^2} \text{Ec}, \quad (4.2)$$

where φ_T is the Taylor discrimination function and can be found as,

$$\varphi_T = \mathcal{C}^2 + 1 - 2\mathcal{P} + \frac{3}{2}(\mathcal{P} - \mathcal{C}). \quad (4.3)$$

In the above equation Ec is the Electro-capillary number and defined as $\text{Ec} = \varepsilon_f E_\infty^2 d / \gamma$. Similarly, Feng [11] introduces an analytical solution for the deformation of a circular droplet under the effects of electric field as

$$D = \frac{\varphi_F}{6(1 + \mathcal{C})^2} \frac{\varepsilon_f E_\infty^2 d}{\gamma} = \frac{\varphi_F}{6(1 + \mathcal{C})^2} \text{Ec}. \quad (4.4)$$

where φ_F is the Feng discrimination function,

$$\varphi_F = \mathcal{C}^2 + \mathcal{C} + 1 - 3\mathcal{P}. \quad (4.5)$$

In order to compare numerical results with those obtained by using Taylor and Feng theories quantitatively, Table 4.1 is presented. In this table, the droplet deformation index D is presented for five different sets of simulation conditions. As one may infer from the sign of evaluated droplet deformation D in Table 4.1,

TABLE 4.1: The comparison of Taylor’s and Feng’s analytical solutions with present ISPH results for the deformation index D for different combinations of conductivity and permittivity ratios.

\mathcal{P}	\mathcal{C}	E_∞	Taylor’s theory	Feng’s theory	Present study
0.5	2	1	0.065	0.061	0.085
0.5	2	1	0.109	0.102	0.130
0.5	3	1	0.143	0.120	0.168
0.5	0.05	1	-0.045	-0.063	-0.061
5	0.5	1	-0.139	-0.196	-0.229

the input parameters given in the first three rows of the table lead to prolate deformation while the input parameters in the fourth and fifth rows causes the droplet to deform in the oblate form.

One may notice from Table 4.1 that for small deformation index values in both oblate and prolate conditions, the results of numerical simulations agree very well with those of analytical analysis except that there are rather small deviations between the analytical and simulation results. However, for relatively higher values of the droplet deformation index, the results of numerical simulations deviate observably from those of both theories. It is important to state that the theoretical analysis of both Taylor and Feng assume that the droplet remains circular hence being accurate for small droplet deformations only. Therefore, our findings matches with what have been reported in literature [10, 12, 81] wherein it was shown both experimentally and numerically that for large droplet deformations, these two analytical expressions underestimate the droplet deformation index. Another important point worthy of mentioning here is that for the prolate deformation, our results are closer in magnitude to those of the Taylor’s theory. On the other hand, when the droplet oblates, our findings have better agreement with the results of the Feng’s theory rather than the Taylor’s theory. In other words, in the prolate deformation, the Taylor’s theory calculates higher values for the droplet deformation index and the relative difference between Taylor data and ours are less than the Feng’s theory. Yet, in oblate deformation, the opposite situation is observed. The reason for such a controversy is hidden in equations (4.2) and (4.4) where in Feng’s theory, the inner fluid permittivity is used while in Taylor’s theory, the droplet deformation index is evaluated using the outer fluid’s permittivity.

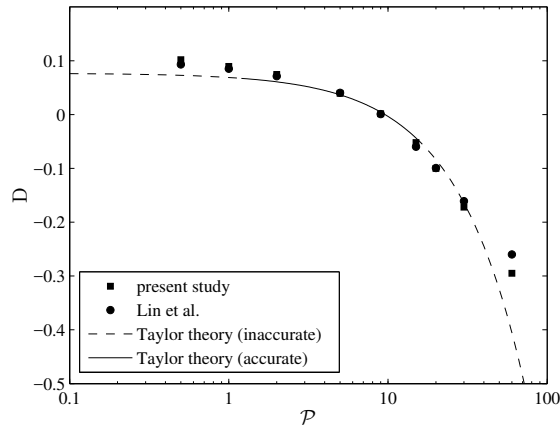


FIGURE 4.2: Comparison the deformation index of present numerical results (square marks) with Lin *et al.* [42] (circle marks) and Taylor’s theory [82] (dashed and solid lines) for the deformation of a neutrally buoyant bubble; The parameters are set to $\mathcal{D} = 1$, $\mathcal{V} = 1$, $\mathcal{C} = 5$, and $Ec = 0.4$.

4.1.2 EHD validation of the Fluent code

In order to validate the code for implementation of the electric forces in the Fluent UDF, the deformation of a stationary bubble in a quiescent fluid is simulated. The bubble is located in an axisymmetric domain of ($H = 12(d/2)$) and ($W = 6(d/2)$) where the distance of the bubble center from the top and bottom boundaries are the same. No-slip condition along with a potential difference of $E_\infty = \Delta\phi/H$ is applied to top and bottom walls. The left and right boundaries are the domain axis and the side wall, respectively. The right boundary abides the no-slip boundary condition and a Neumann boundary condition for the electric potential. In the absence of the bubble, this produces a uniform downward electric field parallel to the side walls. The density, viscosity and conductivity ratios are $\mathcal{D} = 1$, $\mathcal{V} = 1$, and $\mathcal{C} = 5$, respectively, and the applied electric potential yields the Electro-capillary number of $Ec = 0.4$. Figure 4.2 compares the deformation index of the test case for variations of electric permittivity ratio with Taylor’s theory [8] and numerical results of Lin *et al.* [42] for an inviscid system.

In figure 4.2, square and circle signs indicate the numerical results of present study and those of Lin *et al.* [42], respectively and Taylor’s theory is shown with solid and dashed lines. It should be noted that the Taylor’s theory gives accurate results for small deformations where the bubble is nearly spherical, but in high deformation cases, the results of the Taylor’s theory become inaccurate [9, 11, 81]. Therefore, the dash line illustrates the inaccurate Taylor’s theory while the solid lines indicate the region where the theory is accurate. The comparison of the present study with

referenced numerical and analytical results illustrates that in the region of small deformation, the deformation index is predicted with a sufficient accuracy. For large oblate deformations, the present results stand between the referenced numerical and analytical results while for the large prolate deformations, the current study slightly overestimates the deformation index compared to both referenced data.

Chapter 5

Results

5.1 Rayleigh-Taylor Instability (RTI)

The interfacial region established due to the vicinity of multiple streams of immiscible fluids has been a subject of many studies, both numerical and experimental. Of utmost interest has been the case of two phase system which is manifested in many different flow configurations and plays an important role in many industrial and natural phenomena such as cavitation, boiling heat transfer and astrophysics. When two sheets of fluid of different densities are subjected to a pressure gradient in a direction which is not parallel to the density interface, an unstable condition coined by Rayleigh [83] and Taylor [84] will be formed. The initial stages of the instability have been investigated by Chandrasekhar [85] and Mikaelian [86] and shown to have linear growth with respect to Atwood number. Further investigation on long term evolution of the Rayleigh-Taylor Instability (RTI) have been carried out by Goncharov [87] and Abarzhi *et al.* [88], among others, to provide models for continuous bubble and spike evolutions from their earlier exponential growth to the nonlinear regime.

While RTI depends upon gravitational acceleration to initiate the motion of the flow configuration, buoyancy is but one of the many destabilizing agents available in two phase flow systems. It is possible to excite an otherwise stable flow configuration into motion by exposing it to an external electric field. Gross and Porter [89] have reported such observations for a thermally and gravitationally stable stratified fluid, stating that a fluid with an inhomogeneous dielectric constant will experience destabilizing forces when subjected to an external electric field. Electrically excited RTI has been the subject of many studies [90–94]. Raco [90] and

Dong *et al.* [92] conducted studies regarding air-liquid and liquid-liquid interfaces reporting a direct relation between the intensity of the applied electric field and the behavior of the fluids. Later studies by Joshi *et al.* [93] and Barannyk *et al.* [94] show that the degree of instability may be controlled by the choice of electrical properties and field intensities.

There have been several investigations of RTI within Smoothed Particle Hydrodynamics (SPH) framework [95–97]. However, the combination of the two destabilizing agents, electric field and gravity, has not been fully investigated. In this study, the effect of presence of an external electric field on the evolution of RTI-like instability in a confined domain has been investigated numerically using Incompressible SPH (ISPH).

5.1.1 Problem Set-up

Figure 5.1 provides a schematic view of the computational domain used during the simulations conducted in this study. A rectangle of height $H = 4$ and width $W = 1$ is discretized by 320×80 particles arranged in an equally spaced formation. Different phases are marked according to their positions relative to the interface coordinates, $x_{(s)}$ and $y_{(s)}$, defined as

$$y_{(s)} = 2 + \xi_s \cos(kx_{(s)}), \quad (5.1)$$

where particles above the interface are considered to belong to the heavier fluid marked by subscript h and those remaining underneath are assigned to the lighter one designated by subscript l . Disturbance amplitude, ξ_s , is taken to be 0.025 and the wave number k is equal to $2\pi/\lambda$ with λ taken equal to the width of the computational domain, W . During the simulations conducted in this study, heavier fluid penetrates the lighter one due to the presence of gravitational acceleration, g , pointing vertically downward.

Boundary conditions are applied through Multiple Boundary Tangent (MBT) [98] method where all bounding walls are assumed to abide the no-slip condition while a zero gradient condition is enforced for pressure. A uniform and steady electric field of magnitude $E_\infty = \Delta\phi/H$ pointing downward and parallel to side walls is generated by applying constant electric potential difference, $\Delta\phi$, to the horizontal plates.

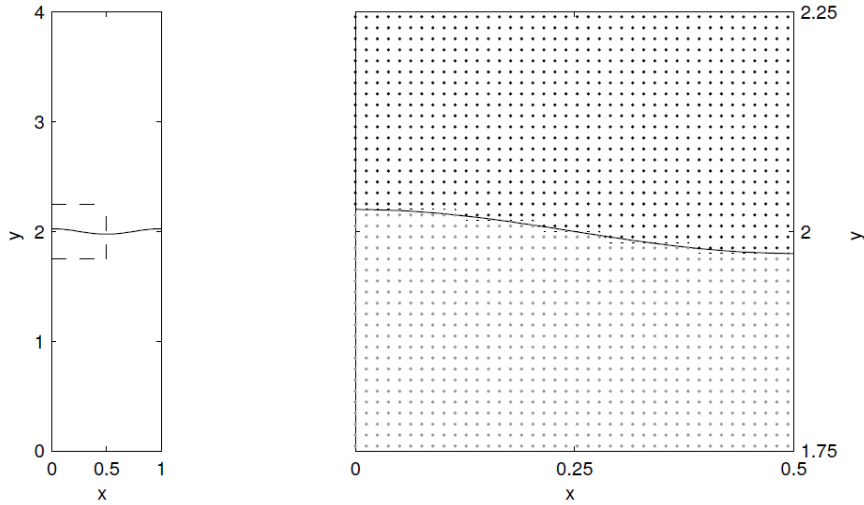


FIGURE 5.1: Initial condition used for simulations. (left) Whole domain; solid line shows the intended interface as defined in (5.1); heavy fluid on top, light fluid at the bottom. (right) Close up view of the portion included between the dashed lines on the right showing the initial particle positions in the vicinity of the interface. Solid line shows the intended interface profile while dashed line is the acquired interface profile calculated as 0.5 level contour of the color function.

Densities and viscosities of the fluid phases are assumed to be identical for all of the simulations carried out during this study. While both phases are assumed to have unit viscosity, a density ratio of 2 leads to an Atwood number of $At = (\rho_h - \rho_l) / (\rho_h + \rho_l) = 1/3$. Surface tension coefficient and gravitational acceleration's effects are combined in Bond number defined as

$$Bo = \frac{\rho_h g W^2}{\gamma} \quad (5.2)$$

while dimensionless time and positions are defined as

$$\begin{aligned} t &= t^+ \sqrt{gW}, & x &= x^+/W, & y &= y^+/W, \\ h_s &= h_s^+/W, & h_b &= h_b^+/W, \end{aligned} \quad (5.3)$$

where a plus sign represents dimensional variables, and h_s and h_b denote spike and bubble tip positions, respectively.

Electric field magnitudes and electric conductivities and permittivities of phases differ among different test cases and are stated in tables provided in each of the following sections.

The accuracy of the numerical method employed here has been tested out through

TABLE 5.1: Simulation parameters for comparison of forces due to the applied electric field

Case	Bo	At	E_∞ (V/m)	ε_h (F/m)	ε_l (F/m)	σ_h (S/m)	σ_l (S/m)
B	100	0.33	1	0.5	1	150	50
C	100	0.33	1	1	0.5	50	150

multiple simulations which were carried out separately for Rayleigh-Taylor Like Instabilities [44]. Consequently, such calculations have been left out for the sake of brevity.

5.1.2 The Comparison of Interfacial Forces

Figure 5.2 shows the comparison of interfacial forces for two cases having two different force configurations. In this figure, the arrows and filled contours respectively indicate the direction and the magnitude of the force vectors. The left column of figure 5.2 shows the forces corresponding the case at which the direction of the permittivity gradient vector is from the heavier fluid toward lighter fluid wherefore the electrical polarization force (the second term in equation (2.14)) points toward heavier fluid from the lighter one. As for the Coulomb force (the first term in equation (2.14)), it mainly acts from the heavier fluid into lighter one. The right column represents the inverse force configuration that can be achieved by enabling the permittivity gradient vector directed from the lighter fluid to heavier one, thereby resulting in the polarization and electric field forces to be in the opposite direction with respect to the case given in the left column. In this figure, the interface is shown for the dimensionless time of $t = 4.74$ at which the spike has started to have a mushroom like shaped front. Table 5.1 provides important simulation parameters for these two cases.

As it is apparent from equation (2.14), the electrical polarization force needs to be perpendicular to the interface while the orientation of the electric field force should be dependent on the interface profile and the direction of permittivity gradient vector as well as the applied electric field direction. For the cases shown in figure 5.2, the polarization force has greater magnitude on the frontier and main-stem of spike for case B and on the bubble frontier for case C. Similarly, the electric field force is concentrated on the spike tip for case B and on the bubble frontiers for case C. The comparison of magnitudes of the polarization and electric field forces at the bubble and spike frontiers of both B and C cases clearly reveals that the electric field force is dominant over the polarization force on the tip positions of

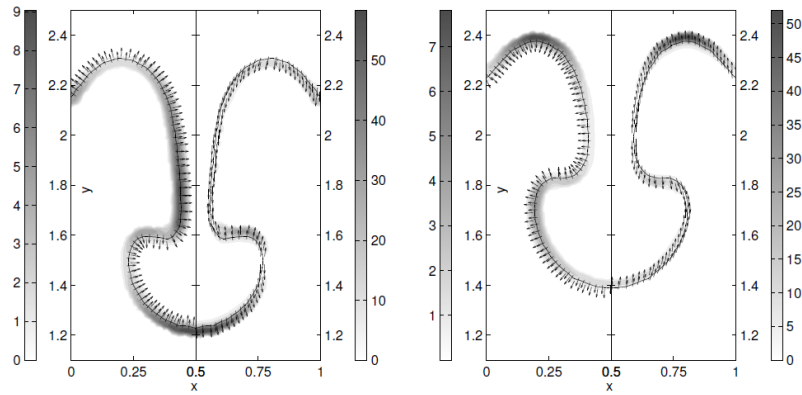


FIGURE 5.2: Comparison of components of the resultant electric force at $t = 4.74$; (left column) case B; (right column) case C. The left sub-column shows polarization forces while the right sub-column gives electric field forces. The direction and magnitude of the forces are respectively indicated by arrows and filled contour levels.

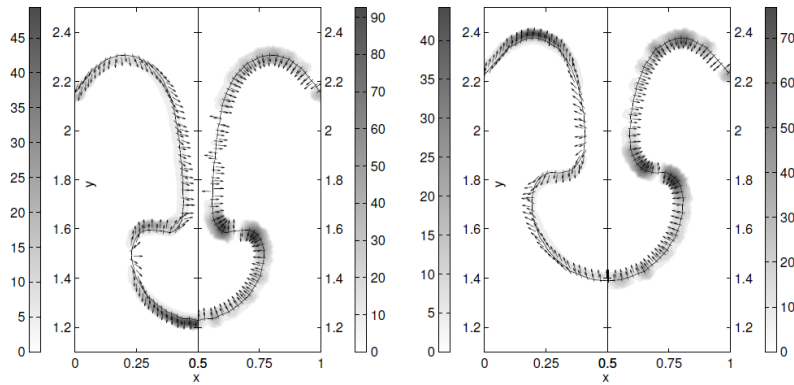


FIGURE 5.3: Comparison of the resultant electric force and surface tension force at $t = 4.74$; (left column) case B; (right column) case C. The left sub-column shows the resultant electric force while the right sub-column gives surface tension forces. The direction and magnitude of the forces are respectively indicated by arrows and filled contour levels.

bubble and spike. On the other hand, the polarization force is obviously much greater than the electric field force on the stem of the spike where the interface is almost in the direction of applied electric field. Stated otherwise, in this region, the electric field force is negligible due to the rather small value of volume charge density (q^v) that can be inferred from equation (2.9). For both case B and C, on the stem the polarization force acts in the transversal direction while the electric field force acts nearly parallel to the interface. Further observation of figure 5.2 for case B reveals that the electric field force (dominant over the polarization force in the vicinity of tips of the spike and the bubble) tends to fasten the penetration of spike into the lighter fluid and slows down rise of the bubble into the heavier

fluid. The polarization force which is dominant over the electric field force for the stem affects the main stem by imposing an inward force to the heavier fluid from the lighter one, resulting in a narrow spike stem. As for the case C, the electric field force dominates the bubble and spike tip positions with the force direction opposite to that of case B, while the polarization force acts on the main stem area in such a way that it leads to thickening of main stem.

Figure 5.3 shows the comparison of the resultant electric force and the surface tension force. As the surface tension force is proportional to the interface curvature, equation 2.4, the surface tension force is concentrated at sharper corners. At this stage of instability, a surface tension force concentration is observed at spike saddle regions (where the stem and the mushroom head of the spike merge) and at the bubble tip positions. On the other hand, the resultant electrical force is dominant in bubble and spike tip positions where the electric field force is much greater in magnitude than the polarization force.

The left sub-column of figure 5.3 shows that the resultant electric force is much larger at the spike frontier in the growth direction of instability for case B. On the bubble frontier, the resultant electric force is in the downward direction thereby acting in way of hindering the rising motion of the bubble. The comparison of the resultant electric force and surface tension force reveals that at the spike frontier, forces are competitive whereby the effect of surface tension to form a circular topology is reduced. At the tip position of bubbles, both the resultant electric and surface tension forces are directed with respect to interface such as to impede the rising motion of the bubble. Wherever the interface is parallel to the electric field direction, the polarization force affects the interface in the transversal direction by exerting a force from the lighter fluid to the heavier one. Such an effect is especially observable at the spike stem where the surface tension is negligible as the curvature tends to zero. Another region at which the polarization force may be deemed effective is at well-developed side-tails of spike at later simulation times. In these regions, the polarization force has similarly a narrowing effect. Therefore, once compared to non-electric field force simulation (case A in table 2), one may expect a faster growth of spike with narrower spike stem and side-tails and a slower rising motion of bubble. These effects may become augmented at higher magnitudes of electric permittivity values or electric field potentials.

The right sub-column of figure 5.3 shows that the resultant electric force is prevailing in the bubble frontiers for case C. At the spike frontier, the resultant electric force is in a reverse direction with respect to the growth direction of the instability.

TABLE 5.2: Simulation parameters for assessing the effect of electric force on the instability. Cases B and C are retabulated for the ease of comparison.

Case	Bo	At	E_∞ (V/m)	ε_h (F/m)	ε_l (F/m)	σ_h (S/m)	σ_l (S/m)
A	100	0.33	0	-	-	-	-
B	100	0.33	1	0.5	1	150	50
C	100	0.33	1	1	0.5	50	150

This assists the surface tension force to generate a slower growth of the instability for the spike tip position. On the bubble frontier, however, the resultant electric force counters the surface tension force resulting in a faster rising bubble. The lateral polarization force tends to thicken the spike stem by providing an outward force from the spike to the lighter fluid. The polarization force may also help to widen the mushroom head in the lateral direction. As a result, the spike has a larger frontier which experiences a larger drag force from the lighter fluid. Compared to non-electric field force simulation, the case of interest has a faster rise of bubble and slower descent of spike. A thicker spike stem and mushroom head are also expected.

5.1.3 The Effect of the applied electric field on the instability

To further assess the effects of the external electric field on the evolution of an unstable configuration, cases B and C are compared with case A, where no electric field is applied and the instability is only affected by gravity. Simulation parameters are specified in table 5.2.

Figure 5.4 shows time evolution of the aforementioned cases sorted from top to bottom corresponding to cases A, B and C of table 5.2, respectively. The first column of figure 5.4 shows the instabilities at $h_s = 1.66$ where the instability is at its initial stages before the mushroom-head of the spike has been formed. As can be noted from the figure, the polarization force plays its role at this stage by encouraging the formation of thicker spike stem and frontier for case C and a thinner one for case B. This effect is more pronounced in the second column given for $h_s = 1.32$. At this stage, the mushroom-head has been already formed for all cases. However, it is obvious that case C is more developed compared to the other two cases in terms of the head form of the spike and the mushroom-head formation of case B is prolonged due to the resultant electric force which tend to stretch and squeeze the spike head along the gravity and transversal directions

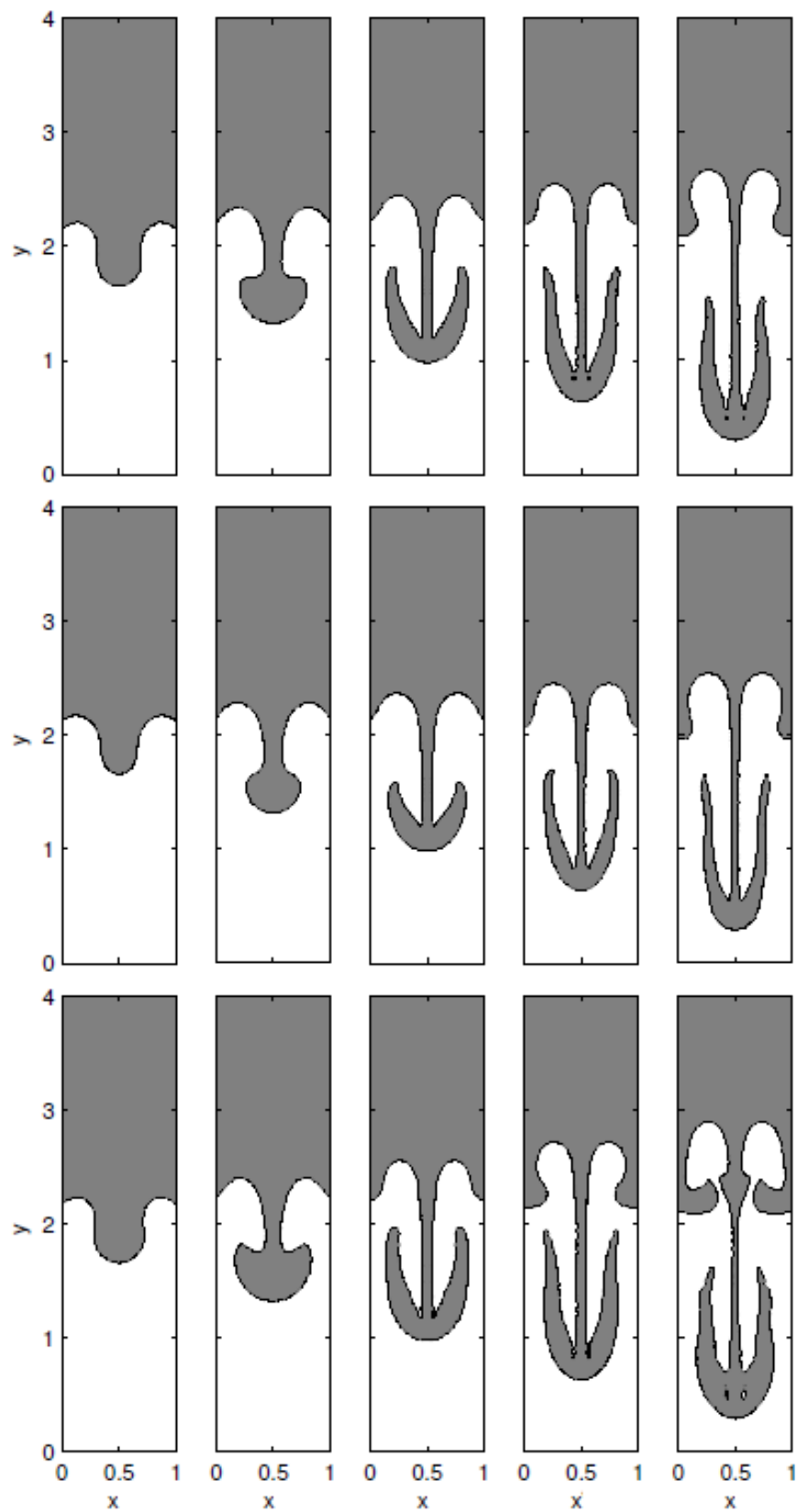


FIGURE 5.4: The evolution of the instability, represented by the 0.5 level contour of color function, for (top row) case A; (middle row) case B; (bottom row) case C. From left to right, snapshots are taken at spike positions of $h_s = 1.66, 1.32, 0.98, 0.64$ and 0.30 .

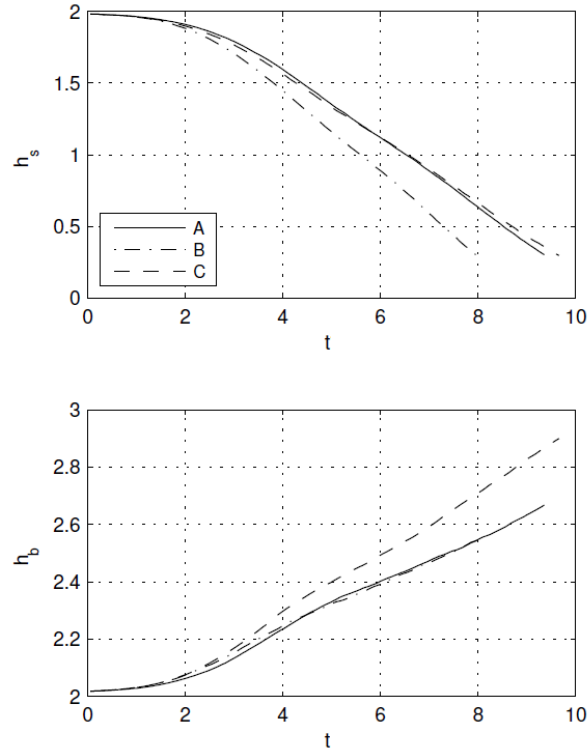


FIGURE 5.5: Normalized distance versus time for cases A, B and C (table 5.2); (top) spike tip position; (bottom) bubble tip position.

respectively. The third column represents the instability for $h_s = 0.98$ at which the side-tails have been developed at the spike region. The effect of polarization force at the spike stem is apparent. The spike stem is thicker in case C due to the outward force component from the heavier fluid to the lighter one. The same justification is valid for the bubble evolution. For case C, the size of bubble pair is smaller whereas the positions of bubble tips are higher than the other two cases. Considering the spike for case B, the total interface forces (the resultant electric and surface tension forces) act on the instability such that the volume of the penetrated heavier fluid is less than the other cases. The fourth column represents the flow topology for $h_s = 0.64$ where case B shows a thinner spike stem and side-tails. It has been mentioned before that the polarization force affects the spike side-tails and stem, imposing a force from lighter to heavier fluid for case B. As for the bubble, its rising motion is mainly promoted by the hydrodynamic forces due to the spike penetration in addition to the buoyancy force recalling that the rise of the bubble is impeded by the total interface forces. The so referred hydrodynamics force becomes present due to the replacement of the lighter fluid by the heavier one as the spike falls down, which pushes the bubble in the upward direction. For case C, the bubbles are inclined toward the boundary walls by the exertion of the polarization force at the spike stem root which is from the heavier

fluid to the lighter one. Another reason for this behavior may be found in the side currents of heavier fluid in the vicinity of wall boundaries which experience a lateral force causing further penetration into the bubble region. An undeveloped form of bubble entrapment is observable at the final stage of the flow evolution at $h_s = 0.3$ which is due to the side currents and formation of secondary instabilities on the spike stem.

The influence of the resultant electric forces on the growth of the instability may be further demonstrated by investigating the temporal evolution of bubble and spike tip positions. Figure 5.5 shows the normalized positions of the tip of bubble and spike for the three test cases in table 5.2. The spike tip position shows that the case B differs from the other two cases in terms of having a faster penetration of spike while the case C features a faster bubble rising. Recall that for cases having a permittivity gradient vector from lighter to heavier fluid such as case C, the resultant electric force concentrates at the frontal region of the bubble. This force is comparable to surface tension force at this region and enables a faster rising motion of the bubble. At the spike region, however, the resultant electric force has much lower magnitudes compared to surface tension force wherefore the growth of the spike for the case C shows a similar behavior to that of the non-electric force case. A similar reasoning can be made for case B where the resultant electric force is concentrated at the tip position of the spike. The magnitude of the resultant electric force at the tip region of the spike is also comparable to the surface tension force at this region thereby reducing the effect of the surface tension force on the growth of the spike and in turn promoting the spike penetration. Contrarily, at the bubble region of case B, the resultant electric force is notably smaller than the surface tension force, and therefore, it does not affect the motion of bubble considerably.

5.1.4 Effect of Electric Permittivity Variations

As one of the influential parameters in the resultant electric force magnitude and direction in equation (2.14), the electric permittivity values have a direct effect on the evolution of instabilities. In order to provide a better understanding of the extents of this effect, additional test cases have been simulated by changing permittivity values whilst keeping their ratio constant.

Table 5.3 presents the simulation parameters of simulation sets D and E. The simulation parameters of cases D-1 to D-5 bear resemblance to case B in terms of

TABLE 5.3: The comparison of various electric permittivity values

Case	Bo	At	E_∞ (V/m)	ε_h (F/m)	ε_l (F/m)	σ_h (S/m)	σ_l (S/m)
D-1	100	0.33	1	0.125	0.25	150	50
D-2	100	0.33	1	0.25	0.5	150	50
D-3	100	0.33	1	0.5	1	150	50
D-4	100	0.33	1	1	2	150	50
D-5	100	0.33	1	2	4	150	50
E-1	100	0.33	1	0.25	0.125	50	150
E-2	100	0.33	1	0.5	0.25	50	150
E-3	100	0.33	1	1	0.5	50	150
E-4	100	0.33	1	2	1	50	150
E-5	100	0.33	1	4	2	50	150

the direction of the electric permittivity gradient vector which is from the heavier fluid to lighter one, thus enhancing the spike penetration and resisting the rising motion of the bubble. As for the opposite scenario which happens when the permittivity gradient vector is from lighter fluid to heavier one, the relevant test cases include E-1 to E-5. It should be noted that cases D-3 and E-3 of table 5.3 are identical to cases B and C of table 5.2, respectively.

Figure 5.6 shows a well-developed stage of instability at $h_s = 0.3$ for D series at top, and E series at the bottom row of the figure. An overview of sub-figures indicates that the increase in permittivity values leads to more contribution from the resultant electric forces on the growth of the instability. For instance, the comparison of upper and lower sub-figures of the first column of this figure 5.6 does not represent a considerable difference between two cases.

A detailed observation of D series indicates that the resultant electric forces have a considerable effect on the topology of side-tails and the position of the bubble. It is clear that as the value of electrical permittivity increases, the side-tails get thinner and smaller while the bubble rise gets slower due to the previously discussed reasons. It should be also noted that the amount of heavier fluid penetrating into the lighter one decreases due to the formation of a narrower jet of heavier fluid with small side-tails for simulations with higher electrical permittivity values such as cases D-4 and D-5.

The lower part of figure 5.6 shows that the electric permittivity increment enforces the side currents along the vertical walls to enclose the bubble and form a bubble entrapment. The side currents which are resulted from the lateral polarization force triggers the formation of secondary instabilities at the main stem, which are shown for the case E-3 (the third column of figure 5.6). The comparison of the

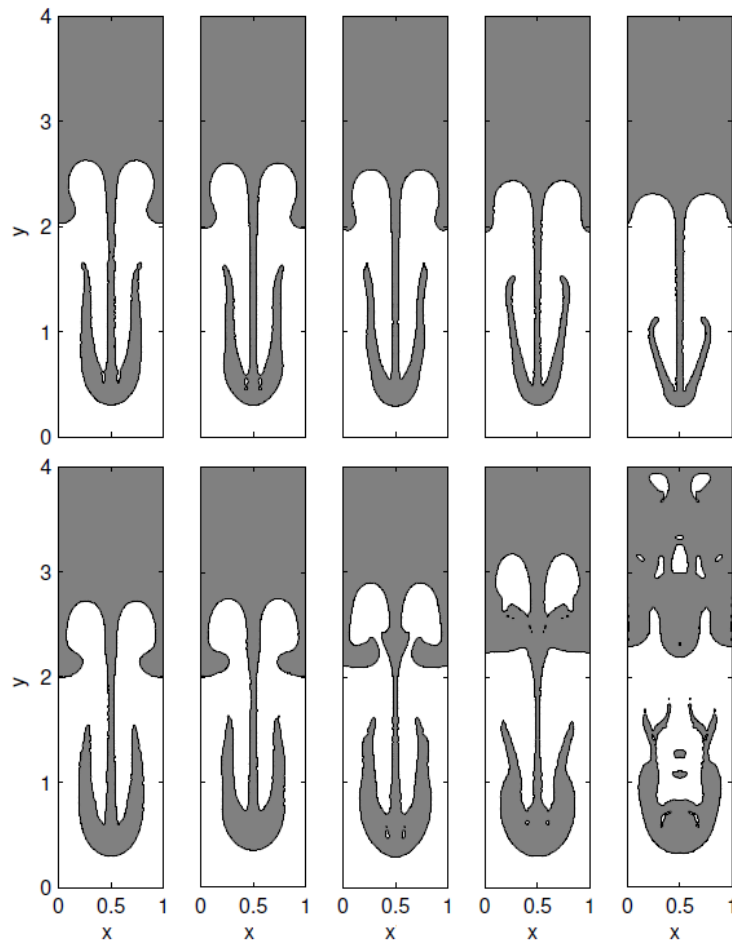


FIGURE 5.6: Snapshots of 0.5 level contour of color function at $h_s = 0.3$ for (top row) D series; (bottom row) E series. From left to right, snapshots correspond to case numbers 1 through 5 as set in table 5.3.

bubble growth shows that there is a notable difference among the given test cases in terms of the bubble positions, shapes, and flow complexity, which is due to the highly influential effect of the resultant electric forces at the bubble tip position as elaborated in detail previously.

Figure 5.7 shows the bubble and spike tip positions versus time for three selected test cases (D-1, D-3, and D-5) of table 5.3 until the spike tip reaches at the final position of $h_s = 0.3$. As mentioned previously, the resultant electric forces enhance the penetration of spike into the lighter fluid while hindering the rising motion of the bubble for the D series test case. Intuitively, one may expect that the bubble front position for case D-5 should be the smallest among others because of the resultant electric force which acts to hinder the upward motion of the bubble. However, at earlier time steps, this is not the observed case due to the fact that the resultant electric force on the tip of the spike causes the spike to descend

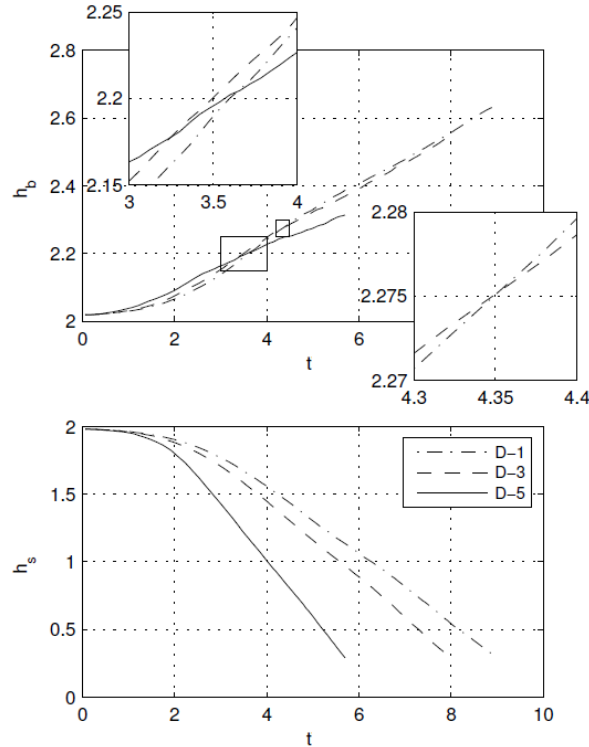


FIGURE 5.7: Normalized distance versus time for cases D-1, D-3 and D-5 (table 5.3); (top) spike tip position; (bottom) bubble tip position.

faster, thereby enabling the formation of strong hydrodynamics force due to the displacement of lighter fluid by the heavier one, which enhances the ascent of the bubble given that at early time steps, the bubble and spike tip positions are close to each other so that the motion of the spike can affect the bubble motion. A more detailed observation illustrates a turning point at dimensionless time around $t = 3.5$, after which this trend is reversed, meaning that the lower the electric permittivity, the higher the bubble position.

Similar to figure 5.7, figure 5.8 shows the bubble and spike tip positions for cases E-1, E-3 and E-5. In these cases, the resultant electric force is mainly dominant on the bubble tip position forming a faster rising bubble into the heavier fluid as the permittivity values increase. Figure 5.8 expresses that the spike tip positions of E series show a similar behavior to that of the bubble tip positions in D series. For E series, it is expected that the spike should descend slower in higher permittivity values due to the resisting nature of the resultant electric forces at the frontier of the spike. However, it is observed that for higher permittivity values, the front of the spike grows faster at earlier time steps. The turning point is observed to be around $4 < t < 5$. The same justification, as given for D series, is valid for present observation. More specifically, the fast rising motion of bubble which is generated

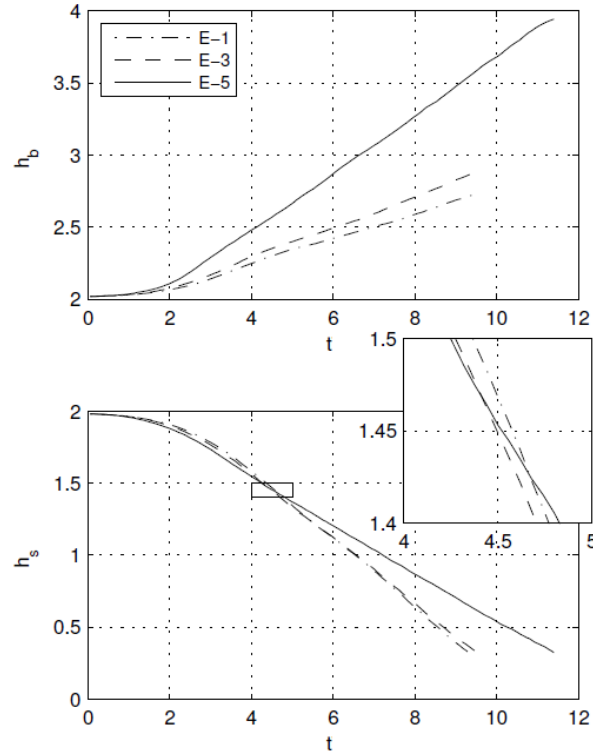


FIGURE 5.8: Normalized distance versus time for cases E-1, E-3 and E-5 (table 5.3); (top) spike tip position; (bottom) bubble tip position.

by greater resultant electric forces at its tip provides hydrodynamic forces to cause the spike to penetrate faster. At higher time steps, this force is not experienced by the spike, considering the more complicated profile at those time steps, resulting in slower growth for higher permittivity values.

5.1.5 Effect of Electric Field Strength Variations

Since the resultant electrical force is influenced by both the strength of electric field and the value of electric permittivity, the instability is also analyzed for varied electric field strengths and simulation parameters are presented in (table 5.4). Similar to previous section, the table is divided into two separate parts. The first one (the F series) is shown for the scenario in compliance with cases B and D series of previous sections. The other part of the table which is shown by G series is correspondent to cases C and E series.

Figure 5.9 shows the simulation results for F series at the top and G series at the bottom. The results are presented for $h_s = 0.3$ similar to what has been presented in previous sections. The strength of the electric field increases from

TABLE 5.4: The comparison of various electric field strengths

Case	Bo	At	E_∞ (V/m)	ε_h (F/m)	ε_l (F/m)	σ_h (S/m)	σ_l (S/m)
F-1	100	0.33	0.2	0.6	1.2	50	20
F-2	100	0.33	0.4	0.6	1.2	50	20
F-3	100	0.33	0.6	0.6	1.2	50	20
F-4	100	0.33	0.8	0.6	1.2	50	20
F-5	100	0.33	1	0.6	1.2	50	20
G-1	100	0.33	0.2	1.2	0.6	20	50
G-2	100	0.33	0.4	1.2	0.6	20	50
G-3	100	0.33	0.6	1.2	0.6	20	50
G-4	100	0.33	0.8	1.2	0.6	20	50
G-5	100	0.33	1	1.2	0.6	20	50

left to right in figure 5.9 for F and G series. For example, in the sub-figures given in the first column of figure in question have rather small values of the electric field strength, these two results do not show a considerable difference in the evolution of the instability. However, as the electric field strengths increases, the difference becomes more observable.

Considering the results of the simulations in F-series, it is seen that as the strength of the electric field increases, in light of the discussion on the resultant electric forces in previous section, one should expect that the ascent of the bubble is impeded, and the descent of the spike into the lighter fluid is promoted. The polarization force, being the dominant component of the resultant electric force in the transversal direction, leads to narrower stem and a pair of side-tails for the spike as the strength of the electric field increases. On the other hand, the G series experience the resultant electric force acting resistively to the growth of the spike while being in accordance with the ascent of the bubble. This results in a faster growth of bubble and slower penetration of heavier spike as the electric field strength increases.

Similar to the analysis that have been made for spike and bubble tip positions in previous section, the time history of bubble and spike tip positions for F (F-1, F-3 and F-5) and G (G-1, G-3 and G-5) series are presented in figures 5.10 and 5.11. In figure 5.10, with the increment of electric field strength, the spike penetrates faster which can be noted by comparing the dimensionless time $t = 7.98$ at $h_s = 0.3$ for case F-5 with the other two cases, which is 16 and 10 percent less than those of cases F-1 and F-3, respectively. The bubble tip position experiences a similar behavior reported formerly for the associated test cases (i.e., Case D-series). Apparently, for higher electric field strength, the bubble experiences more resistive force at its tip position. However, the hydrodynamic forces due to the

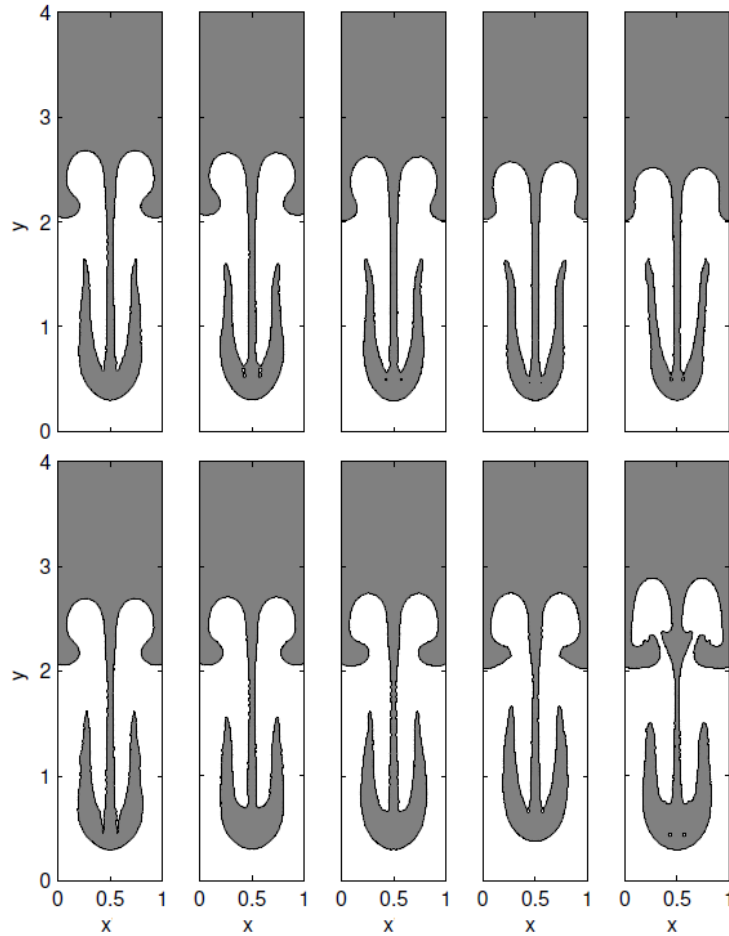


FIGURE 5.9: The evolution of the instability for different electric field strength, which is shown for $h_s = 0.3$ for all cases. The sub-figures at the top row represent the cases F-1 to F-5 of table 5.3, and the sub-figures at the bottom row represents the case G-1 to G-5 of the same table.

penetration of the spike into the lighter fluid affects the bubble motion, hence making it to ascend faster than that in test cases with lower electric field strength.

In figure 5.11 which is shown for bubble and spike tip positions of G series, the bubble rises faster for higher values of electric field strength. This can be quantified by showing that at the final stage where the spike reaches $h_s = 0.3$, the bubble tip position is $h_b = 2.89$ (for case G-5) comparing with cases G-1 and G-3 showing 29 and 18 percent increase, respectively. Moreover, setting the final stage shown here to be $h_s = 0.3$, the instability grows slower for higher electric field intensity cases. The dimensionless time of the instability evolution for case G-5 is 4.5 and 3.8 percent more than of cases G-1 and G-3. It can be noted that the percentage difference is less than that for the F series.

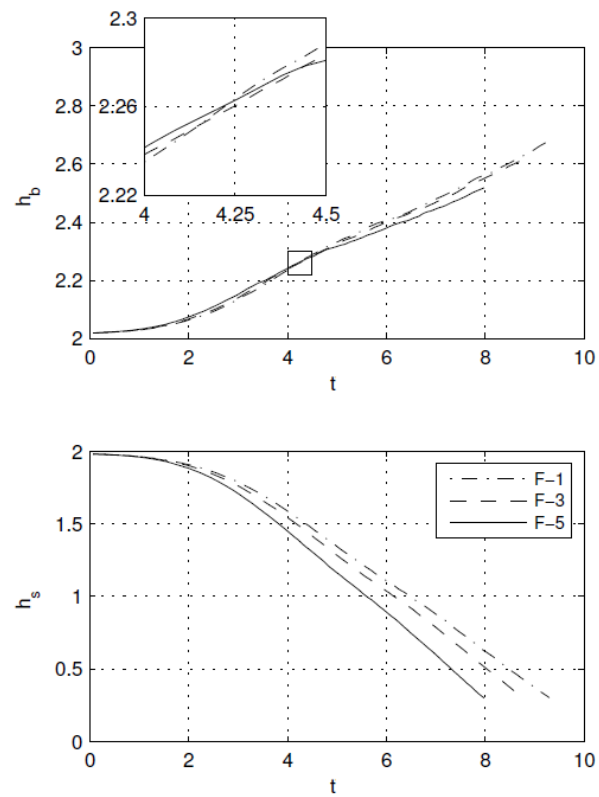


FIGURE 5.10: Normalized distance versus time for cases F-1, F-3 and F-5 (table 5.4); (top) spike tip position; (bottom) bubble tip position.

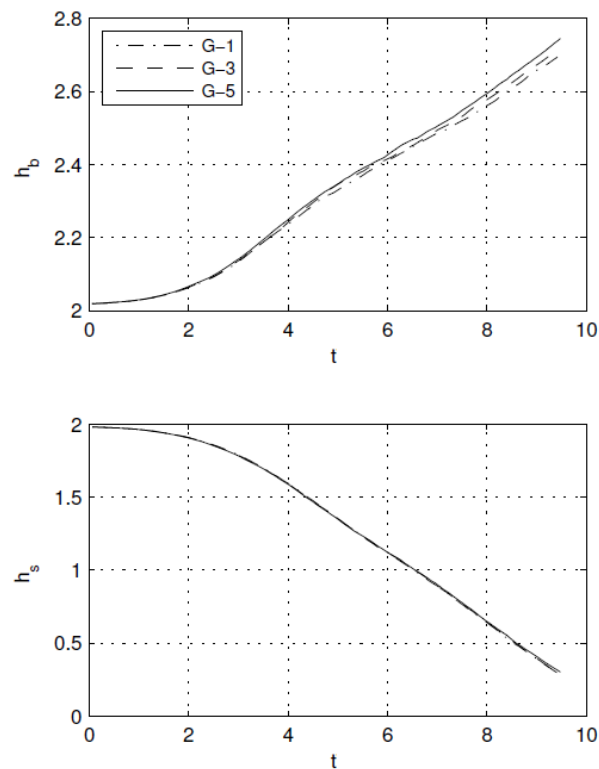


FIGURE 5.11: Normalized distance versus time for cases G-1, G-3, and G-5 (table 5.4); (top) spike tip position; (bottom) bubble tip position.

5.2 Bubble rising

The motion of a lighter fluid with a continuous interface in another heavier fluid due to the gravitational force is known as the bubble rising. In addition to numerous natural phenomena, there are plenty of industrial applications such as liquid separation and waste-water treatments [99, 100], nucleate pool boiling [101] and chemical reactions [102] where the bubble rising is frequently observed. In most of these applications, the bubble rising is normally accompanied by the deformation of the bubble due to external, environmental and geometrical parameters. Numerous studies have been carried out to investigate the effect of various parameters on the regimes of bubble rising. Clift [103] reviewed the bubble rising and illustrated that the motion of the bubble can be categorized by three dimensionless numbers, namely the Reynolds, Morton, and Eotvos numbers which the later can also be referred to as the Bond number. He showed that in small Reynolds and Bond numbers, the bubble remains spherical, but increments of both Reynolds and Bond numbers yield different bubble regimes such as elliptical and spherical caps, as well as ellipsoidal and wobbling shapes. Further investigations [63–65, 104] revealed that bubbles may deform to a toroid under sufficiently large magnitudes of Reynolds and Bond numbers.

Chen *et al.* [63] studied the bubble deformation and its rise for variations of Reynolds, Bond, density and viscosity ratios, and observed that the transition from an elliptical cap to a toroid is facilitated by means of a jet at the wake of the bubble. They concluded that such a transition occurs in density ratios of greater than 5, but the viscosity ratio does not have a significant effect on the bubble shape and velocity. They also realized that a toroidal bubble always travels slower than an elliptical or mushroom-shaped bubble. Bonometti and Magnaudet [64] investigated the transition from a spherical cap to a toroidal bubble and realized that the transition takes place by means of two different scenarios. In the first scenario, they mentioned that for large Reynolds numbers, an upward liquid jet is driven by the hydrostatic pressure difference between the two poles of the bubble. If surface tension can not compete with the force due to the upward jet current, the bubble is pierced. The piercing occurs at the Bond number $32 \leq Bo \leq 35$. The piercing due to the second scenario occurs in the absence of surface tension force. If the viscous effects are not sufficiently strong to sustain the local pressure maximum at the bubble front, a toroidal bubble is formed. The second scenario is found to take place in Reynold number $79 \leq Re \leq 84$. Later, Hua and Lou [65] numerically studied the bubble rising and reported that for constant magnitudes

of Reynolds, Bond, density and viscosity ratios, a toroidal bubble is more likely to be formed when the bubble has an initial prolate shape compared to an initially oblate one. Nonetheless, these bubble regimes can also be affected by other parameters such as external forces and domain constraints.

In order to control the bubble rising conditions and maintain the preferable flow regime and rising characteristics, various techniques have been examined in the literature. Investigated both numerically [2, 105] and experimentally [1, 106], adding surfactants to the multi-phase system can adjust the surface tension to a desired value, resulting in proper control of the bubble rising regimes. However, there are limitations in the usage of surfactants in multi-phase flow systems. For instance, some surfactants are hazardous and have serious impacts on human-being and animal lives [3, 107]. Alternatively, the utilization of magnetic and electric forces is another feasible solution for controlling the bubble rising phenomenon. There are numerous experimental [4] and numerical [5, 108] works investigating the influence of magnetic field on the bubble rising. Yet, the electrohydrodynamic effects on the rising bubble have not been fully discovered.

Mahlmann *et al.* [21] carried out a two-dimensional simulation of a gas bubble rising in a viscous fluid under the perfect dielectric assumption. They investigated the deformation of a rising bubble for variations of electric field strength, surface tension and viscosity. They revealed that the bubble initially deforms into a prolate shape and later flattens into an oblate one thereby experiencing "wobbly-like" oscillations. It was also shown that in presence of electric field, the bubble is more stretched in the direction of the electric field, resulting in an increase in the rising velocity of the bubble. Wang *et al.* [22] simulated a similar case and showed that the increase in the electric field strength can induce separations of the tail of the bubble. Consequently, the jet above the bubble is strong enough to turn the spherical bubble to a toroidal shape. Finally, Yang *et al.* [109] studied the bubble rising under horizontal and vertical electric fields using a perfect dielectric model, numerically. They showed that vertical electric field enhances the rising motion of the bubble while the horizontal electric field hinders the rising motion.

5.2.1 Bubble rising of an oil-water system

Considering the governing equations explained in chapter 2, dimensionless values are formed using the following scales

$$\begin{aligned} \mathbf{x} &= \mathbf{x}^+/r, & \rho &= \rho^+/\rho_f, & \mu &= \mu^+/\mu_f & \mathbf{u} &= \mathbf{u}^+/\sqrt{gr}, \\ t &= t^+\sqrt{g/r}, & \mathbf{E} &= \mathbf{E}^+/E_\infty, & p &= (p^+ - \rho\mathbf{g} \cdot \mathbf{x}^+)/\rho_f gr, \\ \mathcal{D} &= \rho_b/\rho_f, & \mathcal{V} &= \mu_b/\mu_f, & \mathcal{P} &= \varepsilon_b/\varepsilon_f, & \mathcal{C} &= \sigma_b/\sigma_f, \end{aligned} \quad (5.4)$$

leading to Reynolds, Bond, electro-gravitational and electrical capillary numbers defined as

$$\text{Re} = \frac{\rho_f \sqrt{gr^3}}{\mu_f}, \quad \text{Bo} = \frac{\rho_f gr^2}{\gamma}, \quad \text{Eg} = \frac{\rho_f gr}{\varepsilon_f E_\infty^2}, \quad \text{Ec} = \frac{\text{Bo}}{\text{Eg}}. \quad (5.5)$$

Here r is the bubble radius, E_∞ is the undisturbed electric field intensity. A plus sign marks dimensional variables whereas subscripts \square_b and \square_f denote bubble and background fluid phases, respectively.

5.2.1.1 Problem set-up

The schematic of the test case considered in this study is shown in figure 5.12. The bubble is placed at a height of $h_d = 2r$ above the bottom wall in a rectangular computational domain with a height and a width of $H = 10r$ and $W = 6r$, respectively. No-slip boundary condition along with a potential difference of $E_\infty = \Delta\phi/H$ is applied to top and bottom walls denoted with solid lines while the periodicity condition is implemented on the side boundaries, demarcated with dashed lines in figure 5.12. In the absence of the bubble in the computational domain, the periodic boundary condition for the electric potential produces a uniform downward electric field parallel to the side boundaries. Particles discretizing the bubble are positioned along concentric circles around the bubble's center. The radii of consecutive circles differ by one particle spacing and the outermost circle's radius is equal to r . The number of particles along each of these circles vary to keep the overall inter-particle spacing uniform. Fluid particles are arranged on a uniformly spaced Cartesian grid where particles coinciding with the bubble are removed.

In addition to the validations presented in chapter 4 for the implementation of surface tension and the EHD forces on the deformation of a quiescent bubble, the in-house code and the numerical algorithm used here were extensively validated

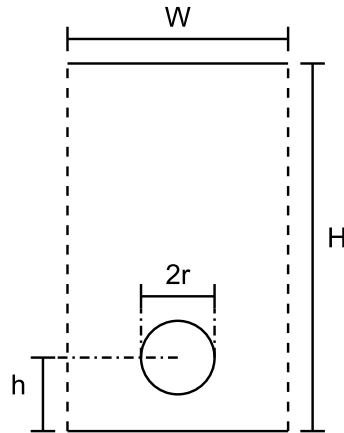


FIGURE 5.12: Schematic of the test case.

via comparing the results of bubble rising simulations with those from Hysing *et al.* [110] and Susmann *et al.* [67], in the studies of our former group member in [76]. However, to present a self-contained study here, we have performed further validations through numerically simulating a bubble rising problem with and without electric field, and compared with level-set results of Mahlmann *et al.* [21]. The computational domain is an enclosed rectangle similar to figure 5.12, but the dimensions of the computational domain are set to those given in [21], namely, $W = 7r$, $H = 14r$ and $h = 2r$. In this section, horizontal boundary conditions are similar to what is employed for the rest of the simulations explained in previous part.

To be compatible with those simulated in [21], however, vertical boundaries are treated as solid walls with no-slip boundary condition while as for the boundary conditions for the electric potential, the Neumann boundary condition is imposed on vertical walls. Both cases have $Re = 250$ and $Bo = 1$, while the electrified case has the electrical capillary number of $Ec = 1$. Figure 5.13 compares the bubble shapes and centroid vertical velocities of non-electrified and electrified cases with those of Mahlmann *et al.* [21]. The results for the non-electric test case have a clear match both in terms of the bubble shape and its vertical velocity. In the electrified case, both shape and the motion of the bubble are in a satisfactory agreement with those of Mahlmann except at a stage where the bubble is close to the boundary. This deviation might be attributed to the possible difference in the resolution of electric field near the boundary.

In order to rely on the numerical results, the dependency of the results to the particle resolution is tested. The resolution of the particles is scaled with respect to the bubble diameter; the number of particles for a unit diameter of bubble

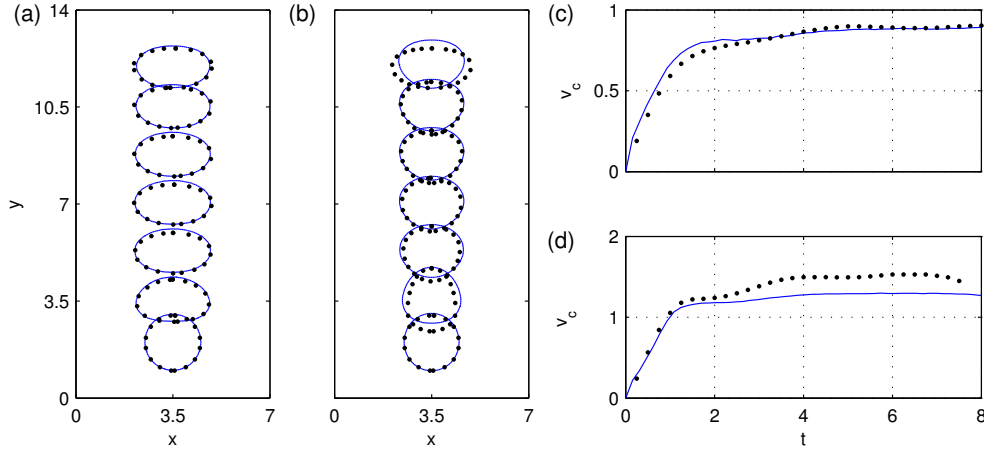


FIGURE 5.13: The comparison of the bubble shape and centroid velocities for non-electrified (a,c) and electrified (b,d) cases of the present study with Mahlmann *et al.* [21] where the solid line corresponds to the results of the current study.

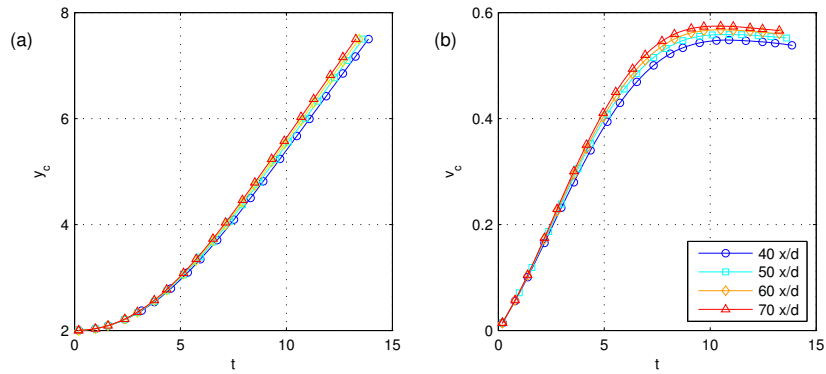


FIGURE 5.14: The temporal evolution of centroid positions and velocities of the validation test case with dimensionless parameters of $Re = 400$, $Bo = 12$ and $Ec = 5$ for six different particle resolutions.

(x/d). In order to perform the test, a case with dimensionless numbers equal to $Re = 400$, $Bo = 12$ and $Ec = 5$ is simulated for different particle resolutions. The resolution is varied from 40 x/d to 70 x/d with a unit increment of 10. Figure 5.14 shows the bubble centroid positions and velocities for these particle resolutions. It is observed that the solution converges when the particle resolution increases. The centroid position of 60 x/d and 70 x/d adequately matches, and their velocities at both the accelerating and terminal stages have negligible difference. Thus, in this study, the particle resolution of 60 x/d is used to simulate the validation and forthcoming test cases.

The rising of a single bubble in a quiescent fluid can be modeled using four dimensionless numbers, namely the density ratio \mathcal{D} , the viscosity ratio \mathcal{V} , the Reynolds

TABLE 5.5: The dimensionless parameters and their corresponding magnitudes and/or ranges that is being used in this study

Parameter	\mathcal{D}	\mathcal{V}	\mathcal{P}	\mathcal{C}	Re	Bo	Ec
Value	0.8	100	0.05	0.01	100 – 400	2 – 12	0 – 5

number Re and the Bond number Bo. The introduction of electric forces to the bubble rising problem adds three new dimensionless parameters to the numerical model. These parameters are electrical permittivity \mathcal{P} and conductivity ratios \mathcal{C} , and electrical capillary number Ec. In order to simulate the bubble rising for an oil-water system, the Reynolds, Bond and electrical capillary numbers are employed to consider the various conditions of bubble rising of an oil-water system. Table 5.5 presents the dimensionless parameters for an electrified bubble rising and their magnitudes and/or ranges used in this work. It should be noted that the case with simulation conditions of [Re = 400, Bo = 12, Ec = 5] is a base case named *ERB*, which is used in all forthcoming comparisons of electrical capillary, Reynolds and Bond numbers in the following sections.

The leaky dielectric model assumes a finite electrical conductivity thereby taking into account the effect of electric charges on the interface [8, 13]. As a result, the bubble is deformed prolately in the direction of electric field or oblately perpendicular to the electric field direction. Feng [11] introduced a discrimination function $\varphi_F = \mathcal{C}^2 + \mathcal{C} + 1 - 3\mathcal{P}$ which determines the shape of the deforming bubble. The positive value of φ_F causes the prolate deformation while the negative value leads to the oblate deformation. In this paper, the discrimination function is calculated to be $\varphi_F = 0.86$, requiring the bubble to deform into a prolate shape if the gravitational force is absent. However, the deformation of the bubble rising in the presence of gravitational and electric forces needs further investigation which is the premise of this study.

5.2.1.2 Effect of Electro-capillary number

In this section, the variation of electrical capillary number and its impact on the bubble rising is studied. The electrical capillary number is varied by changing the external electric field strength. The bubble is subjected to six different electric field strengths ranging from Ec = 0 to Ec = 5 with increments of unity. In this part, the Reynolds and Bond numbers are kept constant for all test cases (Re = 400, Bo = 12).

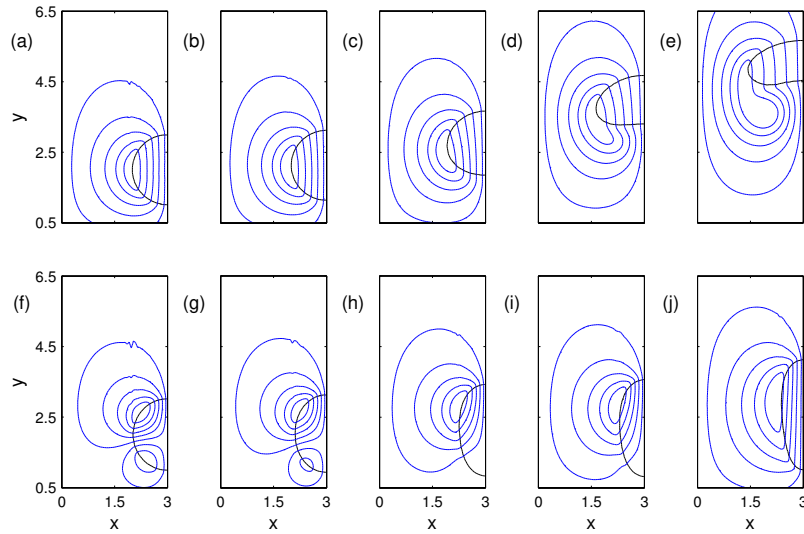


FIGURE 5.15: Bubble shapes and velocity streamlines for non-electrified and electrified cases at five early instants of the rising; The upper row shows the non-electrified case $Ec = 0$ at (a) $t = 0.4$, (b) $t = 10$, (c) $t = 5$, (d) $t = 9$ and (e) $t = 13$ while the bottom one represents the electrified case ERB , at (f) $t = 0.4$, (g) $t = 1$, (h) $t = 2$, (i) $t = 2.4$ and (j) $t = 4$.

In order to show the impact of electric forces on the bubble rising, figure 5.15 presents bubble shape and velocity streamlines in the half of computational domain at five early instants, sorted from left to right, for $Ec = 0$ and ERB cases shown at the top and bottom part of the figure, respectively. As can be observed from the figure, in the absence of the electric forces, the bubble rises forming an oblate shape due to the hydrodynamic drag at the bubble front. However, the application of a sufficiently large electric force elongates the bubble prolately. Considering the vortex formation for the $Ec = 0$ case, a single vortex is generated at the sides of the bubble at the early instances of the rising, but the vortex gradually moves towards the region behind the bubble. This induces an upward jet current of the surrounding fluid beneath the bubble, which promotes the formation of an oblate shape. As for the case of ERB , a pair of vortices is generated due to the electric forces [13]. The flow direction for these vortices can be determined by the comparison of conductivity and permittivity ratios. Based on the parameter setup of this study, these vortices encourage the bubble to elongate into the prolate shape at the early rising moments where the buoyancy effects are not significant. As the bubble ascends, the bottom vortex loses its strength due to the magnification of hydrodynamic forces and finally disappears. Simultaneously, the upper vortex grows and develops at the sides of the bubble.

To quantify the deformation of a bubble, we here introduce a dimensionless parameter, referred to as the aspect ratio, $A_r = \varsigma/\varrho$, where ς and ϱ are bubble diameters

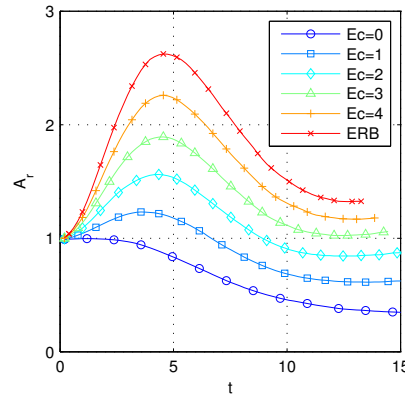


FIGURE 5.16: The temporal variation of aspect ratio A_r as a function of electrical capillary number Ec for six test cases.

in the vertical and horizontal directions passing the bubble centroid, respectively. Figure 5.16 shows the temporal evolution of the aspect ratio for all test cases studied in this part. The general trend of all test cases excluding the non-electric case of $Ec = 0$ demonstrates that the aspect ratio of the bubble increases, indicating that the bubble acquires a prolate shape due to the electric force. As the bubble gets slender, the pressure drag decreases while the friction drag increases, and the surface tension force becomes augmented at the poles of the bubble due to the increase in the curvature therein. After reaching a maximum value, the aspect ratio starts decreasing and reaches a plateau. The aspect ratio levels off when electrical and hydrodynamics forces balance each other.

The temporal evolution of centroid and bottom velocities of the bubble for different electrical capillary numbers is shown in figure 5.17. Figure 5.17-a indicates that the centroid velocity of the bubble increases with the rise of Ec . Comparing the resultant forces applied to bubble due to pressure, viscous stress and electric stresses, it is seen that the electric component is one order of magnitude smaller than viscous and pressure components (not shown). However, the electric forces implicitly affect the rising velocity by changing the bubble shape (figure 5.15). Applying the electric field makes the bubble more prolate, reducing the pressure drag while increasing the friction drag. The resultant drag is much less than when no electric field is applied, increasing the rise velocity of the bubble.

Figure 5.17-b presents the effect of electrical capillary number on the bottom velocity. It is observed that the bottom velocity attains a negative value except for $Ec = 0$ and $Ec = 1$ cases and its magnitude increases with incrementing Ec number. The negative bottom velocity and positive centroid velocity show that the bubble becomes prolate right after its release. There is a transition from negative

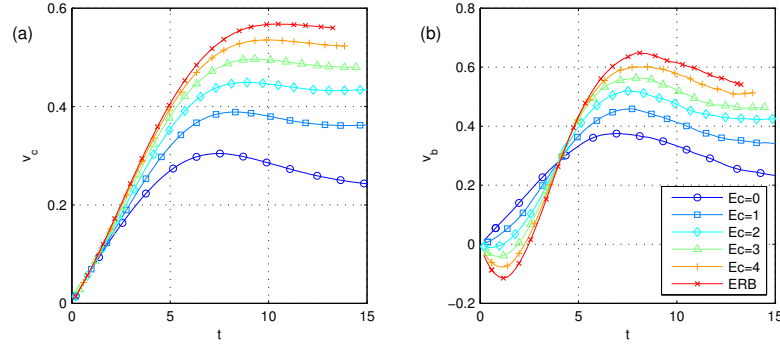


FIGURE 5.17: Temporal variations of centroid velocity v_c at left and bottom velocity v_b at right for different electrical capillary numbers Ec .

to positive value of bottom velocity which occurs earlier in time for smaller values of electrical capillary numbers. After this transition, the bottom velocities cross each other at $t \approx 4.2$ in $v_b \approx 0.3$ which coincides with the moment at which the bubbles reach their highest aspect ratio, as can be seen from figure 5.16.

5.2.1.3 Effect of Reynolds number

In order to observe the effect of Reynolds number on the bubble rising, four cases are studied here, ranging from $Re = 100$ to $Re = 400$ with constant increments of 100, while other dimensionless numbers are set to $Bo = 12$ and $Ec = 5$.

Figure 5.18 gives the variation of aspect ratio versus time for four test cases studied here. Having the highest Reynolds number, the *ERB* case yields a faster response to the electric forces due to the smaller viscous force and hence elongates more, leading to the larger difference between the maximum and terminal aspect ratios. One can additionally note that $Re = 100$ has the lowest variation of the aspect ratio compared to the others, due to stronger viscous force. Moreover, there is not a significant difference in terminal aspect ratio among these four cases.

Figure 5.19 shows the variations of bubble centroid and bottom velocities in time for variations of Reynolds number. Considering the relative significance of viscous force compared to inertial force, the smaller the Reynolds number, the later the bubble reaches its terminal velocity. The terminal velocity increases with incrementing Reynolds number, but it appears that further increment of Reynolds number does not lead to a significant increase in terminal velocity. As for the bottom velocity, all test cases have initial negative velocity which increases with the increment of Reynolds number. The cross-over of velocities occurs in smaller magnitudes of velocity in earlier time compared to that discussed in figure 5.17.

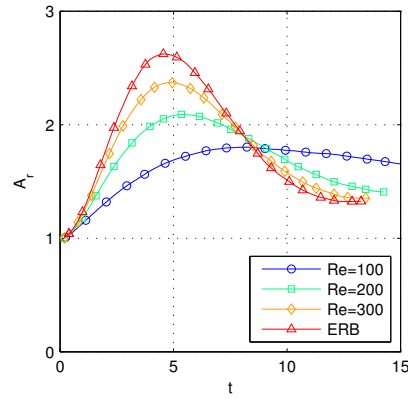


FIGURE 5.18: Temporal variation of aspect ratio A_r for four different Reynolds numbers.

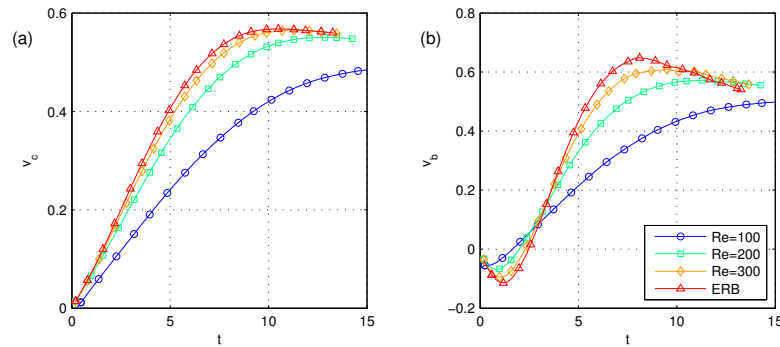


FIGURE 5.19: Temporal variations of centroid velocities v_c at left and bottom velocity v_b at right for four different Reynolds numbers.

5.2.1.4 Effect of Bond number

In this section, the influence of Bond number on the evolution of the bubble under electric field is studied to investigate the significance of interfacial tension forces by addressing the possible role of surfactants on the bubble rising. Here, six different cases are studied and the Bond number is changed from $Bo = 2$ to $Bo = 12$ with constant increments of 2, while other dimensionless numbers are set to $Re = 400$ and $Ec = 5$.

Figure 5.20 shows the variation of aspect ratio versus time for six different cases. One may intuitively expect that the higher the Bond number, the bubble should become more prolate since smaller surface tension force (opposing to electric force) acts on the bubble interface. However, it is observed that the aspect ratio decreases as the Bond number increases. The reduction in the Bond number will correlate with the increase in the surface tension. To maintain constant Ec , electric force needs to be augmented, increasing the prolateness of the bubble.

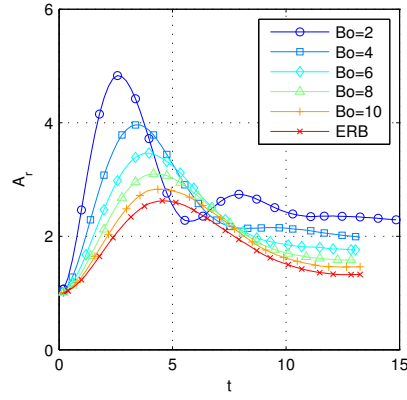


FIGURE 5.20: Temporal variations of aspect ratio A_r , for six different Bond numbers.

The temporal evolution of the centroid and bottom velocities of the bubble for variations of Bond number is presented in figure 5.21. For all the cases except for $Bo = 2$, the centroid velocities increase monotonically in time. The initial notable decrease in the centroid velocity of $Bo = 2$ is owing to the electrical interaction between the bubble and bottom boundary. It is observed here that the bottom boundary pulls the bubble towards itself due to the asymmetric electric force balance at the interface right after the bubble is released. As the Bond number decreases, the pulling effect of the bottom boundary becomes more prevalent. In order to elaborate on the pulling effect, a dimensionless velocity scale U^* is introduced as the ratio of the dielectrophoretic velocity [82] to the gravitational velocity,

$$U^* = \frac{u_d}{u_g} = \frac{\epsilon_f E_\infty^2 r / \mu_f}{\sqrt{2gr}} = \frac{\epsilon_f E_\infty^2}{2\mu_f} \sqrt{\frac{2r}{g}}. \quad (5.6)$$

The dielectrophoretic velocity increases with the enhancement of electric field strength, resulting in an increase in the dimensionless velocity scale, U^* and consequently the pulling effect. It is observable that the centroid velocity of the rising bubble is initially larger for higher Bond number due to the smaller velocity scale. At around $t \approx 10$, there is a cross-over of centroid velocity where the order of the centroid velocity plots for different Bond numbers changes. When the bubble is sufficiently away from the boundary, the pulling effect of the boundary vanishes. Thus, the bubble with a higher aspect ratio (corresponding to lower Bond number cases) will naturally rise faster due to the reduced hydrodynamic drag on the bubble. The variation of bottom velocity as a function of Bond number in figure 5.21-b has a similar behavior with respect to the centroid velocity. The cross-over

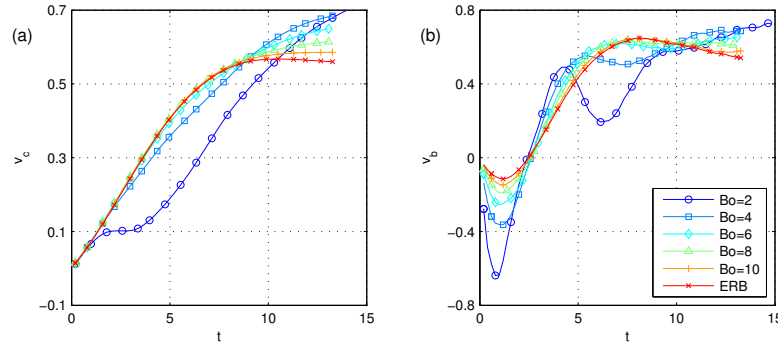


FIGURE 5.21: Temporal variations of centroid velocities v_c at left and bottom velocity v_b at right for six different Bond numbers.

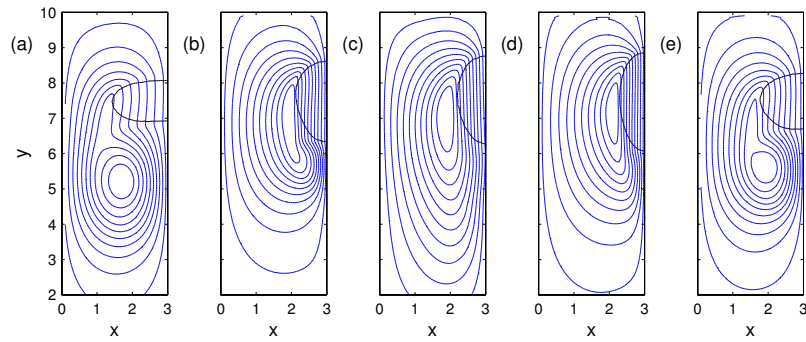


FIGURE 5.22: Bubble shape and velocity streamlines at $y = 7.5$ for five various cases; (a) $Ec = 1$, (b) ERB , (c) $Re = 100$, (d) $Bo = 4$, and (e) $Ec = 1$.

of the bottom velocities occurs earlier in time compared to variations of Reynolds and electrical capillary numbers. This cross-over happens at $t \approx 3$ where the magnitude of the bottom velocity is almost zero.

Figure 5.22 represents concisely the influence of three different dimensionless numbers on bubble rising by showing bubble shape and corresponding streamlines for five different cases in the half of the computational domain. The bubbles are shown for the moment that their centroids are at $y = 7.5$. The presented cases in figure 5.22 are selected as: (a) the case $Ec = 0$ which has no electric forces acting on the bubble, (b) is the case ERB while cases in (c), (d) and (e) are for $Re = 100$, $Bo = 4$ and $Ec = 1$, respectively. According to the parameter setup of Reynolds and Bond numbers, the oblate shape of the bubble in the absence of electric field (Figure 5.22-a) is due to the formation of a jet current beneath the bubble and hydrodynamic drag force. In the absence of electric forces, the vortex detaches from the bubble and remains in the bubble wake, but the exertion of electric forces keeps the vortex alongside the bubble as discussed in figure 5.15. The variation of Reynolds number does not change the bubble shape considerably. The reason is

TABLE 5.6: The dimensionless parameters and their corresponding magnitudes, which have been used to investigate the interaction of bubbles for different orientations and initial center to center distances.

Case	P01	P02	P03	P04	P11	P12
l^*	2.5	3	3.5	4	2.5	3
θ	0	0	0	0	$\pi/4$	$\pi/4$

that electric forces relatively dominate the physics, and decreasing the Reynolds number or in other words enhancing viscous forces does not play a significant role in terminal bubble shape. Raising the surface tension force increases the bubble aspect ratio, enabling the bubble to rise faster. Reduction in Bond number corresponds to an increase in electric force for constant Ec thereby giving rise to further prolateness of the bubble. The case $Ec = 1$ is the intermediate case between cases $Ec = 0$ and ERB where the electric forces are applied but they are not sufficiently strong to elongate the bubble prolately.

5.2.1.5 The EHD interaction between a pair of rising bubble

In this section, the interaction between a pair of rising bubbles is studied for six cases with simulation conditions similar to ERB , under two different initial geometrical orientations. The initial placement of bubbles with respect to each other is controlled by two parameters, namely; the initial center to center distance between the pair of bubbles, l^* , and the angle, θ , between the y axis and the imaginary line connecting the centers of the bubbles. Here, two different angles of $\theta = 0$ and $\theta = \pi/4$ are simulated for various initial center to center distances. Table 5.6 lists the parameters for the cases of this section. For all the cases, the bubbles have the same size, and the distance between the center of the lower bubble and the bottom boundary is one bubble diameter.

Figure 5.23 presents the results for the initial orientation of $\theta = 0$. The left sub-figure shows the distance between bubbles' centroids during their rising motion for all cases with $\theta = 0$ versus the centroid position of the upper bubble. The solid lines illustrate the moment where the bubbles are not merged while the dashed lines represent the merged instances. Here, the bubbles are assumed to merge when the distance between their interfaces is less than three particle spacings. After this point, which happens only for cases P01 and P02, the bubbles ascend in close proximity without forming a unified bubble. Unifying the smaller bubbles into a single larger bubble requires specific algorithms that are beyond the scope of this study. For all vertically in-line bubbles, the general interaction between

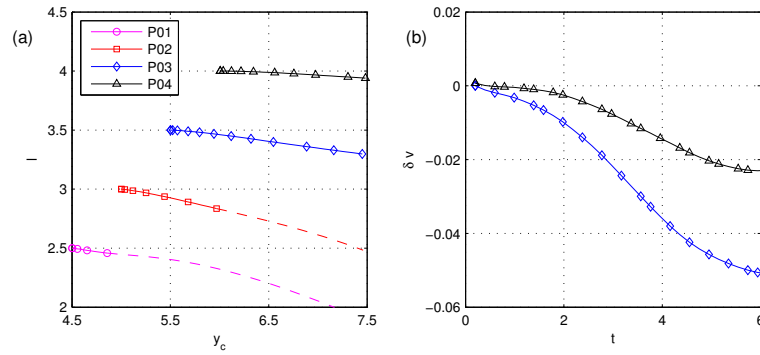


FIGURE 5.23: The interaction of two bubbles with $\theta = 0$ (vertically in-line) for four cases of $P01$, $P02$, $P03$, and $P04$; The left sub-figure shows the distance between bubble centroids for these cases versus the centroid position of the upper bubble; the solid lines indicate the moments in which the bubbles are not merged and dash lines show the merged instances. The right sub-figure shows the difference between upper to lower centroid velocities during evolution time for two cases of $P03$ and $P04$.

bubbles is observed to be attractive. For $P01$ case, the bubbles collide just after their release, due to the initial prolate elongation of bubbles. For $P02$ case, the bubbles merge due to: (i) the prolate elongation due to the electric field and (ii) the pressure drop generated at the wake of the upper bubble. The larger the initial center to center distances are, the merging occurs later in time. For the cases $P03$ and $P04$, the bubbles do not merge but the distance between centroids of two bubbles decreases due to the same reasons explained above. The right sub-figure shows the difference between the bubble centroid velocities versus time calculated as $\delta v = v_b^u - v_b^b$ during their rise where the superscripts u and b denote the upper and bottom bubbles, respectively. This velocity difference shows the effect of the generated pressure drop at the wake of the upper bubble on the distance between the bubbles' centroids.

Figure 5.24 represents the bubble deformation for two cases with $\theta = \pi/4$ orientation throughout their rising. The left figure shows the bubbles shapes for $P11$ and the right figure presents those of $P12$ for three instances $t = 0$, $t = 4$ and $t = 8$. The results show that the bubbles are initially deformed due to electric forces. The bottom bubble rises much slower compared to the upper bubble. The rise of the bottom bubble is hindered due to the fact that the bubble is attracted to the bottom boundary. The effect is much smaller for the upper bubble which is further away from the bottom boundary. Due to the initially oblique orientation of the bubbles, the wake of the upper bubble is less effective in drawing the bottom bubble when compared to the aligned configurations $P01$ - $P04$. Figure 5.25 shows the distance between the centroids of bubbles at left and their corresponding angle at

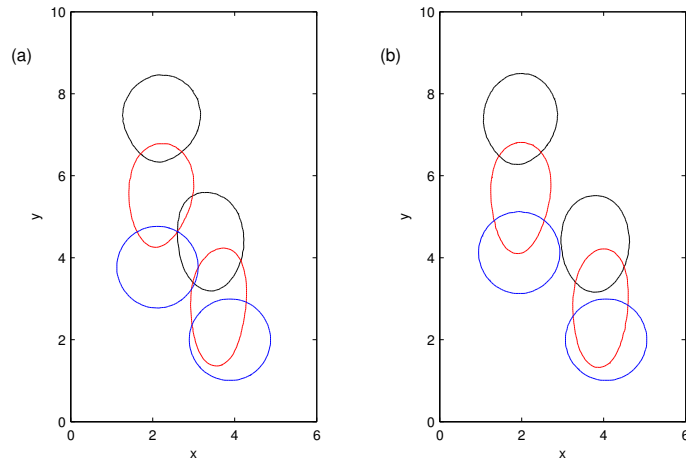


FIGURE 5.24: The interaction of two bubbles with $\theta = \pi/4$; The bubble interface is shown for three different instants of the rising motion, namely, $t = 0$, $t = 4$ and $t = 8$, for $P11$ at the left and for $P12$ at the right.

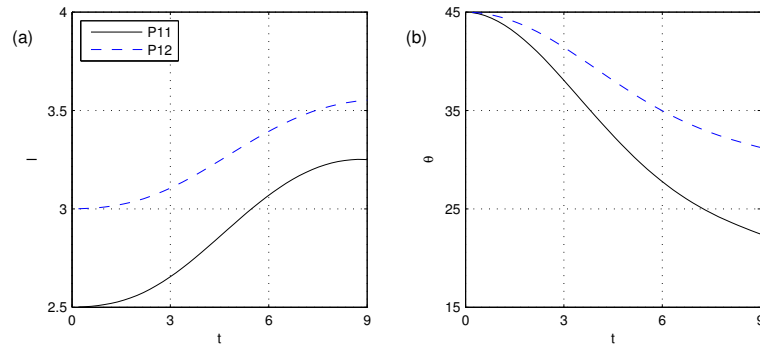


FIGURE 5.25: The center to center distance of bubbles (left) and corresponding angle (θ) (right) for two cases of $P11$ and $P12$.

right for two cases of $P11$ and $P12$. Unlike cases $P01$ - $P04$, the distance between the centroids of the bubbles increases during their rise (figure 5.25-a). Figure 5.25-b indicates that the angle between the bubble centroids decreases since the wake of the upper bubble pulls the lower bubble in the transverse direction of the domain. As the angle between the bubbles decreases, the bottom bubble feels the wake of the upper bubble more and the attractive interaction between the bubbles gets stronger. This can be confirmed from decreasing slope of centroid to centroid distance of bubbles in figure 5.25-a. This may result in a pair of bubbles rising vertically in-line for long rises.

5.2.2 Bubble rising of an air-water system

Considering the governing equations explained in chapter 2, dimensionless values are formed using the following scales

$$\begin{aligned} \mathbf{r} &= \mathbf{r}^+/\mathbf{d}, & \mathbf{z} &= \mathbf{z}^+/\mathbf{d}, & \rho &= \rho^+/\rho_f, & \mu &= \mu^+/\mu_f, & \mathbf{u} &= \mathbf{u}^+/\sqrt{g\mathbf{d}}, \\ t &= t^+\sqrt{g/\mathbf{d}}, & \mathbf{E} &= \mathbf{E}^+/E_\infty, & p &= (p^+ - \rho\mathbf{g} \cdot \mathbf{x}^+)/\rho_f g\mathbf{d}, \\ \mathcal{D} &= \rho_b/\rho_f, & \mathcal{V} &= \mu_b/\mu_f, & \mathcal{P} &= \varepsilon_b/\varepsilon_f, & \mathcal{C} &= \sigma_b/\sigma_f, \end{aligned} \quad (5.7)$$

leading to Reynolds, Bond, Electro-gravitational and Electro-capillary numbers defined as

$$\text{Re} = \frac{\rho_f \sqrt{g\mathbf{d}^3}}{\mu_f}, \quad \text{Bo} = \frac{\rho_f g\mathbf{d}^2}{\gamma}, \quad \text{Eg} = \frac{\rho_f g\mathbf{d}}{\varepsilon_f E_\infty^2}, \quad \text{Ec} = \frac{\text{Bo}}{\text{Eg}} = \frac{\varepsilon_f E_\infty^2 \mathbf{d}}{\gamma}. \quad (5.8)$$

Here \mathbf{d} is the bubble diameter, E_∞ is the undisturbed electric field intensity and g is the gravitational acceleration. A plus sign marks dimensional variables whereas subscripts \square_b and \square_f denote bubble and surrounding fluid phases, respectively.

5.2.2.1 Problem set-up

Here, the axisymmetric simulation domain is a rectangle with a height of H and width of W wherein the bubble is centered at a distance of $h_d = 4(\mathbf{d}/2)$ from the bottom boundary, as shown schematically in figure 5.26. The domain height is set to $H = 24(\mathbf{d}/2)$ which is tested in the preliminary studies ensuring the system to be independent from vertical boundary confinement. The width of the domain is adjusted accordingly to maintain the desired confinement ratio. No-slip condition along with a potential difference of $E_\infty = \Delta\phi/H$ is applied to top and bottom walls shown by solid lines in figure 5.26. Referring to figure 5.26, the left and right boundaries are shown with dash-dot and dash lines representing the domain axis and the side wall, respectively. The right boundary abides the no-slip boundary condition and a Neumann boundary condition for the electric potential. In the absence of the bubble, this produces a uniform downward electric field parallel to the side walls. In all simulations including the validation and convergence tests, the time step is set to keep the Courant-Friedrichs-Lewy (CFL) condition below 0.2 ($\text{CFL} < 0.2$).

To validate the results of present study, three test cases (VT1, VT2 and VT3) are simulated and compared with those from experiments of Bhaga *et al.* [111]

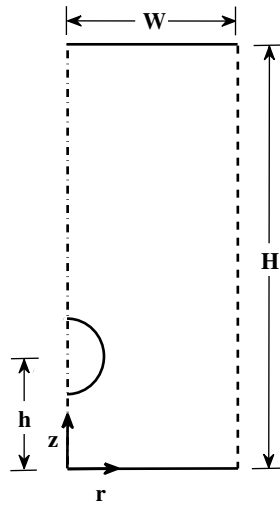


FIGURE 5.26: Schematic of the test case.

and numerical findings of Hua *et al.* [65]. In order to ensure that the results are not affected by the side wall effects, the diameter and height of the axisymmetric domain is taken six and twelve times larger than the bubble diameter ($W = 6(d/2)$) and ($H = 24(d/2)$), respectively. The bubble is located at a distance of two bubble diameters from the bottom boundary, and the boundary conditions are similar to those indicated in figure 5.26. The simulation condition of the test case VT1 is $[\text{Re} = 33.02, \text{Bo} = 116]$, while VT2 and VT3 cases have simulation conditions of $[\text{Re} = 135.4, \text{Bo} = 116]$, and $[\text{Re} = 15.24, \text{Bo} = 243]$, respectively, and the density and viscosity ratios are $\mathcal{D} = 1000, \mathcal{V} = 100$. These conditions are identical to those of Hua *et al.* [65] and equivalent with results of Bhaga *et al.* [111]. It should be noted that in [111] the Reynolds number is calculated based on the terminal rise velocity (U_t) of the bubble and named as the terminal Reynolds number $\text{Re}^* = \rho_f U_t d / \mu_f$. Table 5.2 compares terminal bubble shapes and vertical rise velocity of VT1, VT2 and VT3 with experiments in [111] and simulations in [65]. Considering terminal bubble shapes, the present numerical results are satisfactory in general, and matches with results of the provided references. The comparison of terminal rise velocity with numerical simulations in [65] shows that the present numerical results underestimates the vertical rise velocity for VT2 and VT3 by the relative difference of 0.9% and 1.6%, respectively, and overestimates the rise velocity of VT1 by the relative difference of 1.8%.

There is a difference observed between the characterized Reynolds number (Re) of numerical simulations and calculated Reynolds number (Re^*) of experimental studies. Based on the dimensionless and characteristic parameters, the terminal

TABLE 5.7: Validation of Numerical code with the experiments of Bhaga *et al.* [111] and Hua *et al.* [65] for three test cases; VT1: $Re = 33.02$ and $Bo = 116$, VT2: $Re = 135.4$ and $Bo = 116$, and VT3: $Re = 15.24$ and $Bo = 243$.

Test case	Experiment conditions	Bhaga [111]	Simulation conditions	Hua [65]	Simulation conditions	Present study
VT1	$Re^* = 20.4$		$Re = 33.02$		$Re = 33.02$	
	$Bo = 116$		$Bo = 116$		$Bo = 116$	
	$U_t = \text{—}$		$U_t = 0.602$		$U_t = 0.613$	
VT2	$Re^* = 94$		$Re = 135.4$		$Re = 135.4$	
	$Bo = 116$		$Bo = 116$		$Bo = 116$	
	$U_t = \text{—}$		$U_t = 0.660$		$U_t = 0.654$	
VT3	$Re^* = 7.77$		$Re = 15.24$		$Re = 15.24$	
	$Bo = 243$		$Bo = 243$		$Bo = 243$	
	$U_t = \text{—}$		$U_t = 0.551$		$U_t = 0.542$	

rise velocity of the bubble can be found by $U_t \cdot \sqrt{gd}$, and the Reynolds number calculated based on the dimensional terminal rise velocity can be obtained by $Re_c^* = U_t \cdot Re$. For the above simulated cases, the calculated Reynolds number is found to be $Re_c^* = 20.24$, $Re_c^* = 88.55$ and $Re_c^* = 8.26$ for cases VT1, VT2, and VT3 which shows relative difference ($\frac{|Re^* - Re_c^*|}{Re^*} \times 100$) compared to the experimental finding of Bhaga *et al.* [111] by 0.78, 5.8, and 6.3 percentages, respectively. It should be noted that similar comparison has been made by Hua *et al.* [65] reporting comparable results.

Figure 5.27 presents the dependency of present numerical results on the grid the resolution for the test case VT3 from table 5.7. For all simulations in this paper, the domain is meshed by Cartesian structured mesh model. The test is carried out for four different resolution cases of $MR1 = 24\chi_p$, $MR2 = 32\chi_p$, $MR3 = 48\chi_p$, and $MR4 = 64\chi_p$, where $n\chi_p$ indicates the number of grids per initial bubble diameter. It is observed that for the coarse case of MR1, the bubble vertical velocity is under predicted and the bubble shape has considerable distinctions compared to other cases. The comparison of MR3 and MR4 reveals that the increase in the grid resolution does not change the results considerably, thus the resolution of MR3 is adopted for the simulations of the present study. It should be mentioned that the validation of present study in table 5.7 are also carried out with the same mesh resolution (MR3).

Here, the results of a rising bubble in a cylindrical confined domain under the effect of an external electric field are presented. The domain confinement ratio Cr is defined as the ratio of the diameter of the cylindrical domain over the bubble

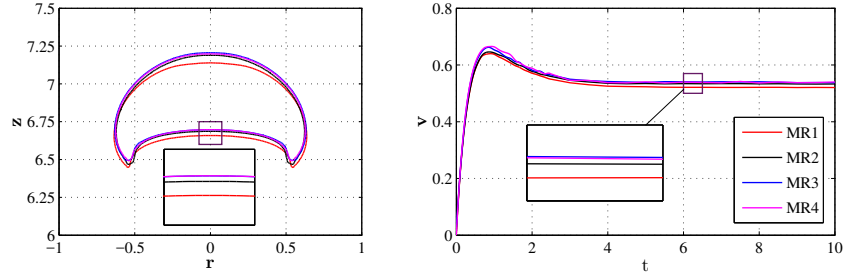


FIGURE 5.27: The grid resolution study for the test case VT3 from table 5.7 for bubble shape (at left) and vertical rise velocity (at right), employing four different resolutions of $MR1 = 24\chi_p$, $MR2 = 32\chi_p$, $MR3 = 48\chi_p$, and $MR4 = 64\chi_p$ where $n\chi_p$ indicates the number of grids per initial bubble diameter.

diameter, $Cr = (2W/d)$. In our preliminary investigations, it is observed that the side wall boundary effects are insignificant for confinement ratios above five ($Cr > 5$). Thus, four confinement ratios of $Cr = 2$, $Cr = 3$, $Cr = 4$, and $Cr = 5$ are considered to take into account the effect of confinement ratio. The simulation conditions of the rising bubble is $Re = 100$, $Bo = 50$, $\mathcal{D} = 0.001$, $\mathcal{V} = 0.01$, $\mathcal{C} = 0.001$, and $\mathcal{P} = 0.05$. Under such simulation conditions and in the absence of electric forces, the bubble deforms to a hemispherical shape in small confinement ratios ($Cr = 2$) due to the effects of the side domain boundaries. By increasing the confinement ratio, the bubble is flattened where the effects of the side domain boundary are lessened. Despite having a wider frontal area, the bubble rises faster in larger confinement ratios. This is a direct consequence of the effects of domain confinement on hydrodynamics of the bubble rising such as the flow vortices inside and outside of the bubble. It should be noted that similar results have been reported in [112] for equivalent simulation conditions.

It should be noted that the Bond number can also be represented as the ratio of the characteristic length (here the bubble diameter) over the capillary length scale ($L_c = \sqrt{\frac{\gamma}{\rho_f g}}$). In the present study, the characteristic length scale is almost one order of magnitude larger than the capillary length scale. This leads to the consideration of just geometrical confinement due to the domain constraints.

In the presence of electric field, the electric potential is adjusted to maintain the Electro-capillary number in the range of $0.5 \leq Ec \leq 2.5$. For small Electro-capillary numbers, $Ec \approx 0.5$, the electric forces do not significantly influence the bubble shape and its vertical rise velocity in any confinement ratio. On the other hand, applying the Electro-capillary number of $Ec = 2.5$ leads to the formation of a toroidal bubble shape for all confinement ratios. In the following, the formation of a toroidal rising bubble is separately investigated for the piercing effect of electric

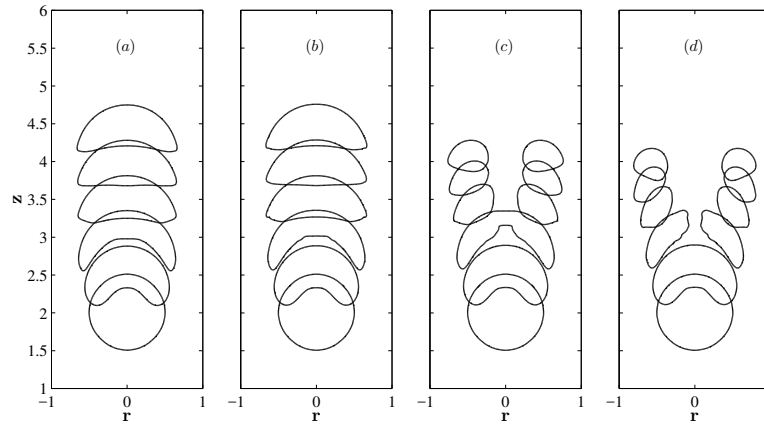


FIGURE 5.28: The history of bubble shapes at $t = 0, 1, 2, 3, 4, 5$ in confinement ratio of $Cr = 2$ for variations of Electro-capillary number; (a) $Ec = 1.0$, (b) $Ec = 1.5$, (c) $Ec = 2.0$, (d) $Ec = 2.5$.

forces in a confined domain, and the influence of confinement ratio in the presence of electric forces. Afterwards, relevant discussions are made on the combined effect of electric forces and confinement ratios on the formation of a toroidal bubble.

5.2.2.2 Effect of Electro-capillary number

Figure 5.28 represents the cross-section and the history of bubble shapes at $t = 0, 1, 2, 3, 4, 5$ for the confinement ratio of $Cr = 2$ and for four different Electro-capillary numbers, (a) $Ec = 1.0$, (b) $Ec = 1.5$, (c) $Ec = 2.0$ and (d) $Ec = 2.5$. During the initial transient stage wherein the bubble motion is dominated by inertial force, the bubble deforms from an initial spherical shape to a spherical-cap shape ($t = 2$ in (a) and (b) cases). Here, recall that the initial transient stage refers to dynamics of the bubble from the initial spherical shape to the terminal state of non-pierced cases and to the piercing moment of pierced cases. This deformation is followed by the formation of an upward jet current of the surrounding fluid at the wake of the bubble. Consequently, the bottom surface of the bubble is indented inwardly while the upper surface of the bubble remains nearly spherical. Afterwards, the bubble tries to maintain its terminal shape due to the effect of surface tension where the indentation of the bottom surface is vanished and the bottom surface of the bubble flattens, reaching into a hemispherical state. Increasing the Electro-capillary number in (c) and (d) cases, the bubble is pierced and a toroidal bubble is formed. The piercing occurs when the upward jet current pushes the bottom surface and the distance between the upper and bottom surfaces of the bubble is minimum in the transient stage (notice $t = 2$ in case

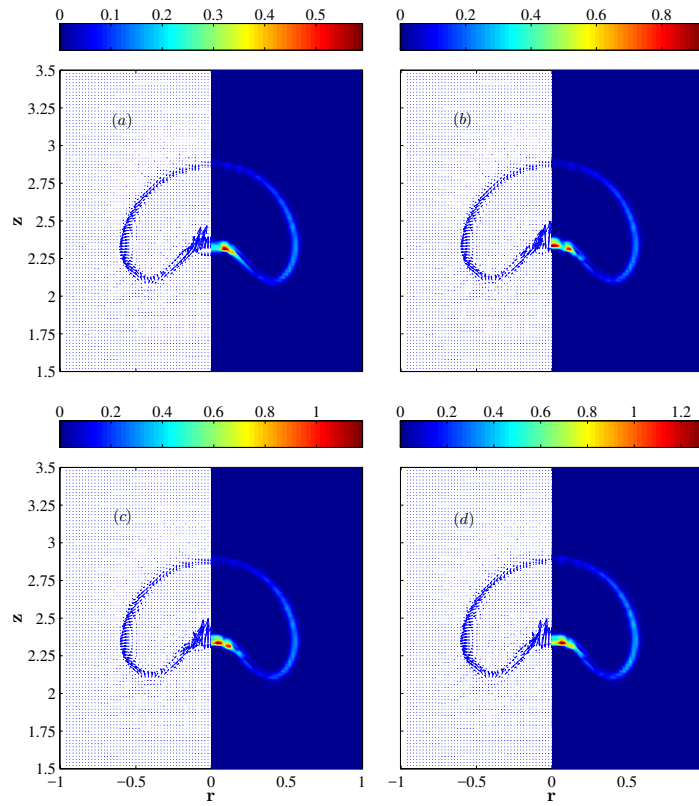


FIGURE 5.29: The electric forces per unit volume normalized by $\varepsilon_f E_\infty^2/d$ shown by vector field (on the left half) and contours (on the right half) on the interface of the bubble at $t = 1$ in confinement ratio of $Cr = 2$ and for (a) $Ec = 1.0$, (b) $Ec = 1.5$, (c) $Ec = 2.0$, (d) $Ec = 2.5$; In order to compare force magnitudes, the electric field intensity for normalizing the forces E_n is taken equal to 1.

(c)). At this moment, the electric forces which act on the interface directing into the bubble, facilitate the formation of a toroidal bubble if the magnitude of the Electro-capillary number is sufficiently large. By comparing the bubble shapes at $t = 2$ for (c) and (d) cases in figure 5.28, it is observed that the electric forces pierce the bubble earlier in time in case (d) which has a larger magnitude of the Electro-capillary number. After the bubble is pierced, the surface tension force which is stronger in regions where the curvature is larger, preserves the shape of the bubble ring (notice the deformation of the bubble shape from $t = 2$ to $t = 5$ for case (d)). This can be referred to as the 'secondary transient stage' describing the dynamics of a rising bubble between the piercing moment and reaching its terminal state. Later, it will be discussed how domain confinement affects the secondary transient stage.

In order to see how the electric forces assist the formation of a toroidal bubble,

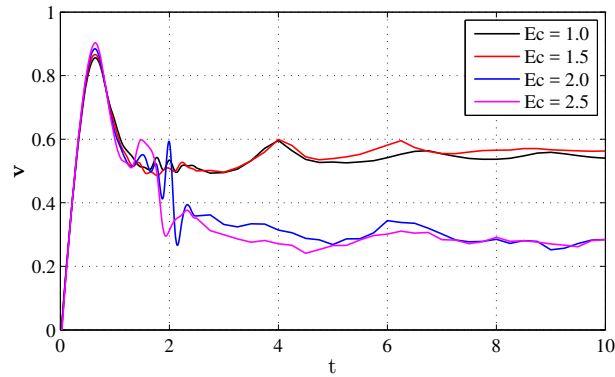


FIGURE 5.30: The vertical rise velocity versus time for constant confinement ratio $Cr = 2$ at different Electro-capillary ratios, $Ec = 1.0, 1.5, 2.0$ and 2.5 .

figure 5.29 is presented. In this figure, the normalized electric forces per unit volume are shown at $t = 1$ on the bubble interface for four cases represented in figure 5.28. It is seen that the electric forces increase with increments of Electro-capillary number by comparing the normalized magnitudes of the forces. Considering the distribution of electric forces on the bubble interface, it is observed that the electric forces are stronger on the bottom surface of the bubble. Moreover, the force vectors show that the direction of electric forces are from the heavier fluid towards the lighter one in that region. This shows that when the distance between the upper and bottom surfaces of the bubble are small, the electric forces pierce the bubble from the center.

The vertical rise velocities of cases (a), (b), (c) and (d) from figure 5.28 are presented in figure 5.30. For the initial moments of transient stage nearly up to $t \approx 1$, the vertical rise velocity increases and reaches a maximum, and thereafter decreases due to the distended frontal area which augments the drag force and nearly levels off with relatively small oscillations for non-pierced cases and drops down further for pierced cases. The maximum value of rise velocity gets larger with increments of the Electro-capillary number. This is due to the distribution and direction of electric forces on the bubble interface, as described in figure 5.29. Since the electric forces are stronger on the bottom surface of the bubble during the initial transient stage directing from heavier to lighter fluid, slight increase on the vertical rise velocity is observed for increments of Electro-capillary number. At $t \approx 2$, piercing occurs for $Ec = 2.0$ and $Ec = 2.5$ cases and the upward jet current passes through the pierced area (not shown here), followed by a sudden drop in the vertical rise velocity. As a result, the terminal rise velocity of the pierced bubbles decreases by almost 50 percent compared to the non-pierced cases. During the secondary transient stage for the pierced cases, the vertical rise velocity decreases

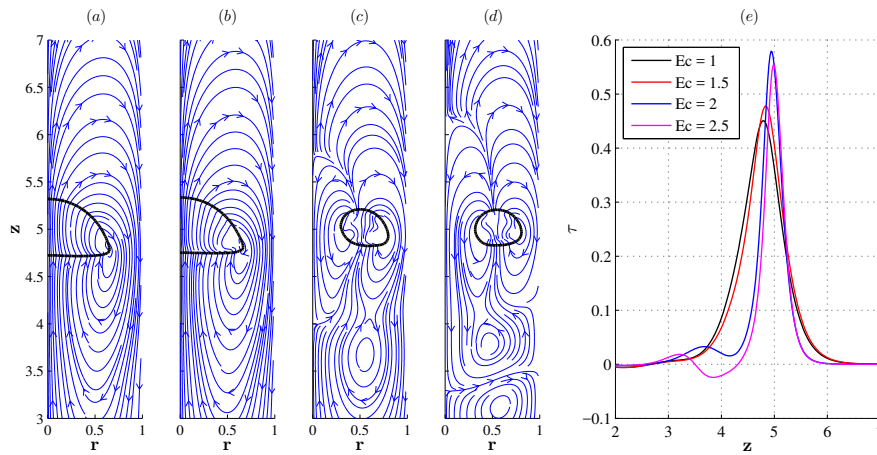


FIGURE 5.31: The velocity streamlines and bubble shapes for confinement ratio for $Cr = 2$ and different Electro-capillary numbers; (a) $Ec = 1.0$, (b) $Ec = 1.5$, (c) $Ec = 2.0$, (d) $Ec = 2.5$ and (e) their corresponding wall shear stress; The bubbles are shown in a half domain for the moment when their centroids are at $z = 5$.

slightly from $v \approx 0.4$ to $v \approx 0.3$. This slight decrease is due to the effects of side boundary, and occurs when the bubble ring approaches the side boundaries during its secondary transient stage. For all cases, it is observed that the velocities are oscillatory especially for pierced cases. It will be shown that these oscillations are due to the confinement of the domain and disappear when the confinement ratio is increased.

Figure 5.31 represents the velocity streamlines and bubble shapes in the half domain for confinement ratio of $Cr = 2$ and for different Electro-capillary numbers (figures 5.31 (a)-(d)), and their corresponding wall shear stress $\tau_w = \mu_f \nabla \mathbf{u}|_z$ at the side wall boundary normalized by $\rho_f g d$ (figure 5.31 (e)). The cases are shown for the moment when the centroid of the bubble is at $z = 5$. For (a) and (b) cases, the bubble is not pierced, and the velocity streamlines illustrate the structure of the upward jet current at the wake of the bubble. For the pierced cases in (c) and (d), however, no upward jet current of surrounding fluid which passes into the pierced region is observed. It should be noted that after the formation of the toroidal shape, a pair of vortices begin to develop at the sides of the bubble ring. These vortices develop as the bubble rises in the fluid. Simultaneously, the effect of the upward jet current in the pierced region gradually disappears. Consequently, the direction of the surrounding fluid motion in the pierced region is reverted. Such a transformation leads to the formation of some other complex vortices especially beneath the bubble ring. Considering the wall shear stress in figure 5.31 (e), it should be noted that positive magnitudes of wall shear stress indicate the

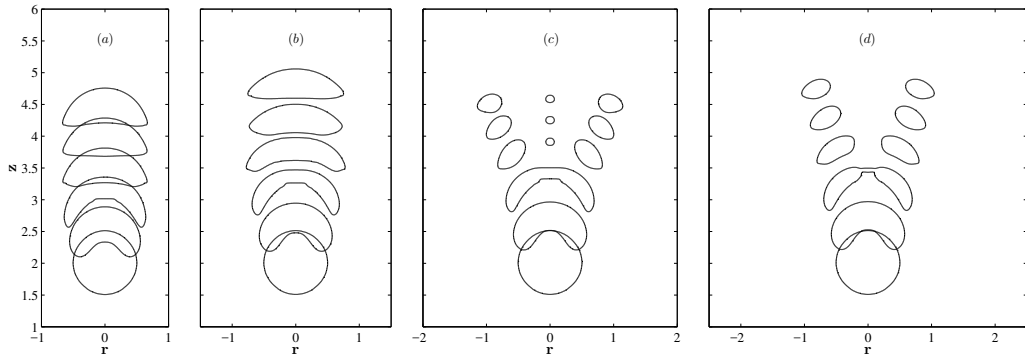


FIGURE 5.32: The history of bubble shapes at $t = 0, 1, 2, 3, 4, 5$ in Electro-capillary number of $Ec = 1.35$ for various confinement ratios; (a) $Cr = 2$, (b) $Cr = 3$, (c) $Cr = 4$, (d) $Cr = 5$.

friction in the upward direction for downward motion of the surrounding fluid at the vicinity of the wall. The maximum value of the wall shear stress slightly increases with increments of Electro-capillary number for non-pierced cases. The location of the maximum value stands at the elevation of the bottom surface of the hemispherical bubble. For the pierced cases, the magnitude of the maximum point increases considerably and its location is at the elevation of the centroid of the bubble ring. Increments of Electro-capillary number for pierced bubbles show a slight decrease in the maximum value of the wall shear stress. For $Ec = 2.5$, the wall shear stress has negative values between $z \approx 3.5$ and $z \approx 4.3$ indicating that an upward current of the surrounding fluid exists in the vicinity of the wall as a direct consequence of the formation of vortices beneath the toroidal bubble.

5.2.2.3 Effect of confinement ratio

The cross-section and the history of bubble shapes at $t = 0, 1, 2, 3, 4, 5$ for Electro-capillary $Ec = 1.35$ and various confinement ratios, (a) $Cr = 2$, (b) $Cr = 3$, (c) $Cr = 4$, (d) $Cr = 5$ are shown in figure 5.32. Later it will be shown that how the confinement ratio affects the minimum value of the Electro-capillary number required for piercing the bubble. It will also be shown that in large confinement ratios, there is not much of a difference between the minimum value of Electro-capillary number which can pierce the bubble. Thus, $Ec = 1.35$ is selected to show that the bubble pierces in two larger confinement ratios but remains hemispherical/ellipsoidal in more confined cases. Comparing the bubble terminal shapes for (a) and (b) cases at $t = 5$, it is observed that the bubble is more flattened when the confinement ratio increases, changing the terminal shape from a hemispherical shape in $Cr = 2$ to an ellipsoidal-cap in $Cr = 3$. When the bubble is flattened

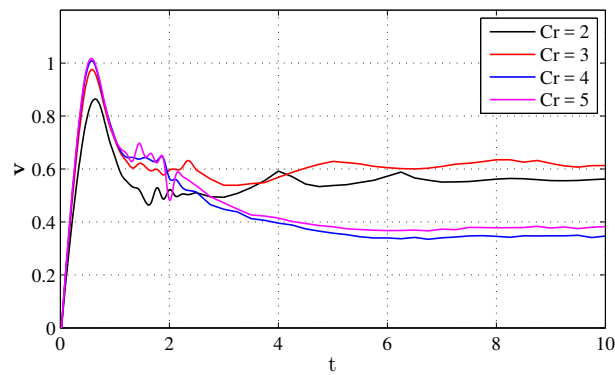


FIGURE 5.33: The vertical rise velocity versus time for constant Electro-capillary numbers $Ec = 1.35$ at different confinement ratios, $Cr = 2, 3, 4$ and 5 .

in larger confinement ratios, the distance between the upper and bottom surface of the bubble in the transient region decreases (notice the bubble shapes at time $t = 2$ and consider the distance between upper and bottom surfaces in $r = 0.0$). Then, the electric forces pierce the bubble from the center forming a toroidal bubble as discussed in figure 5.28. After the formation of the toroidal bubble, the secondary transient stage begins.

Figure 5.33 represents the vertical rise velocity versus time for the cases shown in figure 5.32. The maximum value of vertical rise velocity increases with increments of the confinement ratio. This is intuitively expected since the larger the confinement ratio, the less the effect of the no-slip boundary on the rising velocity. Similar to the variations of maximum of vertical rise velocity for different Electro-capillary numbers (figure 5.30), the vertical rise velocity drops down (after $t \approx 1$) due to the enlargement of the frontal area of the bubble and levels off briefly. For (c) and (d) cases, the vertical rise velocity sharply drops down further because of the piercing of bubbles. Further decrease in the vertical rise velocity until $t \approx 5$ for (c) and (d) cases indicates the secondary transient stage of the bubble. After reaching the terminal rise velocity, one can clearly observe the influence of the increments of confinement ratio on the magnitude of the terminal rise velocity for both pierced and non-pierced cases where upon the formation of toroidal bubble, the terminal rise velocity of pierced bubbles falls below those of (a) and (b) cases. It is shown earlier that the vertical rise velocity in small confinement ratios are oscillatory. Here in figure 5.33, it is shown that by increasing the confinement ratio, these oscillations tend to be reduced.

Figure 5.34 represents the velocity streamlines and cross section of bubble rings in

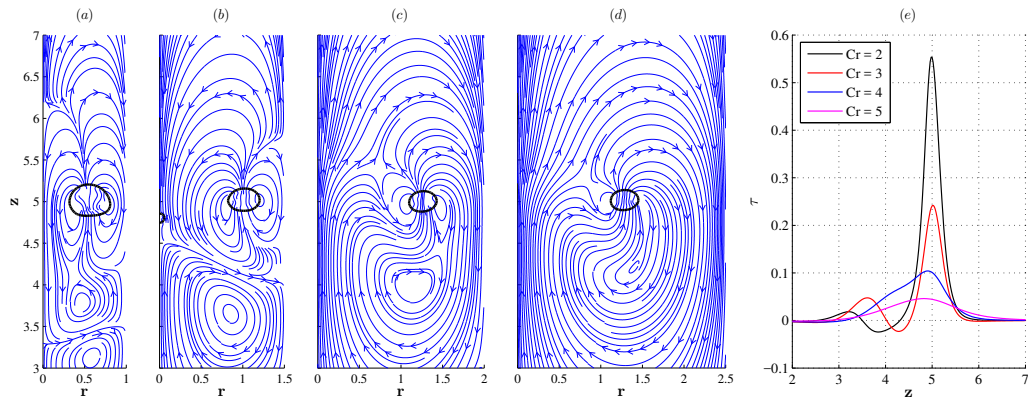


FIGURE 5.34: The velocity streamlines and bubble shapes for Electro-capillary number of $Ec = 2.5$ and different confinement ratios; (a) $Cr = 2$, (b) $Cr = 3$, (c) $Cr = 4$, (d) $Cr = 5$ and (e) their corresponding wall shear stress; The bubbles are shown in a half domain for the moment when their centroids are at $z = 5$.

the half domain for Electro-capillary number of $Ec = 2.5$ and various confinement ratios (figure 5.34 (a) - (d)), and the corresponding side wall shear stress (figure 5.34 (e)), at the moment when the centroid of the bubble ring is at $z = 5$. In relation to the formation of vortices after the piercing of the bubble, it is stated earlier that the jet current of the surrounding fluid gradually disappears after the development of a pair of vortices around the bubble ring. The pair vortices are observable in figure 5.34 (a) and (b) at the sides of the bubble interface. However, the development of these vortices depends on the domain confinement. In smaller confinement ratios, the vortices are formed right after the bubble is torn from the center (not shown here), but the formation of vortices are delayed in time for larger confinement ratios. Thus, it is observed in figure 5.34 that for (a) and (b) cases, the vortices are developed and the upward jet current disappears, but the upward jet current passing through the pierced region still exists for (c) and (d) cases. It should be noted that the development of pair vortices around the bubble ring is accompanied by the formation of other vortices beneath the bubble ring. Considering the wall shear stress, its magnitude dramatically increases with decrements of confinement ratio. This represents the effect of side walls on the flow of the surrounding fluid that affects the bubble shape and vertical rise velocity and also the magnitude of Electro-capillary number in which the bubble pierces. Since all the cases are pierced, the maximum values of wall shear stress for all the confinement ratios are in the same location which corresponds to the centroid of the bubble ring. Moreover, it is found that the existence of pair vortices around the bubble ring for $Cr = 2$ and 3 cases generates negative magnitudes of shear stress on the side wall.

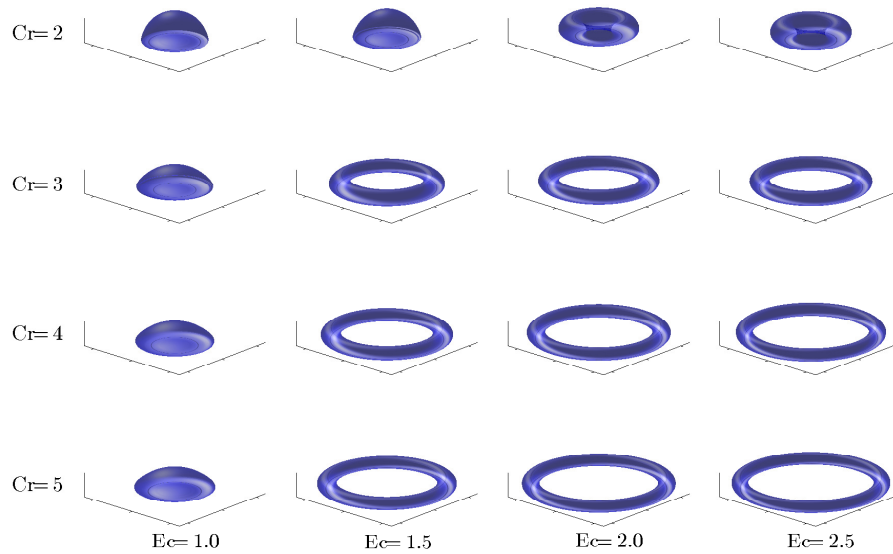


FIGURE 5.35: Three-dimensional demonstration of terminal bubble shape for variations of Electro-capillary numbers and confinement ratios.

5.2.2.4 The combined effect of confinement ratio and Electro-capillary number

Figure 5.35 represents the terminal shapes of bubbles in 3D for different confinement ratios and Electro-capillary numbers at $t = 10$. For Electro-capillary number of $Ec = 1.0$, the bubble remains non-pierced for all confinement cases and increments of confinement ratio make the bubble shape flattened. For $Ec = 1.5$, the bubble keeps its hemispherical shape in $Cr = 2$, but the bubble is torn when the confinement ratio is increased to $Cr = 3$. The toroidal shape of the bubble horizontally spreads as the confinement ratio increases to $Cr = 4$ and 5 . Considering larger magnitudes of Electro-capillary number $Ec = 2.0$ and 2.5 , it is observed that the final bubble shape for all confinement ratios is toroidal.

It has shown earlier that both confinement ratio and Electro-capillary number affect the bubble rising regime and have direct influence on the formation of a toroidal bubble (refer to figures 5.32 and 5.28, respectively). In order to determine the region where the bubble is pierced, a set of simulations in different Electro-capillary numbers and confinement ratios are carried out and the corresponding results are shown in figure 5.36. For four different confinement ratios, various Electro-capillary cases are simulated and the final state of the bubble is

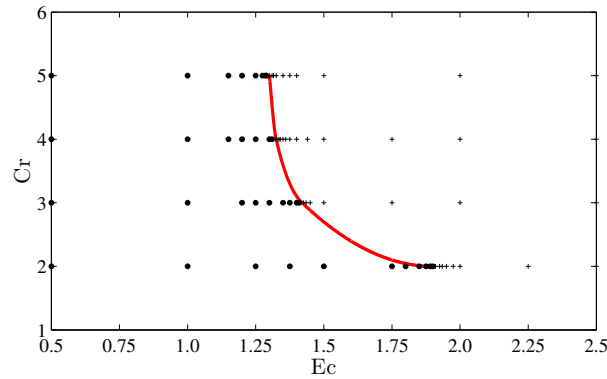


FIGURE 5.36: The map of the test cases for variations of Electro-capillary numbers and confinement ratios simulated in present study; the circle marks indicate the cases wherein the rising bubble remains non-pierced while the plus marks represent the pierced cases. The red solid line indicates the transition region where the bubble pierces.

indicated by circle and plus marks for the non-pierced and pierced cases, respectively. Moreover, a solid line determines where the bubble shape transforms into a toroidal shape as the Electro-capillary number increases. It is seen that in large confinement ratios $Cr = 5$, $Ec \approx 1.3$ is the threshold value in which a toroidal bubble is formed. This threshold does not change considerably when the confinement ratio of $Cr = 4$ is interested. Since the wall effects resist against the formation of toroidal bubble shape, the threshold increases when the confinement ratio falls below $Cr = 4$. Relatively large magnitude of Electro-capillary number $Ec \approx 1.9$ is required for $Cr = 2$ to make the bubble form a toroidal shape.

Figure 5.37 represents the terminal Reynolds number Re^* for different confinement ratios in variations of Electro-capillary number. It is stated earlier in figure 5.30 that when the bubble is pierced, the vertical rise velocity and consequently, the terminal Reynold number decreases considerably. Considering the terminal Reynolds number in two spectra of Electro-capillary number - $Ec < 1.25$ for non-pierced bubbles and $Ec > 1.85$ for toroidal bubbles - the terminal Reynolds number increases by incrementing the confinement ratio due to the effects of side boundary on the vertical rise velocity of the bubble. Moreover, by noticing the trend of terminal Reynolds number before the formation of the toroidal bubbles, it is observed that increments of Electro-capillary number lead to a slight increase in the vertical rise velocity and consequently, the terminal Reynolds number for all confinement ratios. As it has been stated earlier, it is due to the formation of electric forces on the interface of the bubble which leads to a faster rise of the

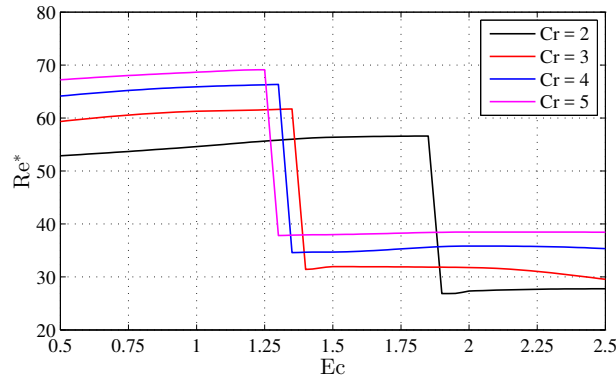


FIGURE 5.37: Variations of Terminal Reynolds number as a function of Electro-capillary number for different confinement ratios.

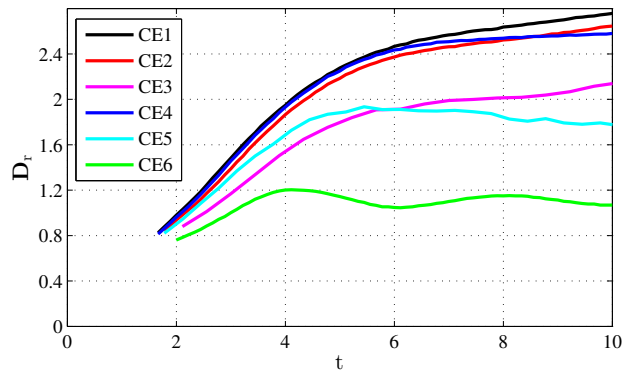


FIGURE 5.38: The variations of normalized diameter of the bubble ring D_r in time for CE1 [Cr = 5, Ec = 2.5], CE2 [Cr = 5, Ec = 2], CE3 [Cr = 5, Ec = 1.5], CE4 [Cr = 4, Ec = 2.5], CE5 [Cr = 3, Ec = 2.5], and CE6 [Cr = 2, Ec = 2.5].

bubble in larger electric field strengths. After the formation of the toroidal bubble, however, increase in the Electro-capillary number does not influence the trend of terminal Reynolds number considerably. This indicates that the electric forces do not have a significant impact on the vertical rise velocity of the bubble after the formation of the toroidal shape.

Figure 5.38 presents the variations of normalized diameter of the bubble ring D_r versus time after the bubble is pierced for some test cases in this study. The D_r is defined as the magnitude of the toroidal bubble diameter divided by the initial bubble diameter. The trend of D_r consists of two sections, one which has a steep slope showing the second transient stage of the bubble, and the other with a gentle slope indicating that the toroidal bubble gradually reaches its terminal state. During the second transient stage of rising, the toroid expands circumferentially and the bubble ring approaches the side boundary. This is due to the direction of the flow field of the surrounding fluid around the bubble that directs from the

inner region of the bubble ring towards the side boundary. The flow field of the surrounding fluid around the bubble ring is motivated by the upward jet current, and can be seen in figure 5.34 (d). It is observed that the pair vortices at the sides of the bubble ring develop leading to the gradual disappearance of the upward jet current. Considering the pair vortices, the vortex in the outer side of the bubble ring is found to be effective on the expansion of the bubble ring during the second transient stage. However, the expansion is ceased by the gradual strengthening of the inner vortex during the bubble rise, which is a turning point in the trend of the normalized diameter. Afterwards, the toroidal bubble reaches a plateau where the change in the normalized diameter is quite negligible. Since the development of the pair vortices around the bubble ring occurs earlier in time in smaller confinement ratios, reaching the plateau happens earlier for CE5 and CE6 cases. It should be noted that some oscillations are seen in the pattern of normalized diameter of the bubble ring for CE5 and CE6 cases which is due to the effects of the side boundary on the formation and strength of pair vortices around the bubble ring.

5.3 Droplet coalescence

The binary coalescence occurs when two droplets merge together and form a single droplet. The coalescence phenomenon is observed both in nature and industrial applications such as formation of rain droplets [113], spray in internal engines [114, 115] and surface treatment processes [116]. Thus, the coalescence of binary droplets is broadly investigated in experimental [117, 118] and numerical [119, 120] studies.

The coalescence of binary droplets was initially investigated on the collision of water droplets [113, 117, 118]. Brazier *et al.* [113] realized that three regimes of coalescence exist under different experiment conditions: (i) permanent coalescence (CP), (ii) coalescence followed by separation (CS), and (iii) coalescence followed by separation and formation of satellite droplets (CD). They showed that the coalescence can be characterized by the Weber number (We) and the impact parameter (β). The impact parameter varies between 0 and 1 representing head-on to grazing coalescence, respectively. They reported that the transition between permanent coalescence and coalescence with separation occurs when Weber number exceeds a critical value. Moreover, the CS and CD regimes are promoted near head-on and grazing collisions, respectively. Later studies on hydrocarbon droplets conducted by Jiang *et al.* [114] revealed that in addition to these coalescence regimes,

there is a bouncing regime which divides the permanent coalescence into a slow coalescence regime in small We numbers and a fast coalescence regime in large We numbers. This statement has been modified by Qian *et al.* [121] who studied different regimes of binary coalescence of both water and hydrocarbon droplets. They realized that both material properties of droplets and surrounding environment as well as pressure are influential on the regimes of coalescence.

Numerical investigations of the coalescence of binary droplets was pioneered by Foote [122] who studied the bouncing effect in head-on coalescence of equal-size droplets using a Marker-and-Cell method neglecting the effects of surrounding fluid. Thereafter, the coalescence of binary droplets was simulated by different numerical methods [119, 123–126] in literature. Inamuro *et al.* [123, 127] developed the Lattice Boltzmann Method to simulate the coalescence of binary droplets within the ranges of ($20 \leq We \leq 80$) and ($0 \leq \beta \leq 0.82$) and observed three different regimes of coalescence (i.e. CP, CS and CD). Tanguy *et al.* [124] employed a Level-Set approach to simulate 2D and 3D coalescence by using the Ghost Fluid method for interfacial discontinuities for the Weber range of ($We \leq 61$). They showed their results are in a good agreement with previous data in literature, but stated that they may suffer from possible mass loss for some under-resolved regions. In order to tackle the under-resolved problem, Nikolopoulos *et al.* [125, 128] studied the head-on and head-off coalescence using the Volume-of-Fluid (VOF) method and employed the Adaptive Mesh Refinement (AMR) technique. Consequently, they succeeded to investigate the formation of satellite bubbles in high Weber numbers. Within the framework of particle methods, the coalescence of binary droplets was simulated as a single phase collision of two separate droplets in vacuum by Yang *et al.* [129] and Melean [126], but no multiphase simulation of the coalescence of binary droplets is carried out in literature, to date, which is one of the important novelties of this study.

On the other hand, It is observed in some other studies in literature [130, 131] that a film of the surrounding fluid exists between the colliding droplets both in 2D and 3D simulations. The authors of present study also observed the same issue in primary simulations of binary coalescence which require a remedy to drain out the existing film from the contact surface of droplets. In order to drain out the thin film between the bubble interfaces, the film drainage model was developed [132, 133] based on the lubrication theory. Various theoretical studies [134–137] have been carried out on the development of the film drainage model. Klaseboer *et al.* [137] experimented and mathematically modeled the drainage of thin liquid film between two spherical bubbles. They compared two different assumptions, namely

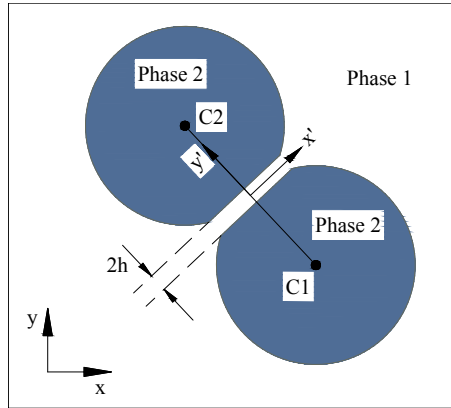


FIGURE 5.39: The schematic representation of bubble position and

the immobile interfaces and mobile interfaces assumptions by measuring the film thickness and thinning rate of the film, and concluded that the immobile interfaces assumption shows more accurate results. The experimental and theoretical developments in the framework of lubrication theory and film drainage model has been reviewed by Chan *et al.* [138] where more interested readers can be referred to. The film drainage models have also been employed in many numerical simulations [139–141]. Janssen *et al.* [141], for instance, used the Boundary Integral method to simulate head-on coalescence of viscous drops with the same viscosity as the surrounding fluid, and found out that there is a difference between the buoyancy driven and external flow driven coalescence due to the difference in the internal flows inside droplets. Nonetheless, the lubrication theory and drainage model have not been employed to any particle-based methods, to the best knowledge of the authors.

5.3.1 Lubrication theory and film drainage model

In order to drain out the fluid particles from the thin film between interface of droplets, the film drainage model based on the Reynolds lubrication theory [142] can be applied. In this model which is described schematically in figure 5.39, it is assumed that the thickness of the film is sufficiently small compared to the length of the film, thus the general Navier-Stokes equation can be simplified for the flow in the film as

$$-\frac{\partial p'}{\partial x'} + \mu \frac{\partial^2 u'}{\partial y'^2} = 0. \quad (5.9)$$

In the above equation, prime superscript indicates parameters in the coalescence coordinate where its origin is at the center of the film shown in figure 5.39, and u' is the velocity component in the direction of the x' . By integrating equation 5.9 twice and considering $\frac{\partial u'}{\partial y'} = 0$ at $y' = 0$ and $u' = 0$ at $y' = h_l/2$, an explicit statement for the velocity profile in the film, u' , can be written as

$$u' = \frac{1}{2\mu_f} \frac{\partial p'}{\partial x'} [y'^2 - h_l^2], \quad (5.10)$$

where h is the half of the film thickness.

In order to implement the lubrication theory in the numerical algorithm (referring to chapter 3.1), the lubrication velocity \mathbf{u}^l is calculated based on the pressure obtained from eq. 3.22 as

$$\mathbf{u}_i^l = \lambda_l \left[\frac{1}{2\mu_i} \nabla p_i^{(n+1)} \mathbf{r}_i^l \right], \quad (5.11)$$

where λ_l is a scalar coefficient. This coefficient is a case-dependent parameter and should be adjusted based on material properties such as density and viscosity as well as flow characteristics such as approaching velocity and droplet diameter. Nonetheless, our simulations show satisfactory results for $\lambda_l \approx 0.02$ in the case of low viscous and/or small Weber numbers and $0.1 \leq \lambda_l \leq 0.2$ for high viscous and/or large Weber number cases. \mathbf{r}_i^l is the position of the particles with respect to the coalescence coordinate as described in figure 5.39. Then, the lubrication velocity is added to the final velocity in eq. 3.23. The final displacement equation 3.24 is modified by adding the lubrication velocity displacement

$$\mathbf{r}_i^{(n+1)} = \mathbf{r}_i^{(n)} + \frac{1}{2} \left(\mathbf{u}_i^{(n)} + \mathbf{u}_i^{(n+1)} \right) \Delta t + \mathbf{u}_i^l \Delta t + \delta \mathbf{r}_i^{(n)}. \quad (5.12)$$

In order to implement film drainage model, the following considerations should be made:

- The particles positions of both droplets should be stored in separate arrays and updated in each time step. This is done to track droplets and to evaluate the distance between them. This also helps to reduce the computational cost incurred due to the implementation of the film drainage model.
- At each time step, the distance between droplets, \mathcal{L} , should be calculated. This is done by finding the minimum distance between particles of one

droplet with those of the other one which is effectively the distance between droplets' interfaces.

- The film drainage model is applicable when the thickness of the film is much smaller than the droplets diameter [137]. On the other hand, the film drainage model should be applied when the particles of the surrounding fluid have enough time to be drained out. Thus, the film drainage model should be turned on when the distance between droplets are smaller than a specific threshold. It is found that $0.1 \leq \mathcal{L}/d \leq 0.12$ provides satisfactory results.
- At each time step, particles of the surrounding fluid should be checked to be inside the film. For that purpose, the distance of surrounding fluid particles with both droplets should be checked, and drainage velocity should be applied to those appropriate ones.
- The drainage velocity is applied until the distance between droplets are less than 1.5 particle spacing. Thereafter, the coalescence has been occurred and the film drainage model should be turned off, consequently.

It should be noted that since material properties of droplets are identical, interfacial and volumetric forces as well as field parameters will not be affected after coalescence. Consequently, when the droplets are coalesced, no further considerations should be made to eliminate possible numerical issues.

5.3.2 Problem Set-up

Considering the governing equations explained in chapter 2, dimensionless values are formed using the following scales

$$\begin{aligned} \mathbf{x} &= \mathbf{x}^+/d, & \rho &= \rho^+/\rho_d, & \mu &= \mu^+/\mu_d, & \mathbf{u} &= \mathbf{u}^+/(d/t^+), & t &= t^+/(d/t^+), \\ p &= p^+/\rho_d(\mathbf{u}^+)^2, & \mathcal{D} &= \rho_d/\rho_f, & \mathcal{V} &= \mu_d/\mu_f, & \mathcal{P} &= \varepsilon_d/\varepsilon_f, & \mathcal{C} &= \sigma_d/\sigma_f, \end{aligned} \quad (5.13)$$

leading to Reynolds, Weber, Electro-Weber and Electro-capillary numbers defined as

$$\text{Re} = \frac{\rho_d \mathbf{u} d}{\mu_d}, \quad \text{We} = \frac{\rho_d \mathbf{u}^2 d}{\gamma}, \quad \text{Ew} = \frac{\rho_d \mathbf{u}^2}{\varepsilon_d E_\infty^2}, \quad \text{Ec} = \frac{\text{We}}{\text{Ew}} = \frac{\varepsilon_d E_\infty^2 d}{\gamma}. \quad (5.14)$$

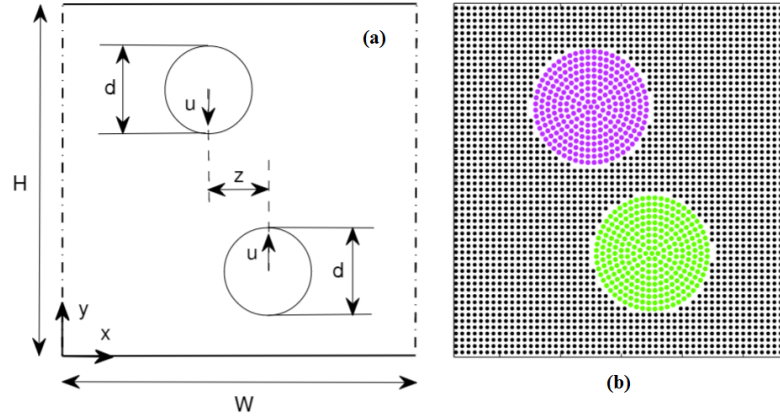


FIGURE 5.40: Schematic of the test case in sub-figure (a) and the schematic of the initial particle positions for droplets and their surrounding fluid (not full domain representation) presented with different colors in sub-figure (b).

Here, d is the bubble diameter and E_∞ is the undisturbed electric field intensity. A plus sign marks dimensional variables whereas subscripts \square_d and \square_f denote droplet and background fluid phases, respectively. The impact parameter β can be expressed as $\beta = z_d/d$ where z_d is the projection of the distance between droplet centroids, perpendicular to the direction of droplets' motion before coalescence (refer to figure 5.40 for schematic representation). In the present study, the simulations are carried out in the absence of gravity, thus \mathbf{g} is set to zero.

The schematic of the test case considered in this study is shown in figure 5.40-a. The computational domain is a rectangle with a height and a width of $H = 5d$ and $W = 5d$, respectively. The droplets are vertically placed at the initial center to center distance of $2d$ from each-other while the horizontal distance is adjusted by z to provide desirable impact parameter β . No-slip boundary condition along with a potential difference of $E_\infty = \Delta\phi/H$ is applied to top and bottom walls denoted with solid lines while the periodicity condition is implemented on the side boundaries, demarcated with dashed lines in figure 5.40. In the absence of the droplet in the computational domain, the periodic boundary condition for the electric potential produces a uniform downward electric field parallel to the side boundaries. Particles discretizing the droplet are positioned along concentric circles around the droplet's center shown in figure 5.40-b. The radii of consecutive circles differ by one particle spacing and the outermost circle's radius is equal to r . The number of particles along each of these circles vary to keep the overall inter-particle spacing uniform. Fluid particles are arranged on a uniformly spaced Cartesian grid where particles coinciding with the droplet are removed.

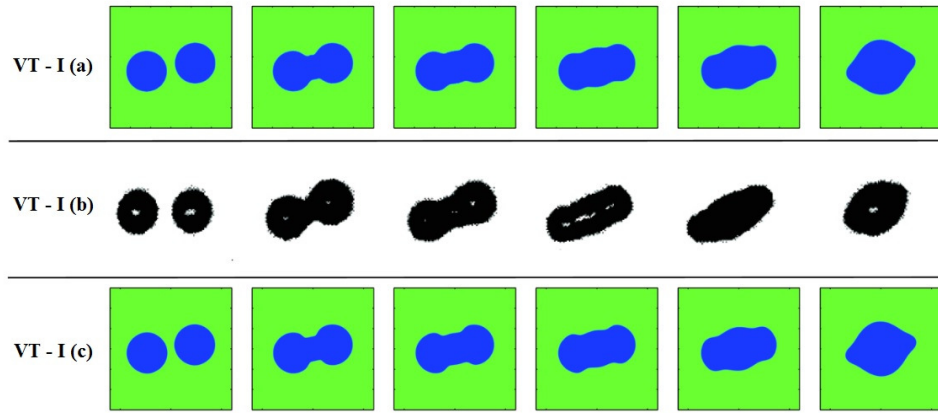


FIGURE 5.41: The comparison of the results with experimental findings of Qian *et al.* [121] and numerical findings from a FVM tool for simulation conditions $[We = 0.2, Re = 14.8, \beta = 0.20]$ at different simulation times; (a) present numerical result, (b) experimental findings, (c) FVM results.

In order to validate numerical results, the current in-house code has been extensively validated in our previous studies for numerous multiphase flow problems [13, 76, 143] including bubble dynamics and electrohydrodynamics. Nonetheless, the numerical results of two colliding droplets are validated by comparing the results with the experiments of Qian *et al.* [121] and the results of an available Finite Volume (FV) numerical tool, for two cases with different simulation conditions. The computational domain and boundary conditions of the test-cases performed with the FV tool is set identical to those of the in-house SPH code. The simulation conditions of two cases are $[We = 0.2, Re = 14.8, \beta = 0.20]$ for case VT-I and $[We = 15.2, Re = 139.8, \beta = 0.08]$ for case VT-II, while the Electro-capillary number is set to zero. Figures 5.41 and 5.42 show the coalesced droplet for some instances of the VT-I and VT-II cases, respectively. In both figures, the top, middle and bottom rows present the numerical results of the present study, experimental findings of Qian *et al.* [121] and numerical results from our FV simulations, respectively. It should be noted that in order to illustrate the results clearly, the numerical results are rotated in the post-processing stage, being aligned with the experiments direction.

The general observation reveals that both cases perfectly agree with experimental finding and FV results. For small values of Weber number shown in figure 5.41, i.e. case VT-I, numerical results are perfectly match with experimental data and FV results. The same observation is valid for large values of Weber number in figure 5.42. However, the simulation conditions of the numerical results are slightly different from those of the experimental findings. In other words, numerical results

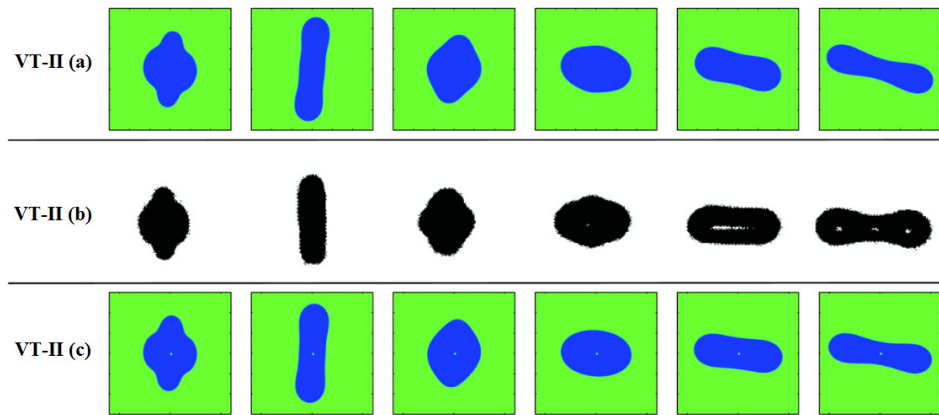


FIGURE 5.42: The comparison of the results with experimental findings of Qian *et al.* [121] and numerical findings from a FVM tool for simulation conditions [$We = 15.2, Re = 139.8, \beta = 0.08$] at different simulation times; (a) present numerical result, (b) experimental findings, (c) FVM results.

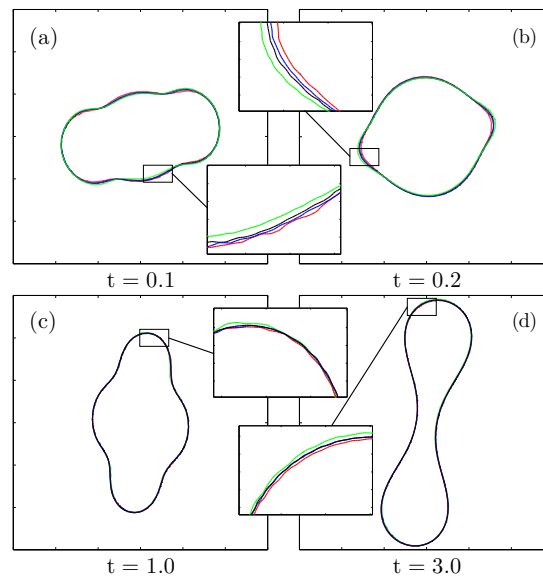


FIGURE 5.43: The particle resolution study for VT-I (sub-figures a and b) at $t = 0.1$ and $t = 0.2$, and VT-II (sub-figures c and d) at $t = 1.0$ and $t = 3.0$ for four different resolutions; $\Pi = 40 \text{ x/d}$ (green solid line), $\Pi = 50 \text{ x/d}$ (red solid line), $\Pi = 60 \text{ x/d}$ (blue solid line) and $\Pi = 70 \text{ x/d}$ (black solid line)

in VT-II are comparable with those of experiments in higher values of Weber and Reynolds numbers. This contrast arises from the difference between two-dimensional nature of present numerical simulations and three-dimensional nature of experimental findings.

The particle resolution study has been done for two different test-cases simulated for the validation, VT-I and VT-II. Figure 5.43 provides the coalesced droplet

interface at times $t = 0.1$ and $t = 0.2$ for VT-I and $t = 1.0$ and $t = 3.0$ for VT-II, respectively. The tests are performed for four different resolution cases, $\Pi = 40, 50, 60$ and 70 x/d denoted by green, red, blue and black solid lines in figure 5.43, respectively, where Π represents the number of particles per unit diameter of droplets (x/d). It is shown that for $\Pi = 60$ x/d and $\Pi = 70$ x/d , the coalesced droplet interface adequately matches. Thus, the particle resolution of $\Pi = 60$ x/d is chosen for the rest of the simulations performed in this study including the validation VT-I and VT-II test-cases, unless it is stated otherwise.

5.3.3 Binary droplet coalescence

Now, the results of binary coalescence of droplets are presented, by simulating three different sets of test-cases for head-on coalescence, head-off coalescence and electro-coalescence. In all these cases, the film drainage model is applied and represents the robustness of the proposed algorithm for simulation of different collision problems. For the inertia driven head-on and head-off coalescence in the following section, the electric potential is set to zero and the system experiences no electric force. In this part, the droplets are approaching towards each other by an initial velocity. However, for the electro-coalescence of two suspended droplet, the electric force is applied, and the initial velocity is eliminated. Thus, the flow currents generated by the electric stresses lead to the proximity of droplets which will be discussed in details.

In order to represent how film drainage model improves numerical results, figure 5.44 is presented. In this figure, the results are compared for one of the test-case simulated for head-on coalescence. In the figure, SPH particles are shown in column A for the case without the implementation of film drainage model and column B for the case with the implementation of the model. This test-case has the simulation conditions of $[We = 5.0, Re = 100, \mathcal{D} = 1000, \mathcal{V} = 100]$. In figure 5.44, two instants after the coalescence at $t = 0.15$ and $t = 0.50$ are shown where magenta and green dots are used to represent upper and lower droplets, respectively, while black dots show the surrounding fluid. For the test-cases without the implementation of the drainage model in column A, it is seen that a film of particles of surrounding fluid remains between droplet interfaces. The population of these particles is around 2 percent of the number of coalesced droplet particles which can affect the overall topology and behaviour of the coalescence. The thickness of this film is about two particles spacing and in some regions, it may be reduced to only one particle spacing. Thus, the interfacial forces such as surface tension

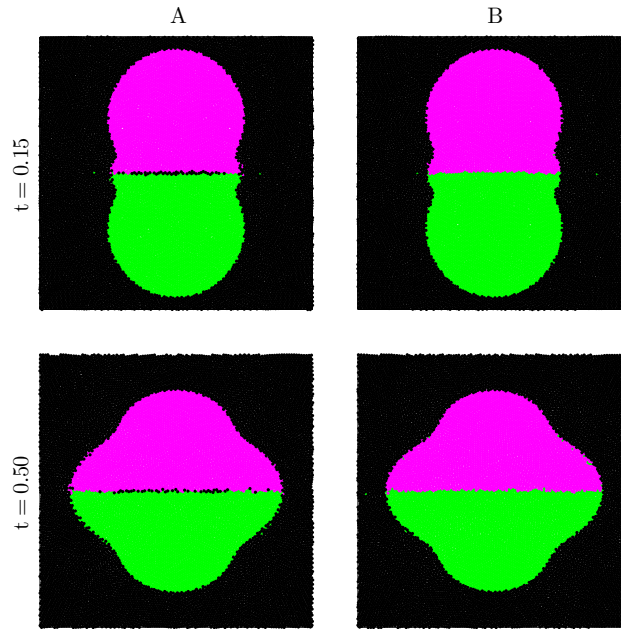


FIGURE 5.44: SPH particles of a head-on test-case with the simulation conditions of $[We = 5.0, Re = 100, \mathcal{D} = 1000, \mathcal{V} = 100]$ at two different times after coalescence for the original results (without the drainage mode) in column A, and the modified model (including the drainage model) in column B; Magenta, green and black points represent upper droplet, lower droplet and surrounding fluid particles respectively.

and electric forces are not correctly calculated in that region since the diffusive interface is four particle spacing thick. This numerical entrapment is resolved after implementation of the drainage model. It is observed that in the modified results where the drainage model is successfully applied in column B, the liquid film of surrounding fluid particles is drained out. In some cases, it is observed that individual particles of surrounding fluid will remain in the region. However, the number of these discrete particles are less than 0.2 percent of the coalesced droplet particles. These particles can be either converted to droplet particles or remain there, since they will not deteriorate the accuracy of the simulation results.

5.3.3.1 Head-on coalescence

For the simulation of head-on coalescence, seven different test-cases are selected and their simulation conditions are tabulated in table 5.8. In these cases, all simulation conditions are set to be identical but the initial approaching velocity is adjusted to maintain desired Weber number.

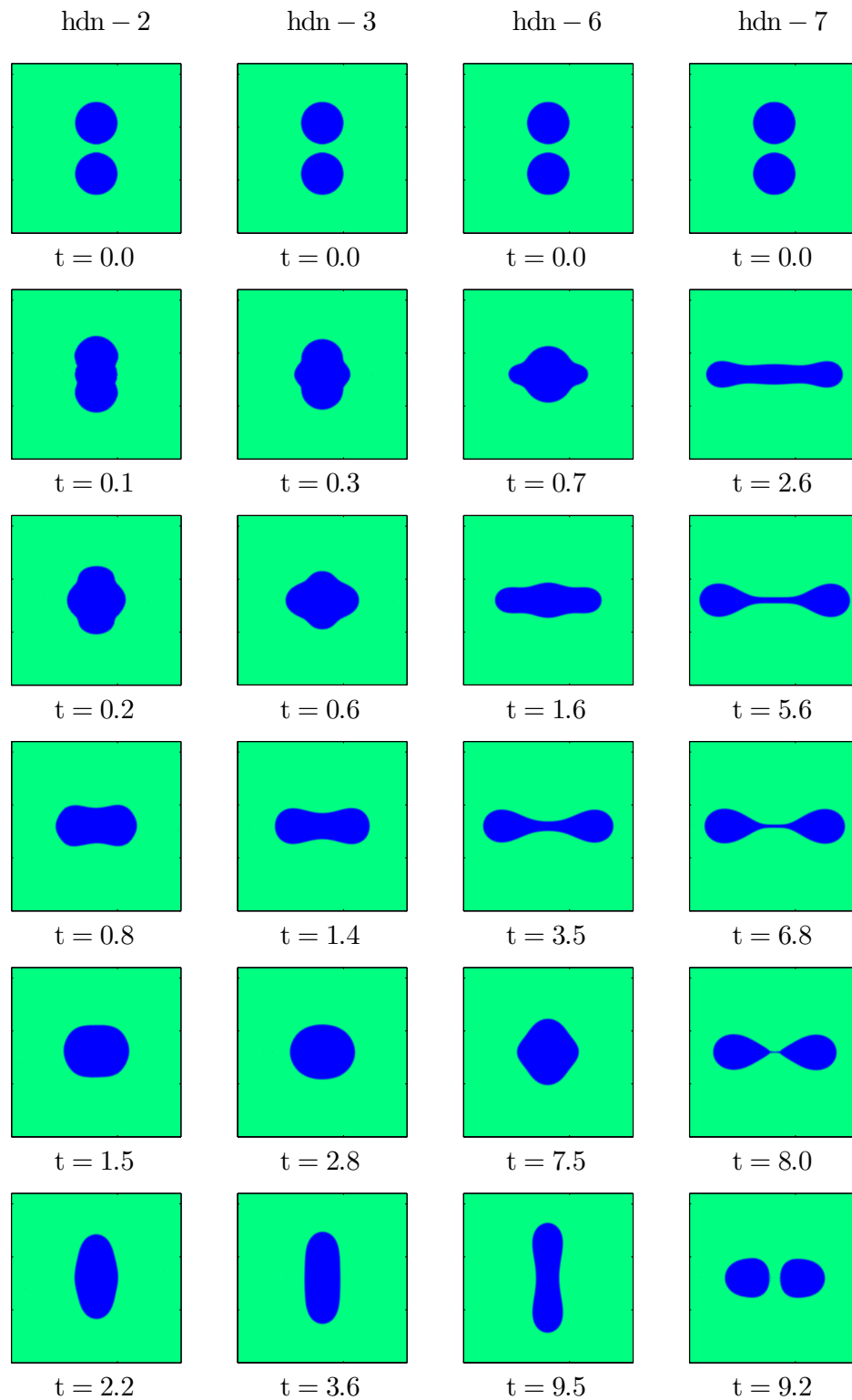


FIGURE 5.45: The evolution of head-on coalescence ($\beta = 0$) at different simulation times; The Reynolds number is set to $Re = 100$ and Weber number increase from left to right columns by $We = 2.0$, $We = 5.0$, $We = 20.0$ and $We = 30.0$.

TABLE 5.8: The magnitudes of the simulation conditions for head-on coalescence cases.

Case	We	Re	β	\mathcal{D}	\mathcal{V}
hdn-1	0.5	100	0.0	1000	100
hdn-2	2.0	100	0.0	1000	100
hdn-3	5.0	100	0.0	1000	100
hdn-4	10.0	100	0.0	1000	100
hdn-5	15.0	100	0.0	1000	100
hdn-6	20.0	100	0.0	1000	100
hdn-7	30.0	100	0.0	1000	100

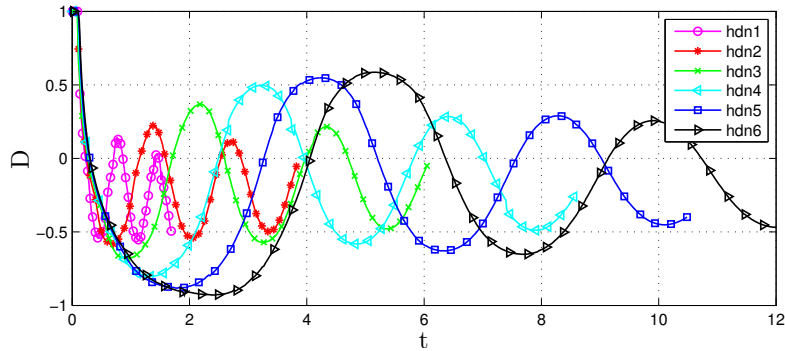


FIGURE 5.46: The variation of deformation index of coalesced droplets in time for different head-on cases shown in table 5.8.

The time evolution of head-on coalescence of two droplets is shown in figure 5.45 for four different cases from table 5.8. From the numerical point of view, the lubrication theory shows robust results for the simulation of head-on coalescence for a wide range of Weber numbers and the film drainage model perfectly drains out the liquid film from the gap between the colliding droplets. After the coalescence of droplets, two symmetric indented tips are formed at the sides of coalesced droplet which grow perpendicular to the direction of coalescence. Further growth of these indented tips leads to the formation of a hippopede, as can be seen for $We = 20.0$ at $t = 3.5$. In large Weber numbers where the inertia is relatively stronger than surface tension force, the neck of the hippopede becomes narrow and two distinguished lobes of the hippopede form an oval shape. It is observed that in $We = 30.0$, the inertial force is sufficiently strong to break the neck and form two separate droplets. On the other hand and when the Weber number is not large enough to tear apart the hippopede lobes, the surface tension force tries to balance the droplet topology and thus, the droplet undergoes an oscillatory deformation form a prolate to an oblate one. It is believed that this oscillatory motion is dissipated by viscous effects.

TABLE 5.9: The magnitudes of the simulation conditions for head-on and head-off coalescence cases.

Case	We	Re	β	\mathcal{D}	\mathcal{V}
hdf-1	10.0	100	0.05	1000	100
hdf-2	10.0	100	0.10	1000	100
hdf-3	10.0	100	0.20	1000	100
hdf-4	10.0	100	0.30	1000	100
hdf-5	10.0	100	0.40	1000	100
hdf-6	10.0	100	0.60	1000	100
hdf-7	10.0	100	0.80	1000	100

In order to quantify this oscillatory behaviour of the coalesced droplet, the deformation index is defined similar to that for the deformation of the droplet under the effect of the electric forces in previous section. Figure 5.46 shows the variation of the deformation index in time for six test cases represented in table 5.8. The oscillatory behaviour of the test cases are shown for at least two wave periods of their oscillations. The amplitude of deformation decreases for all test cases due to the viscous dissipation. This can be obtained by comparing the maximum prolate deformation in first and second periods of oscillation. For all cases, it should be also mentioned that at $t = 2.0$, the deformation index of hdn-5 and hdn-6 cases are very close to $D = -1$. This shows that the neck of the hippopede is very narrow at those times. For the case of hdn-7 (not shown here), the deformation index reaches $D = -1$, which represents that the droplet is separated into two smaller droplets.

5.3.3.2 Head-off coalescence

Similar to head-on coalescence, seven test-cases are simulated for head-off coalescence which their simulation conditions are tabulated in table 5.9. The simulation conditions of these test-cases are set identical to each-other while their impact parameter is changed for different test-cases.

Figure 5.47 represents the time evolution for four different test-cases from table 5.9. The first row of the problem illustrates the droplets at the moment of coalescence. It should be reminded that the direction of the droplets velocity is set in vertical direction and relative dislocation of droplets represent the head-off conditions of the coalescence. It is observed that the film drainage model can drain out the surrounding fluid particles between colliding droplets. At this range of simulation conditions, it is observed that all cases remain in the permanent coalescence regime

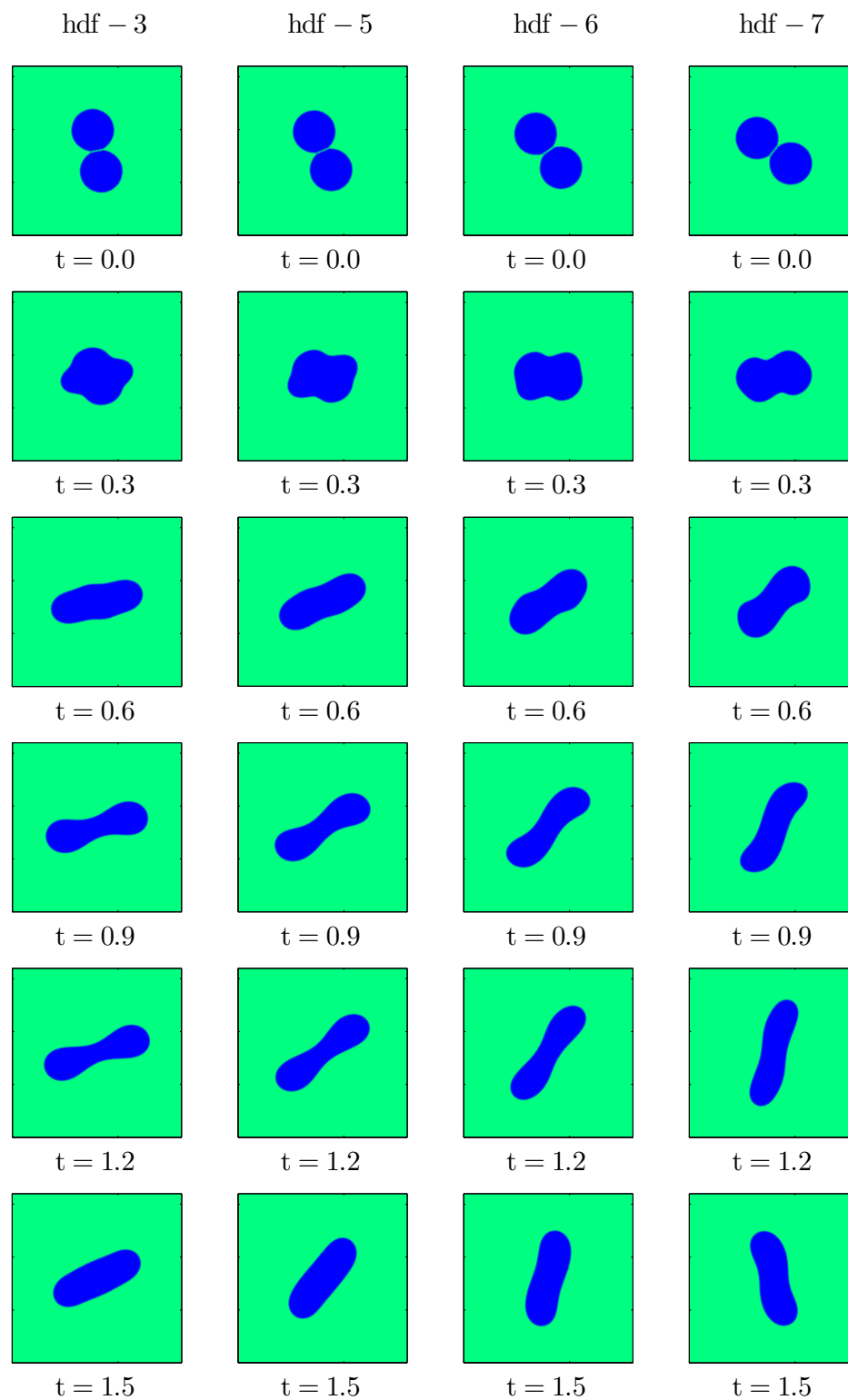


FIGURE 5.47: The evolution of head-off coalescence ($\beta = 0$) at different simulation times for four test-cases from table 5.9; The Reynolds and Weber numbers are set to $Re = 100$ and $We = 10.0$, and the impact parameter is increased from left to right, $\beta = 0.2$, $\beta = 0.4$, $\beta = 0.6$ and $\beta = 0.8$.

TABLE 5.10: The magnitudes of the simulation conditions for electro-coalescence cases.

Case	Ec	l^*	\mathcal{D}	\mathcal{V}	\mathcal{C}	\mathcal{P}
edc-1	1.0	0.25	1	1	10	0.5
edc-2	1.0	0.25	1	1	0.5	10
edc-3	0.5	0.25	1	1	10	0.5
edc-4	1.5	0.25	1	1	10	0.5
edc-5	0.5	0.25	1	1	0.5	10
edc-6	0.75	0.25	1	1	0.5	10
edc-7	1.25	0.25	1	1	0.5	10
edc-8	0.5	0.5	1	1	0.5	10
edc-9	0.75	0.5	1	1	0.5	10
edc-10	1.0	0.5	1	1	0.5	10
edc-11	1.25	0.5	1	1	0.5	10
edc-12	0.5	1.0	1	1	0.5	10
edc-13	0.75	1.0	1	1	0.5	10
edc-14	1.0	1.0	1	1	0.5	10
edc-15	1.25	1.0	1	1	0.5	10

and no satellite droplets are formed. It is observed that all coalesce droplets spin around its center of mass. For small impact parameter cases such as hdf-1 and hdf-2 (not shown in the figure), the results does not differ much from those in head-on coalescence shown in figure 5.45 for case hdn-5. However, for large values of the impact parameter, for instance for the case of hdf-7, the coalesced droplet spin faster in the simulation domain.

5.3.3.3 Electro-coalescence

The lubrication theory and the drainage model can also be applied to electro-coalescence phenomenon where two droplets collide due to the presence of an applied electric field. In order to simulate that, the initial velocity is removed and the electric field is applied to manipulate the fluid flow in the domain. Additionally, the impact parameter is set to zero to obtain head-on electro-coalescence. Thus, the characteristic parameters change and the problem is governed by other dimensionless numbers such as the Electro-capillary number. Since the initial approaching velocity is set to zero, the characteristic velocity and time are found by

$$\mathbf{u}_c = \frac{\varepsilon_d E_\infty^2 d}{\mu_d}, \quad t = t^+ / (\mathbf{u}_c / d), \quad (5.15)$$

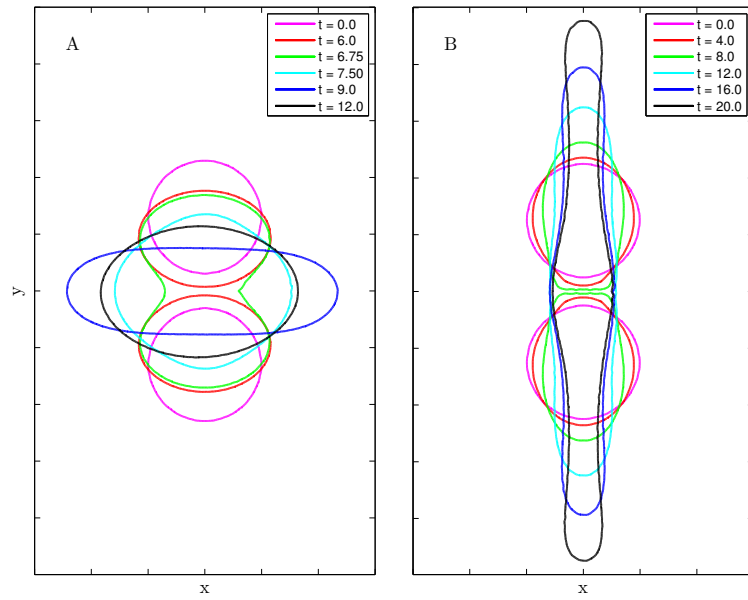


FIGURE 5.48: The time evolution of droplet interface for electro-coalescence for two different cases; (A) an oblate deformation case of droplets corresponding to edc-1 of table 5.10, and (B) a prolate deformation case corresponding to edc-2 of table 5.10.

where \mathbf{u}_c indicates the characteristic velocity.

Table 5.10 tabulates the dimensionless parameters for the electro-coalescence test-cases. In order to eliminate the viscous effects, both density and viscosity ratios are set to unity. On the other hand, permittivity and conductivity ratios are set to provide two sets of runs for oblate and prolate deformations of droplets. Another dimensionless parameter introduced here is the initial distance between droplets l^* which is normalized with respect to the droplet diameter.

Figure 5.48 shows the interface of droplets before and after coalescence for different simulation times for edc-1 and edc-2 cases of table 5.10. According to the electric permittivity and conductivity ratios and based on the analytical solution of Feng [11], it is expected that edc-1 undergoes an oblate deformation while edc-2 case deforms into a prolate shape. It is observed that both cases collide and the drainage model drains out the particles entrapped between colliding droplet interfaces. It is observed that for both cases, the droplets approach to each other due to the flow currents around the droplets. After the coalescence for the edc-1 case, and due to the action of electric forces, the coalesced droplet experiences electric forces on its interface pushing it to form an oblate shape which results in a stretching motion of the coalesced droplet seen at $t = 9.0$. This stretching motion is bounced back to

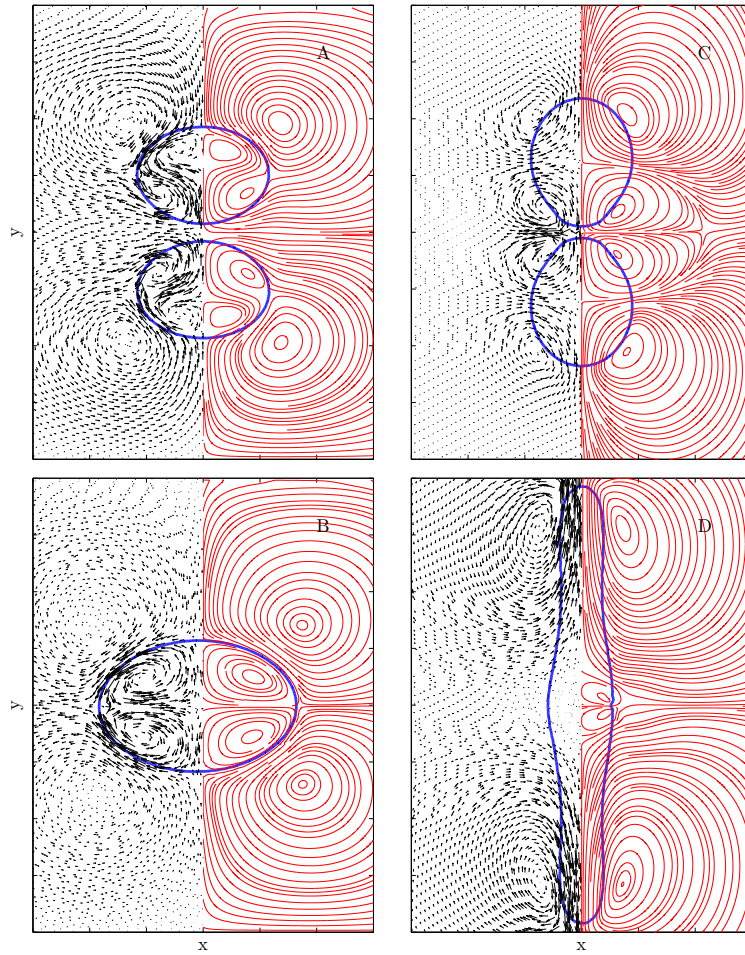


FIGURE 5.49: Droplet interface of edc-1 and edc-2 test-cases from table 5.10; velocity vectors and streamlines of particles are shown by black arrows and red lines in the left and right halves of the figure, respectively, the upper row (sub-figures A and C) represents the droplets before the coalescence and bottom row (sub-figures B and D) represents the coalesced droplet after coalescence.

balance the hydrodynamic forces such as surface tension which results in the final state of the coalesced droplet at $t = 12.0$ shown in the figure. On the other hand, the edc-2 case experience a permanent stretching motion in the vertical direction due to the formation of electric forces around the droplet.

Figure 5.49 illustrates the droplet interface and velocity vectors and streamlines, at two arbitrary times before and after coalescence for edc-1 and edc-2 cases. The edc-1 and edc-2 cases have reverse permittivity and conductivity ratios with respect to each-other leading to an oblate and a prolate formation for these cases, respectively. It is expected that the flow directions inside and around colliding droplets should be in reverse directions. This is valid for the flow motion at the

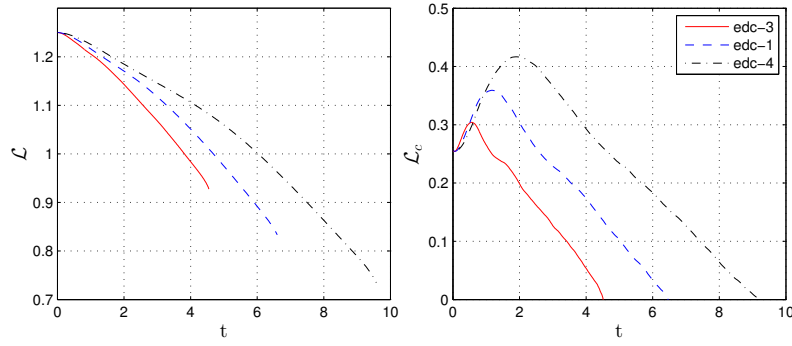


FIGURE 5.50: Comparison of droplet distance \mathcal{L} and droplet center to center distance l^* for different oblate deformation cases edc-1, edc-3 and edc-4 of table 5.10.

outer halves (rear side) of two colliding droplets in sub-figures 5.49-A and -C, but the flow motion in the inner halves (approaching side) of these droplets are in the same direction for both cases. The flow direction is a clock-wise flow in the upper-right quarter of the bottom droplet. It shows that the flow current tends to push away the surrounding fluid from the region between droplets and make both cases get closer to each other which will lead to coalescence. This flow motion is assisted by the lubrication theory and the film drainage model for a better coalescence. After permanent coalescence, the flow current inside and around the coalesced droplet has reverse direction for edc-1 and edc-2 cases.

The distance between interfaces \mathcal{L} and the center to center distance of droplets l^* are plotted in figure 5.50 for three oblate deformation cases from table 5.10. In this figure, it is observed that the center to center distance between droplets monotonically decreases for all cases which indicates the attraction of droplets due to the electrically induced flow currents around droplets. Moreover, it is observed that the case with smaller Electro-capillary number collides earlier in time and in longer center to center distances. This later conclusion is trivial since the larger the Electro-capillary number, the more deformation droplets may attain. On the other hand, the distance between droplet interfaces shows a rising trend in the early simulation time which is followed by a descending trend after reaching a vertex. The droplets are subjected to an oblate deformation when the electric field is applied at the beginning of the simulation which increases the distance between droplets. However, this turns into a decreasing trend due to the attraction of droplets resulted by electrohydrodynamic currents.

Figure 5.51 represents the distance between droplets for all prolate cases of table

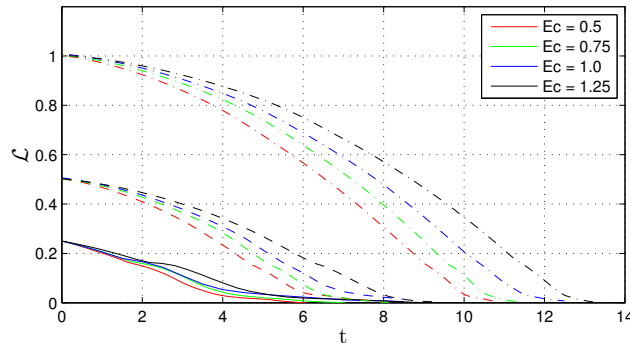


FIGURE 5.51: Comparison of droplet distance l^* for prolate deformation coalescence cases of table 5.10.

5.10. It is observed that in contrast to oblate deformation cases, it has a monotonically decreasing trend for all cases. That happens due to the fact that the direction of droplet deformation and droplet attraction due to electrohydrodynamic currents are in the same direction, in contrast to the oblate deformation cases. On the other hand, it is observed that the cases with smaller Electro-capillary numbers collide in shorter times. This is due to the definition of characteristic velocity and time, and their direct proportionality with the second power of electric field.

5.4 Electro-jet printing

The jet printing can be used in numerous applications especially in micro-scale systems ranging from soft tissue printing in biological systems [144], solar cells [145, 146] and manufacturing electronic devices [145, 147], amongst others. In the EHD jet printing, the printing quality can be controlled by means of an applied electric potential which induces the EHD forces on the fluid interface leading to the formation of a Taylor cone. This results in the deposition of a more than one order of magnitude thinner liquid film compared to the nozzle diameter. This feature makes the EHD jet printing a strong alternative for other means of jet printing methods such as piezo-type printing [148, 149], specially in practices where micro-scale diameters of deposition film is of interest.

The early investigations on the EHD jet and drop formation were carried out by Zeleny [150, 151] and later by Taylor [152]. Thereafter, many experiments have been done to examine the effect of different parameters on the Taylor cone jet and printing features. The studies of Barrero *et al.* [153], Higuera [154] and Hayati *et al.* [26, 27] are just a few examples of previous attempts to discover the

phenomenon and examine the relative importance of different physical and environmental parameters on the printing process. Barrero *et al.* [153] investigated the effects of electric conductivity and viscosity on the motion of liquid film inside the Taylor cone. They realized that there is a recirculation meridional motion induced by the tangential electric stress. The recirculation moves towards the tip of the jet along the cone surface and away from it along the axis. They also reported that the recirculation motion increases when electric conductivity and viscosity of the printing liquid decrease. Hayati *et al.* [26, 27] studied the mechanism of the stable jet formation and stated that the electric conductivity of the printing liquid has a significant impact on the phenomenon. For small magnitude of electric conductivity (insulators), little disruption is observed due to the insufficient free charges in the bulk of the fluid. On the other hand, they reported that for large magnitudes of electric conductivity (conductive materials), the printing is unstable and sparks are observed in higher electric potentials. For moderate magnitudes of electric conductivity (leaky dielectrics), however, the jet is formed for specific ranges of electric potential. Nevertheless, the complexity of the phenomenon and influence of numerous physical and environmental parameters have hindered efforts to convey a well-studied systematic approach to the problem. Yet, one of the exceptions is the experiments of Lee *et al.* [28] on the optimization and classification of the jetting modes employing a systematic approach to the problem. They constructed maps of printing regimes for different volume concentrations of a binary mixture and illustrated that how the printing pattern may change from dripping to pulsating, cone-jet, tilted jet and multi-jet, due to the variations of electric potential and injector feed rate. Experimental limitations on the selection of material properties may motivate researchers to employ numerical simulations as an available alternative for a systematic study on the EHD jet printing.

In the following, the behavior of EHD jet printing is numerically elaborated under the influence of various parameters. In the EHD jet printing, the number of dimensional parameters that influences the formation of the liquid jet is large. Therefore, a set of dimensionless groups is used to model the problem. Here, for the specific problem of interest with applications in micrometer scale, the gravitational force can be neglected while the surface tension and EHD forces are known to be the dominating forces. On the other hand, the injector inlet feed rate and fluid physical properties are the other important parameters that highlight the effect of inertial and viscous forces. Based on these set of forces, three dimensionless numbers are introduced as Reynolds number (Re), Weber number

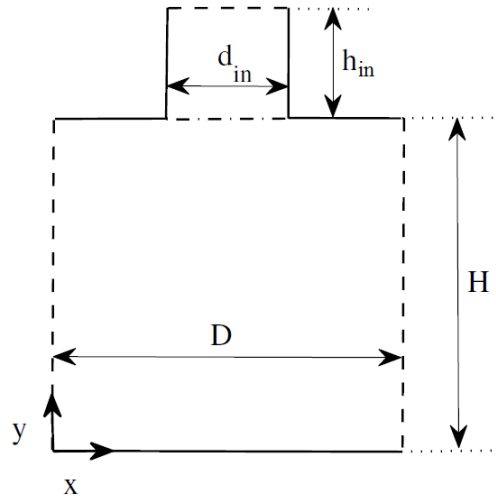


FIGURE 5.52: The schematic figure of the solution domain.

(We) and Electro-Weber number (Ew) representing the relative importance of inertia to viscous, surface tension and EHD forces, respectively.

This should be noted that the following study is carried out to provide some design criteria for the experimental setups of real-scale electro-jet printing devices. Moreover, the present study is a simplified model with respect to real-scale models and some assumptions are made here. It is known that the process is not an iso-thermal process and when the printing liquid is injected from the inlet nozzle, it solidifies due to the pressure and temperature variations. Moreover, the numerical model is simulated for a Newtonian liquid by considering a constant viscosity. However, the printing liquid is normally a non-Newtonian shear-thinning fluid in many occasions. Nonetheless, the present study tries to elaborate on the importance of electric forces on jet printing. It is believed that present model can be extended to simulating the non-Newtonian fluids, temperature-dependent properties of materials and other applications of interest such as pulsed injector printers.

5.4.1 Problem set-up

Figure 5.52 shows the schematic geometry for simulating the EHD jet printing. The domain has two regions, the nozzle (above the dash dot line) and the air chamber (below the dash dot line). The horizontal dash line represents the inlet boundary with a constant inlet velocity u_{in} of the printing liquid. The vertical dash lines are set to zero pressure outlet boundary condition. The bottom solid line is

the deposition surface while the other solid surfaces at the top of the figure represent the nozzle walls. All solid boundaries abide the no slip boundary condition but the deposition surface is a moving boundary with the velocity of $u_b = 5u_{in}$. The moving bottom boundary condition is set to avoid fluid accumulation during the printing process on the deposition surface. The electric potential is set to ϕ^+ on the inlet and nozzle boundaries, and ϕ^- on the bottom boundary. The vertical dash lines are set to no flux boundary condition for the electric potential.

The computational domain is initialized by setting the nozzle region to the printing liquid and the air chamber to the air properties, respectively. Thus, the dash-dot line represents the initial interface between the fluid phases in figure 5.52. In this study, the time step is set dynamically to keep the CourantFriedrichsLewy (CFL) condition below 0.2 ($CFL < 0.2$).

In this study, the characteristic length scale is set equal to half of the nozzle diameter $l_c = \frac{d_{in}}{2}$, so the dimensionless parameters can be represented as,

$$h = \frac{h^+}{l_c}, D = \frac{D^+}{l_c}, H = \frac{H^+}{l_c}, x = \frac{x^+}{l_c}, y = \frac{y^+}{l_c}, t = t^+ \frac{u_{in}}{l_c}, \quad (5.16)$$

where h is the nozzle height, H and D are the air chamber height and width, respectively. A plus sign represents dimensional variables and t is the simulation time and u_{in} is the inlet velocity. The star sign indicates the dimensionless variables. The injection nozzle has the height of $h_{in} = 2$, while the size of the air chamber is $D = 6$ and $H = 6$.

The EHD jet printing is a complex phenomenon and various hydrodynamic and EHD properties can affect the behaviour of the printing pattern. Thus, a systematic study is barely feasible to be carried out since many dimensional properties such as surface tension coefficient, fluid viscosity, density, electrical permittivity and conductivity, and/or controllable external parameters like applied electric field and geometrical dimensions can be influential. Moreover, if a systematic study is performed for a selection of these effective parameters, it can not be generalized for all possible combinations and scenarios. Instead, one may combine these dimensional parameters into dimensionless groups such that those dimensionless groups reflect the relative importance of different forces, thereafter the results are valid for all experiments with different dimensional combinations, if they fit in the range of those dimensionless numbers. Upon the recognition of inertia, surface tension, viscous and EHD forces as the effective forces acting on the problem, three dimensionless numbers of Reynolds (Re), Weber (We) and Electro-Weber (Ew) numbers

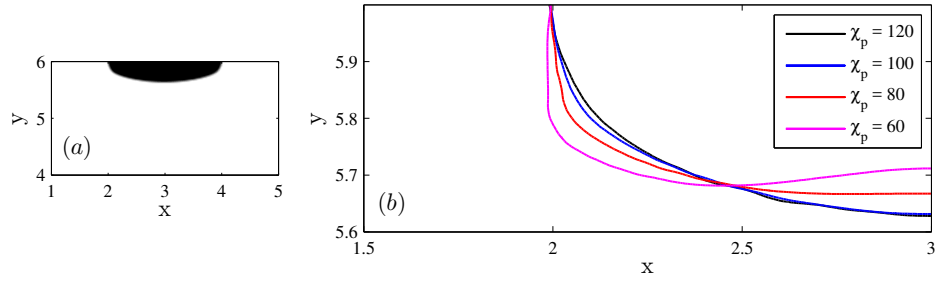


FIGURE 5.53: The grid resolution study for simulation condition of $[\text{Re} = 0.02, \text{Ew} = 300]$ at $t = 0.3$; (a) the wide view, and (b) the zoomed view of the dashed box in (a) for four different cases $\chi_p = 60$, $\chi_p = 80$, $\chi_p = 100$ and $\chi_p = 120$ which χ_p represents the number of nodes per nozzle diameter. The wide view in (a) is shown for the resolution of $\chi = 100$.

can be developed as the relative importance of inertia over viscous, inertia over surface tension and EHD over inertia, respectively. These dimensionless numbers can be shown as,

$$\text{Re} = \frac{\rho_f u_{in} d_{in}}{\mu_f}, \text{We} = \frac{\rho_f u_{in}^2 d_{in}}{\gamma}, \text{Ew} = \frac{\varepsilon_f E_\infty^2}{\rho_f u_{in}^2}, \quad (5.17)$$

where E_∞ is defined as the characteristic electric field and evaluated as $E_\infty = (\phi^+ - \phi^-)/H$. In addition to these dimensionless numbers, physical properties can be represented in their dimensionless form as,

$$\mathcal{D} = \frac{\rho_f}{\rho_g}, \mathcal{V} = \frac{\mu_f}{\mu_g}, \mathcal{P} = \frac{\varepsilon_f}{\varepsilon_g}, \mathcal{C} = \frac{\sigma_f}{\sigma_g}. \quad (5.18)$$

Here, the subscripts g and f refer to the appropriate properties of the air and printing liquid phases, respectively.

In order to check the dependency of the numerical results to the Cartesian structured mesh used in this study, a case with simulation condition of $[\text{Re} = 0.02, \text{Ew} = 300]$ is simulated under different resolution cases. Figure 5.53 represents the wide view at $t = 0.3$ in 5.53-a, and the fluid interface for four resolutions of $\chi_p = 60$, $\chi_p = 80$, $\chi_p = 100$ and $\chi_p = 120$ at that instant in 5.53-b, which χ_p represents the number of grids per nozzle diameter. The results indicate that there is a considerable difference in the results of $\chi_p = 60$, $\chi_p = 80$ and $\chi_p = 100$. But, the captured interface for the resolutions of $\chi_p = 100$ and $\chi_p = 120$ have minimal distinctions. Therefore, the resolution of $\chi_p = 100$ is used to simulate the numerical results in this study.

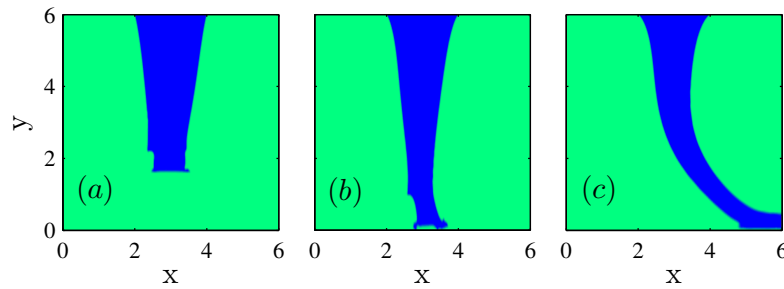


FIGURE 5.54: Instants of the printing process for simulation condition of $[\text{Re} = 0.02, \text{Ew} = 400]$ at (a) $t = 1.511$, (b) $t = 1.566$, and (c) $t = 1.593$.

5.4.2 The EHD jet printing process

In this section, the results of a printing process with respect to the variations of dimensionless numbers are presented. Thus, ratios of physical properties are set to $\mathcal{D} = 1000$, $\mathcal{V} = 50$, $\mathcal{P} = 14$ and $\mathcal{C} = 10^6$. We have performed a set of preliminary test cases to define the region where the printing is generated. It is found that the jet printing is produced in ranges of Reynolds and Electro-Weber numbers equal to $\text{Re} = 0.02 - 0.2$ and $\text{Ew} = 300 - 800$ while keeping the Weber number constant equal to $\text{We} = 0.02$. Here, It should be stated that the printing is not solely producible in the specified ranges of dimensionless numbers, and other sets of dimensionless parameters may also lead to the formation of printable jet.

Figure 5.54 shows the printing process for simulation condition of $[\text{Re} = 0.02, \text{Ew} = 400]$ at three instants of printing process, (a) $t = 1.511$, an instant before the printing jet touches the deposition surface, (b) $t = 1.566$, the touching moment, and (c) $t = 1.593$, the instant when the printing jet is formed and developed. One may intuitively expect from the jet configuration that the electric forces push the printing liquid from the sides and form a printable jet. However, the mechanism of the printing is found to be different. When the printing liquid is injected, the electric forces act on the interface from the heavier fluid towards the lighter one. Thus, the printing liquid is pulled towards the deposition surface whereby it forms a jet. According to the leaky dielectric assumption, the electrostatic relaxation time is much faster than the viscous relaxation time. Thus, the electric potential drop in the printing liquid is negligible compared to the electric potential drop in the air, knowing that the electric conductivity of the printing liquid is six order of magnitude larger than air. Therefore, the electric field in the region between the tip of the printing jet and the deposition surface becomes larger when the distance between them decreases. This results in stronger electric forces at the tip of the

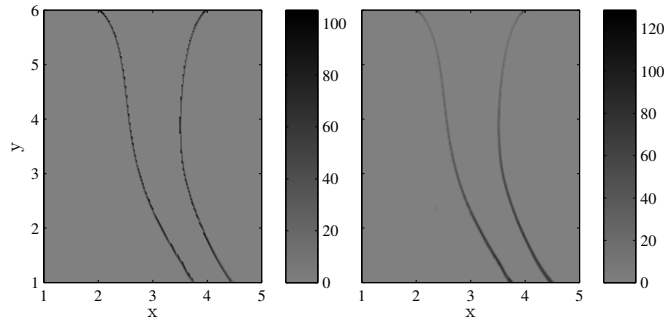


FIGURE 5.55: The surface tension force (at the left) and the electric force (at the right) for simulation condition of $[\text{Re} = 0.02, \text{Ew} = 400]$ at $t = 1.593$

printing jet at later times of printing process and before the moment when the jet touches the deposition surface.

Figure 5.55 presents the surface tension (at the left) and electric (at the right) forces per unit volume on the jet interface for the simulation condition of $[\text{Re} = 0.02, \text{Ew} = 400]$ at $t = 1.593$. The surface tension and electric forces are normalized by $\gamma/\rho_f d_{in}$ and $\varepsilon_f E_\infty^2/\rho_f d_{in}$, respectively. The direction of the surface tension force is towards the inside of the curvature of the surface while the direction of the electric forces is from the printing liquid towards the air. It is shown clearly that the electric forces are stronger on parts of the interface which is closer to the deposition surface. This is due to the existence of stronger electric field between the jet and the deposition surface, as explained before.

5.4.3 Effect of Reynolds number

Figure 5.56 shows the jet for different Reynolds numbers (a) $\text{Re} = 0.02$, (b) $\text{Re} = 0.05$, (c) $\text{Re} = 0.10$, and (d) $\text{Re} = 0.20$ at a constant Electro-Weber number of $\text{Ew} = 400$. It is observed that at a constant Electro-Weber number, with increments of Reynolds number, the jet diameter gets thinner. Since the Reynolds number scales the relative importance of inertia over viscous force, increasing the Reynolds numbers represents a system with constant inlet feed rate and less viscous printing liquid, or equivalently a system with constant viscosity and larger inlet feed rate. For the first case (more viscous printing liquid), increasing the Reynolds number is equivalent to increasing the fluidity of the printing jet. This enables the electric forces to better influence the printing liquid with a less resistive force, and consequently reducing the printing diameter when the Reynolds number is increased. Considering the second case (increasing the inlet feed rate), one may at

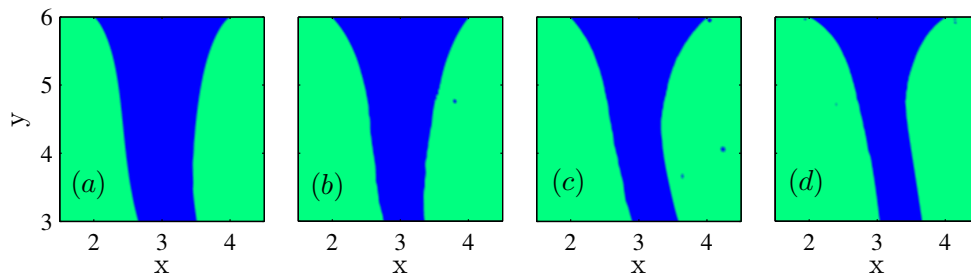


FIGURE 5.56: The variations of jet diameter for variations of Reynolds number in $Ew = 400$; (a) $Re = 0.02$, (b) $Re = 0.05$, (c) $Re = 0.10$, and (d) $Re = 0.20$.

first sight argue that the printing diameter should increase due to the injecting of larger amount of printing liquid during a given period of time. However, since the Electro-Weber number is kept constant, the electric forces should be augmented proportional to the increase in the inertial force. Therefore, the electric forces become stronger and a thinner printing jet is produced.

5.4.4 Effect of Electro-Weber number

Figure 5.57 shows the variations of jet diameter with respect to a change in Electro-Weber number from $Ew = 300$ to $Ew = 800$ at a constant Reynolds of $Re = 0.02$. It is observed that by increasing the Electro-Weber number, a thinner printing jet is produced. The reason behind this is rather straight forward and obvious since the increments of Electro-Weber number in constant Weber and Reynolds numbers enhance the dominance of electric forces over inertia, viscous and surface tension forces.

5.4.5 Unstable regimes

In some cases, when the electric potential is set large enough, the electric forces become extremely strong on the jet interface which leads to the formation of an unstable jet. Figure 5.58 shows the three unstable cases with simulation conditions of $[Re = 0.10, Ew = 600]$, $[Re = 0.10, Ew = 700]$, and $[Re = 0.10, Ew = 800]$. For these cases, the jet becomes very thin comparatively, and drippings of the printing liquid initiates before the tip of the jet touches the deposition surface. As it has been mentioned earlier, the electric forces become stronger at the tip of the jet when the distance between the jet and the deposition surface decreases. Here, prevailing over all other forces including viscous and surface tension forces,

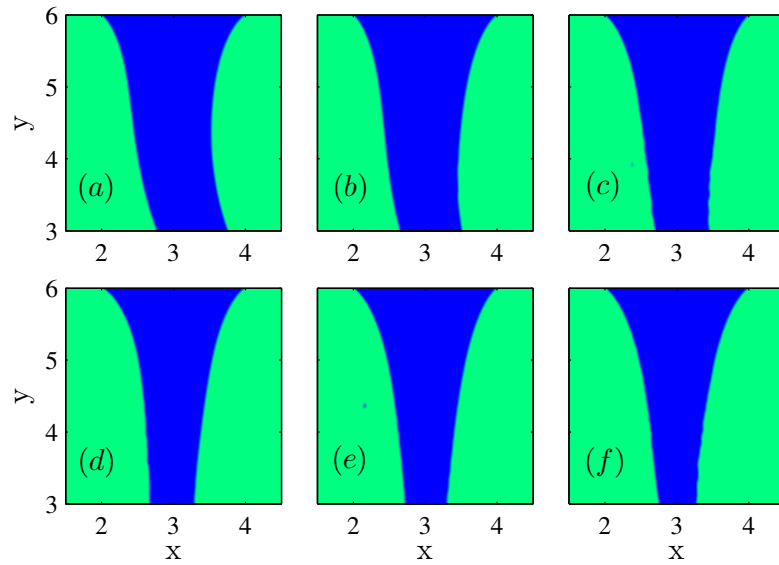


FIGURE 5.57: The variations of jet diameter for various Electro-Weber number in a $Re = 0.02$; (a) $Ew = 300$, (b) $Ew = 400$, (c) $Ew = 500$, (d) $Ew = 600$, (e) $Ew = 700$, and (f) $Ew = 800$.

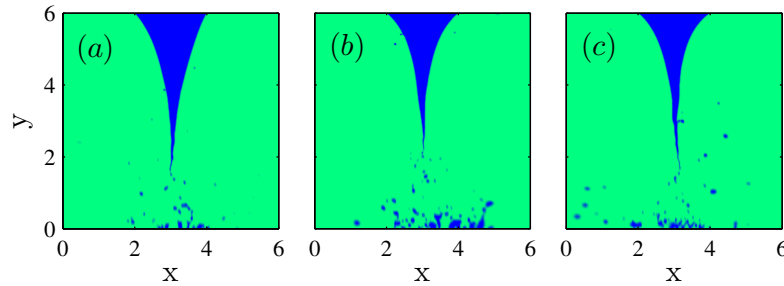


FIGURE 5.58: The unstable regimes of printing obtained for three cases, (a) $Re = 0.10$ and $Ew = 600$, (b) $Re = 0.10$ and $Ew = 700$, (c) $Re = 0.10$ and $Ew = 800$.

the induced electric force on the tip of the jet forms tiny droplets of the printing liquid. The formation of these tiny droplets is followed by the instability of the jet and hence, no printing pattern is observable.

One of the most important features of printing is the diameter of the jet. Table 5.11 shows the normalized diameter of the printing jets for variations of Re and Ew numbers. The data is shown for the full spectrum of the dimensionless numbers used in this paper. The diameter is measured at the elevation of $y = 4$ and at the moment where the printing process is completed (equivalent to figure 5.54 (c)). The results are normalized with respect to the nozzle diameter $\mathcal{S} = \frac{\delta_t}{2l_c}$, where δ_t is the dimensional measured diameter of the jet.

TABLE 5.11: The normalized jet diameter for variations of Re and Ew numbers; the Reynolds number varies from $Re = 0.02$ to $Re = 0.20$ and the Electro-Weber number varies from $Ew = 300$ to $Ew = 800$.

Ew	Re			
	0.02	0.05	0.10	0.20
300	0.521	0.497	0.488	0.421
400	0.498	0.409	0.371	0.356
500	0.464	0.349	0.310	0.235
600	0.384	0.296	0.250 \diamond	–
700	0.377	0.270	0.157 \diamond	–
800	0.364	0.224	0.131 \diamond	–

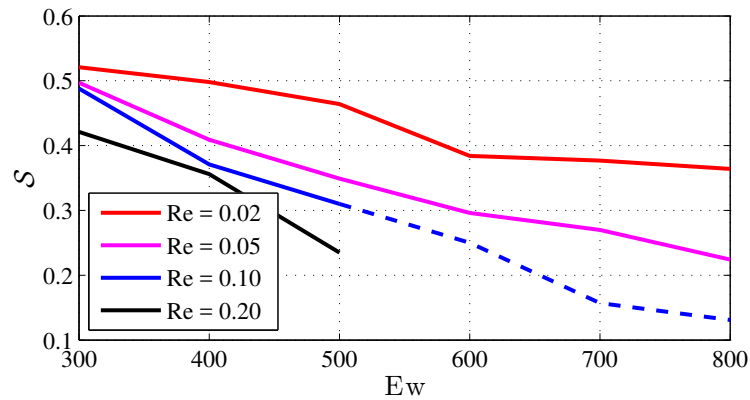


FIGURE 5.59: The normalized diameter of the measure thickness of the printing jet for variations of Ew and Re numbers.

The results presented in table 5.11 reveals that with increments of Electro-Weber number in constant Reynolds numbers, the jet diameter becomes thinner. The same observation is obtained for constant Electro-Weber numbers and increments of Reynolds number. Thus, the maximum value for the normalized diameter is equal to $\Delta = 0.521$ for $Re = 0.02$ and $Ew = 300$, and the minimum value is obtained for $\Delta = 0.224$ for $Re = 0.05$ and $Ew = 800$. The \diamond sign is used to mark those parameters for which the jet is formed but it is unstable and as a result, no film of jetting pattern is obtainable. The dash mark denotes the region where the jet is not formed and thus, no data is provided.

Figure 5.59 presents the normalized diameter of the measured thickness of the printing liquid for variations of Reynolds and Electro-Weber numbers. It is observed that by increasing the Electro-Weber number at constant Reynolds numbers, the thickness of the film is reduced. On the other hand, increasing the

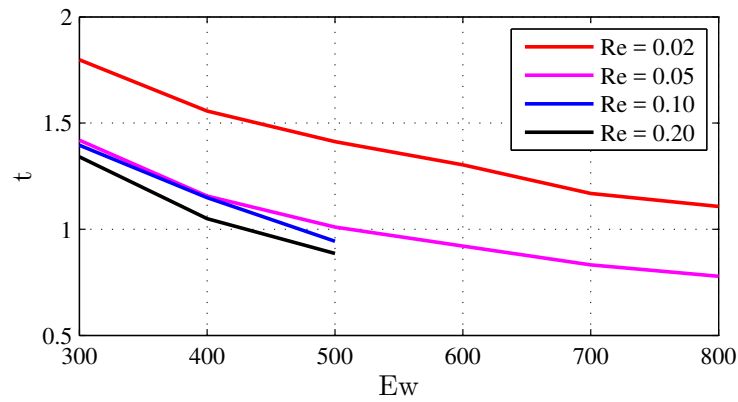


FIGURE 5.60: The dimensionless touching time for variations of Reynolds and Electro-Weber numbers.

Reynolds number for constant Electro-Weber numbers results in the formation of thinner printing film, but it may reach unstable film in some cases. Thus, the present results can be a good suggestion for the design of experimental setups for the electro-jet printing. It is suggested that the Reynolds number should be kept as small as possible for the formation of thinner printing films and desired film thickness is provided by adjusting the external electric field. moreover, it should be noted that by increasing the Reynolds number, there is the risk of formation of an unstable regimes.

Figure 5.60 represents the dimensionless time of the touching moment for different Reynolds and Electro-Weber numbers. The results show that the time of the touching moment decreases as both Reynolds and Electro-Weber numbers increase. It is explained earlier that by increasing the Reynolds number, the electric forces become stronger with the same order of the inertia forces. Hence, the electric force at the tip of the jet can pull the jet stronger towards the deposition surface, leading to reduction in the time of the touching moment. For increments of Electro-Weber number, the printing liquid is subjected to stronger electric forces in larger E_w numbers, resulting in a faster printing process.

Chapter 6

Conclusion

6.1 Concluding remarks

The present study illustrates the effects of electrohydrodynamic effects on multiphase flow problems. This is an efficient, simple and precise approach to control fluid-fluid multiphase flow problems. This approach can be applied to design industrial scale setups for a wide range of multiphase flow problems of industrial applications where the manipulation of dispersed/separated multiphase systems are of interest. In order to do that, numerical models have been developed for the simulation of multiphase flow problems under the effects of electrohydrodynamics by developing an in-house Incompressible Smoothed Particle Hydrodynamics (ISPH) code and also by writing numerical subroutines for a commercial software package named ANSYS-Fluent.

The Smoothed Particle Hydrodynamics is a meshless numerical scheme developed for the simulation of fluid flow problems. This method is widely used in literature for the simulation of various fluid flow problems such as bubble dynamics, fluid-solid interactions, free surface flows and flow instabilities amongst others. In this study, the method is extended for various problems in multiphase flow problems under the effects of electrohydrodynamics.

The surface tension force is implemented through the Continuum Surface Force model on the diffusive interface. The leaky dielectric model is employed for the implementation of electrohydrodynamics which allows finite accumulation of surface charges on the interface between fluid phases. In order to discretize the continuity

and momentum equation, a predictor-corrector algorithm is used and the pressure field is obtained by solving a pressure Poisson equation.

The ANSYS-Fluent software is a well-known package that is used to simulate fluid flow problems for a wide range of academic and industrial applications. In order to simulate dispersed multiphase flow problems, the software is equipped with the Volume of Fluid (VOF) method. The ANSYS-Fluent is capable to model numerous applications using different built-in modules, but it is not developed to simulate multiphase flows under electrohydrodynamics effects. Thus, complex User Defined Functions (UDFs) are coded and added to the main solver to serve the aforementioned purpose.

In this study, numerical results of the in-house code and the Fluent software are validated for the implementation of electrohydrodynamics by comparing with credential experimental, numerical and analytical data in literature. Additionally, they are extensively validated for various test-cases in relation to the problems of interest. These problems are the electrified Rayleigh-Taylor Instability, electrified bubble rising, electro-coalescence of binary droplets and electro-jet printing. In the following, the conclusions regarding each of these problems are discussed.

1. The Rayleigh-Taylor Instability occurs when two sheets of fluid are separated by an interface and the gravitational force is directing from the heavier fluid towards the lighter one. Thus, a perturbation on the interface generates an instability which is followed by formation of descending heavier fluid spikes and ascending lighter fluid bubbles. Depending on the direction of electric properties gradients, two different force configurations on the interface may be obtained. Several simulations have been performed for these two force configurations and results have been compared with no electric field case. In order to scrutinize the effect of the resultant electric on the instability in question, simulations have been conducted by changing the values of the electric permittivity as well as the strength of the electric field. The following comments can be made as concluding remarks

- The electric polarization force always acts normal to the interface while the electric field force is oriented in the direction of electric field. For both electric permittivity gradient cases, the polarization force is dominant wherever the interface is parallel to the growth direction of the instability, such as spike stem and side-tails. The electric field force affects the instability at spike tip providing a force in the direction of the

growth of the instability and at the bubble tip creating a force in the reverse direction to the ascent of the bubble, provided that the permittivity gradient is from heavier to lighter fluid. As for the case with the permittivity gradient vector from lighter to heavier fluid, the electric field force affects the instability at the bubble tip position providing an accordant force in the direction of bubble ascent.

- In comparison to the test case without electric force, the spike penetrates faster into the lighter fluid and the spike stem and side-tails are narrower due to the presence of polarization force in the test case with the permittivity gradient vector from heavier to lighter fluid. As for the test case with the reverse permittivity gradient vector, the spike has a slower descent and the resultant electric forces lead to a larger spike frontier and thicker spike stem and side tails. The bubble experiences resultant electric forces in the direction enhancing the rising motion of bubble. The side currents of heavier fluid approach the main stem and form a bubble entrapment, associated by secondary instabilities in the main spike stem region.
 - Increasing the value of electric permittivity and the strength of the electric field, it is observed that for the case having electric permittivity gradient vector from heavier to lighter fluid, despite having a resisting force at the bubble tips, the bubble rises faster at early time steps for higher electric force contributions. The reason for such an observation lies behind the fact that the hydrodynamic force due to replacement of lighter fluid by the heavier one as the spike descend contributes to the ascent of the bubble. Similarly, for the other case, it is expected that due to the presence of resistive electric forces at the spike tip, the spike has a slower penetration in early times for larger electric force magnitudes. However, the electric forces at the bubble region enhance the rising motion of the bubble. This provides hydrodynamic forces exerted onto the heavier fluid, resulting in faster penetration for larger electric force values at early time steps.
2. The bubble rising is simulated for an oil-water system to represent the effects of Reynolds, Bond and Electro-capillary numbers on different aspects of the bubble rising under the effects of electric forces. The final conclusion can be made as
- The general trend of bubble Aspect ratio is a linear increase to a maximum value which follows by a non-linear fashion reaching a plateau

where the electric and hydrodynamic forces balance each other. Moreover, it is found that the bubble Aspect ratio increases by incrementing electrical Capillary and Reynolds numbers, and decrementing the Bond number. Increasing the Reynolds number, the bubble response to electric forces is faster and the maximum Aspect ratio is reached earlier in time. Decrementing the Bond number, the surface tension force is stronger on bubble interface which attempts to preserve the circular bubble shape. Since the electrical Capillary number is kept constant for variations of Bond number, the electric forces are augmented as well, resulting in an increase in Aspect ratio by decrementing the Bond number.

- The study of centroid and bottom velocities of bubble for variations of electrical Capillary, Reynolds and Bond numbers reveals that the centroid velocities increase with increments of electric Capillary and Reynolds number. Increase in the Bond number yields in the increase of the centroid velocities in the transient stage, in contrast to the terminal stage. The bottom velocity is observed to be under the influence of bottom boundary and initially gets negative values for all cases showing the pulling effect of the bottom boundary. A dimensionless time scale velocity is introduced as the ratio of dielectrophoretic velocity over the hydrodynamic velocity. As this dimensionless velocity scale increases, the pulling effect of the bottom boundary is enhanced.
 - The interaction of a bubble pair shows that for vertically in-line bubbles, the distance between bubble centroids becomes smaller during the bubble rise which infers that the bottom bubble feels the pressure drop at the wake of the upper bubble. It is seen that for small values of initial center to center distance, the bubbles merge during their rise. For the cases where the bubble centroids are not initially in-line in vertical direction, however, the distance between bubble centroids increases which indicates that the bottom bubble does not feel the wake of the upper one. It is also observed that the bubbles gradually get in-line during their rising motion.
3. In order to study the effect of domain confinement and electric force on the formation of a toroidal bubble for the bubble rising, a case with the simulation conditions of $Re = 100$, $Bo = 50$, $\mathcal{D} = 0.001$, $\mathcal{V} = 0.01$, $\mathcal{C} = 0.001$, and $\mathcal{P} = 0.05$ is considered. Four confinement ratios, $Cr = 2, 3, 4$ and 5 ,

are modeled and Electro-capillary number is adjusted to consider the effect of electric forces. The concluding remarks are listed as

- It is found that both Electro-capillary number and confinement ratio are influential on the formation of the toroidal bubble. The bubble is pierced when the electric forces is sufficiently strong. The reason is that when the bubble is in the initial transient stage, the distance between the upper and bottom surfaces of the bubble decreases and then, the electric forces pierces the bubble. For smaller confinement ratios, larger Electro-capillary number is required to pierce the bubble. After the formation of a toroidal bubble, a secondary transient stage is observed. During the secondary transient stage, the vertical rise velocity of the bubble ring slightly decreases while the diameter of the bubble ring increases.
- It is observed that in all confinement ratios, the bubble terminal Reynolds number increases with enhancement of electric forces up to the state where the bubble remains non-pierced. The formation of the toroidal bubble is followed by a sudden drop of almost 50 percent in bubble vertical rise velocity. Increasing the Electro-capillary number after the bubble piercing does not have a significant influence on the terminal Reynolds number. The terminal Reynolds number increases with increments of confinement ratio both before and after the formation of the toroidal bubble.
- The study of the velocity streamlines revealed that after the formation of the toroidal bubble, a pair of vortices gently develops around the bubble ring resulting in gradual disappearance of the upward jet current. For smaller confinement ratios, the pair vortices develop right after the piercing, thus the upward jet current disappears earlier. Formation of the pair vortices results in the development of other complex vortices beneath the bubble ring.
- Considering the wall shear stress, it is found that for all confinement ratios, the wall shear stress increases with increments of the Electro-capillary number. In larger confinement ratios, the magnitude of the wall shear stress is much smaller than the smaller confinements. Negative shear stress is found in some parts of the side wall elevations due to the existence of complex vortices formed after the piercing of the bubble, especially in smaller confinement ratio cases.

4. A multiphase ISPH method is proposed based on the lubrication theory and the film drainage model to simulate droplet coalescence and electro-coalescence. Then, the method is utilized to simulate head-on and head-off coalescence, as well as the electro-coalescence for wide ranges of simulation conditions. Below, the concluding comments are provided as
 - The implementation of the film drainage model shows that the model can drain out those particles of surrounding fluid entrapped between droplet interfaces. This is done by adding a lubrication velocity to these particles when two droplets are approaching each other.
 - For the head-on and head-off coalescence, we simulated test-cases up to $We = 30$ and $0 \leq \beta \leq 0.8$. It is observed that all cases undergo permanent coalescence except for hdn-7 where the inertia is strong enough to separate the coalesced droplet into two smaller ones. For the electro-coalescence, both oblate and prolate deformed droplets are attracted to each other and permanent coalescence occurs for both types.
5. A systematic study is presented for the simulation of electro-jet printing by introducing three dimensionless numbers, Reynolds, Electro-Weber and Weber numbers. The Reynolds and Weber numbers represent the relative importance of inertia over viscous and surface tension forces, respectively, while Electro-Weber number is the ratio of electric forces over inertia. The final comments as the concluding remarks are classified as
 - The numerical findings show that the electric forces act on the interface of the printing liquid directing from the liquid towards the surrounding air. The electric forces contribute to the formation of the jet mainly by pulling the printing liquid towards the deposition surface. Since the electric relaxation time is much smaller than the viscous relaxation time, the electric potential drop in the printing liquid is observed to be negligible compared to that in the air. Thus, the electric field between the tip of the jet and the deposition surface becomes larger as the injection evolves, resulting in the formation of larger electric forces at the tip of the jet.
 - The systematic study shows that the electric diameter of the printing jet becomes narrower with the increments of Reynolds number in constant Electro-Weber numbers. By increasing the Reynolds number, the relative importance of inertia with respect to the viscous effects

is increased. Thus, in order to keep the Electro-Weber number constant, electric field needs to be adjusted. This leads to increments of electric forces on the interface which yields in the formation of a narrower printing jet. By increasing the Electro-Weber number at constant Reynolds number, the significance of electric forces over the inertia, surface tension and viscous forces increases. Thus, narrower printing jets are observed in larger Electro-Weber numbers. It is also seen that for $Re = 0.1$ and 0.2 , there is an unstable jet in Electro-Weber numbers greater than $Ew > 500$. For these cases, it is found that electric forces become so strong and drippings of the printing liquid is observed which prevents the formation of a stable printing jet.

6.2 Future works

This work represents a comprehensive study on the capabilities of the electrohydrodynamics to control numerous multiphase flow problems. However, there are many interesting and novel challenges in this field which can be tackled as future research directions. Below, possible future patterns of research are suggested as the extension of the present study, including but not limited to

1. There are numerous problems in the field of electrohydrodynamics effects which require careful investigation and development of the SPH method. Some of these problems are
 - other multiphase flow problems,
 - non-Newtonian fluids, and
 - turbulent flows.
2. Studies on three dimensional problems within the context of electrohydrodynamics multiphase flows are also novel in the field.
3. Development of new models for the simulation of electrohydrodynamics which can cover all fluid systems with different combinations of electrical properties.
4. Solution of real-world industrial problems where the electrohydrodynamics can control the physical behavior of the fluid system.

5. The performance of the present code can be improved by employing parallel-processing techniques such as GPU-based CUDA platform which can magnificently reduce the computational cost.
6. Considering the simulation of electro-jet printing, the present numerical model can be extended to non-Newtonian fluids, non iso-thermal printing process by including the solidification effects after injection, and pulsation of the inlet feed rate.

Bibliography

- [1] D. Rodrigue, D. De Kee, C. C. M. Fong, An experimental study of the effect of surfactants on the free rise velocity of gas bubbles, *Journal of Non-Newtonian Fluid Mechanics* 66 (1996) 213–232.
- [2] B. Cuenot, J. Magnaudet, B. Spennato, The effects of slightly soluble surfactants on the flow around a spherical bubble, *Journal of Fluid Mechanics* 339 (1997) 25–53.
- [3] T. L. Metcalfe, P. J. Dillon, C. D. Metcalfe, Detecting the transport of toxic pesticides from golf courses into watersheds in the precambrian shield region of ontario, canada, *Environmental Toxicology and Chemistry* 27 (2008) 811–818.
- [4] C. Zhang, S. Eckert, G. Gerbeth, Experimental study of single bubble motion in a liquid metal column exposed to a dc magnetic field, *International Journal of Multiphase Flow* 31 (2005) 824–842.
- [5] K. Ueno, T. Nishita, S. Kamiyama, Numerical simulation of deformed single bubbles rising in magnetic fluid, *Journal of Magnetism and Magnetic Materials* 201 (1999) 281–284.
- [6] C. T. O’Konski, H. C. Thacher Jr, The distortion of aerosol droplets by an electric field, *The Journal of Physical Chemistry* 57 (1953) 955–958.
- [7] C. Garton, Z. Krasucki, Bubbles in insulating liquids: stability in an electric field, in: *Proceedings of the Royal Society of London A: Mathematical, Physical and Engineering Sciences*, volume 280, The Royal Society, pp. 211–226.
- [8] G. Taylor, Studies in electrohydrodynamics. i. the circulation produced in a drop by electrical field, in: *Proceedings of the Royal Society of London A: Mathematical, Physical and Engineering Sciences*, volume 291, The Royal Society, pp. 159–166.
- [9] O. Vizika, D. Saville, The electrohydrodynamic deformation of drops suspended in liquids in steady and oscillatory electric fields, *Journal of fluid Mechanics* 239 (1992) 1–21.
- [10] S. Torza, R. Cox, S. Mason, Electrohydrodynamic deformation and burst of liquid drops, *Philosophical Transactions of the Royal Society of London A: Mathematical, Physical and Engineering Sciences* 269 (1971) 295–319.
- [11] J. Q. Feng, T. C. Scott, A computational analysis of electrohydrodynamics of a leaky dielectric drop in an electric field, *Journal of Fluid Mechanics* 311 (1996) 289–326.

- [12] J. Hua, L. K. Lim, C.-H. Wang, Numerical simulation of deformation/motion of a drop suspended in viscous liquids under influence of steady electric fields, *Physics of Fluids* (1994-present) 20 (2008) 113302.
- [13] M. Shadloo, A. Rahmat, M. Yildiz, A Smoothed Particle Hydrodynamics study on the electrohydrodynamic deformation of a droplet suspended in a neutrally buoyant Newtonian fluid, *Computational Mechanics* 52 (2013) 693–707.
- [14] J.-W. Ha, S.-M. Yang, Deformation and breakup of newtonian and non-newtonian conducting drops in an electric field, *Journal of Fluid Mechanics* 405 (2000) 131–156.
- [15] H. Paknemat, A. Pishevar, P. Pournaderi, Numerical simulation of drop deformations and breakup modes caused by direct current electric fields, *Physics of Fluids* 24 (2012) 102101.
- [16] S. D. Deshmukh, R. M. Thaokar, Deformation, breakup and motion of a perfect dielectric drop in a quadrupole electric field, *Physics of Fluids* 24 (2012) 032105.
- [17] J.-W. Ha, S.-M. Yang, Rheological responses of oil-in-oil emulsions in an electric field, *Journal of Rheology* 44 (2000) 235–256.
- [18] J.-W. Ha, S.-M. Yang, Breakup of a multiple emulsion drop in a uniform electric field, *Journal of Colloid and Interface Science* 213 (1999) 92–100.
- [19] S. Sankaran, D. Saville, Experiments on the stability of a liquid bridge in an axial electric field, *Physics of Fluids A: Fluid Dynamics* 5 (1993) 1081–1083.
- [20] C. Burcham, D. Saville, The electrohydrodynamic stability of a liquid bridge: microgravity experiments on a bridge suspended in a dielectric gas, *Journal of Fluid Mechanics* 405 (2000) 37–56.
- [21] S. Mählmann, D. T. Papageorgiou, Buoyancy-driven motion of a two-dimensional bubble or drop through a viscous liquid in the presence of a vertical electric field, *Theoretical and Computational Fluid Dynamics* 23 (2009) 375–399.
- [22] T. Wang, H. Li, Y. Zhang, D. Shi, Numerical simulation of bubble dynamics in a uniform electric field by the adaptive 3d-voset method, *Numerical Heat Transfer, Part A: Applications* 67 (2015) 1352–1369.
- [23] J. Doshi, D. H. Reneker, Electrospinning process and applications of electrospun fibers, *Journal of electrostatics* 35 (1995) 151–160.
- [24] A. Greiner, J. H. Wendorff, Electrospinning: a fascinating method for the preparation of ultrathin fibers, *Angewandte Chemie International Edition* 46 (2007) 5670–5703.
- [25] D. H. Reneker, A. L. Yarin, H. Fong, S. Koombhongse, Bending instability of electrically charged liquid jets of polymer solutions in electrospinning, *Journal of Applied physics* 87 (2000) 4531–4547.
- [26] I. Hayati, A. Bailey, T. F. Tadros, Investigations into the mechanisms of electrohydrodynamic spraying of liquids: I. effect of electric field and the environment on pendant drops and factors affecting the formation of stable jets and atomization, *Journal of Colloid and Interface Science* 117 (1987) 205–221.

- [27] I. Hayati, A. Bailey, T. F. Tadros, Investigations into the mechanism of electrohydrodynamic spraying of liquids: II. mechanism of stable jet formation and electrical forces acting on a liquid cone, *Journal of colloid and interface science* 117 (1987) 222–230.
- [28] A. Lee, H. Jin, H.-W. Dang, K.-H. Choi, K. H. Ahn, Optimization of experimental parameters to determine the jetting regimes in electrohydrodynamic printing, *Langmuir* 29 (2013) 13630–13639.
- [29] B. Sandefer, S. Pijl, B. Koren, Review of computational fluid dynamics for wind turbine wake aerodynamics, *Wind energy* 14 (2011) 799–819.
- [30] K. McLaren, S. Tullis, S. Ziada, Computational fluid dynamics simulation of the aerodynamics of a high solidity, small-scale vertical axis wind turbine, *Wind Energy* 15 (2012) 349–361.
- [31] T. Poinsot, S. Candel, A. Trounev, Applications of direct numerical simulation to premixed turbulent combustion, *Progress in Energy and Combustion Science* 21 (1995) 531–576.
- [32] I. R. Gran, B. F. Magnussen, A numerical study of a bluff-body stabilized diffusion flame. part 2. influence of combustion modeling and finite-rate chemistry, *Combustion Science and Technology* 119 (1996) 191–217.
- [33] B. Pouffary, R. F. Patella, J.-L. Reboud, P.-A. Lambert, Numerical simulation of 3d cavitating flows: analysis of cavitation head drop in turbomachinery, *Journal of Fluids Engineering* 130 (2008) 061301.
- [34] P. M. Congedo, C. Corre, P. Cinnella, Numerical investigation of dense-gas effects in turbomachinery, *Computers & Fluids* 49 (2011) 290–301.
- [35] J. Chauchat, M. Médale, A three-dimensional numerical model for dense granular flows based on the μ (i) rheology, *Journal of Computational Physics* 256 (2014) 696–712.
- [36] C. Khor, Z. Ariff, F. C. Ani, M. A. Mujeebu, M. Abdullah, M. Abdullah, M. Joseph, Three-dimensional numerical and experimental investigations on polymer rheology in meso-scale injection molding, *International Communications in Heat and Mass Transfer* 37 (2010) 131–139.
- [37] S. Shin, D. Juric, Modeling three-dimensional multiphase flow using a level contour reconstruction method for front tracking without connectivity, *Journal of Computational Physics* 180 (2002) 427–470.
- [38] G. Tryggvason, B. Bunner, A. Esmaeeli, D. Juric, N. Al-Rawahi, W. Tauber, J. Han, S. Nas, Y.-J. Jan, A front-tracking method for the computations of multiphase flow, *Journal of Computational Physics* 169 (2001) 708–759.
- [39] C. W. Hirt, B. D. Nichols, Volume of fluid (vof) method for the dynamics of free boundaries, *Journal of computational physics* 39 (1981) 201–225.
- [40] Y.-C. Chang, T. Hou, B. Merriman, S. Osher, A level set formulation of eulerian interface capturing methods for incompressible fluid flows, *Journal of computational Physics* 124 (1996) 449–464.

-
- [41] J. Brackbill, D. Kothe, C. Zemach, A Continuum Method for Modeling Surface-Tension, *Journal of Computational Physics* 100 (1992) 335–354.
- [42] Y. Lin, P. Skjetne, A. Carlson, A phase field model for multiphase electrohydrodynamic flow, *International Journal of Multiphase Flow* 45 (2012) 1–11.
- [43] M. S. Shadloo, M. Yildiz, Numerical Modeling of Kelvin-Helmholtz Instability Using Smoothed Particle Hydrodynamics, *International Journal for Numerical Methods in Engineering* 87 (2011) 988–1006.
- [44] M. S. Shadloo, A. Zainali, M. Yildiz, Simulation of Single Mode Rayleigh-Taylor Instability by SPH Method, *Computational Mechanics* 51 (2013) 699–715.
- [45] H. Braess, P. Wriggers, Arbitrary lagrangian eulerian finite element analysis of free surface flow, *Computer Methods in Applied Mechanics and Engineering* 190 (2000) 95–109.
- [46] K. Yokoi, A practical numerical framework for free surface flows based on clsvof method, multi-moment methods and density-scaled csf model: Numerical simulations of droplet splashing, *Journal of Computational Physics* 232 (2013) 252–271.
- [47] R. A. Gingold, J. J. Monaghan, Smoothed particle hydrodynamics: theory and application to non-spherical stars, *Monthly Notices of the Royal Astronomical Society* 181 (1977) 375–389.
- [48] J. J. Monaghan, Simulating free surface flows with SPH, *Journal of Computational Physics* 110 (1994) 399–406.
- [49] J. Monaghan, A. Kocharyan, SPH simulation of multi-phase flow, *Computer Physics Communications* 87 (1995) 225–235.
- [50] J. P. Morris, Simulating surface tension with smoothed particle hydrodynamics, *International Journal of Numerical Methods in Fluids* 33 (2000) 333–353.
- [51] A. Colagrossi, M. Landrini, Numerical simulation of interfacial flows by smoothed particle hydrodynamics, *Journal of Computational Physics* 191 (2003) 448–475.
- [52] X. Y. Hu, N. A. Adams, A multi-phase sph method for macroscopic and mesoscopic flows, *Journal of Computational Physics* 213 (2006) 844–861.
- [53] J. Monaghan, Smoothed particle hydrodynamics and its diverse applications, *Annual Review of Fluid Mechanics* 44 (2012) 323–346.
- [54] M. Liu, G. Liu, Smoothed particle hydrodynamics (sph): an overview and recent developments, *Archives of computational methods in engineering* 17 (2010) 25–76.
- [55] S. J. Cummins, M. Rudman, An sph projection method, *Journal of computational physics* 152 (1999) 584–607.
- [56] T. Breinlinger, P. Polfer, A. Hashibon, T. Kraft, Surface tension and wetting effects with smoothed particle hydrodynamics, *Journal of Computational Physics* 243 (2013) 14–27.

- [57] A. M. Tartakovsky, A. Panchenko, Pairwise force smoothed particle hydrodynamics model for multiphase flow: surface tension and contact line dynamics, *Journal of Computational Physics* 305 (2016) 1119–1146.
- [58] C. Peng, G. Xu, W. Wu, H.-s. Yu, C. Wang, Multiphase sph modeling of free surface flow in porous media with variable porosity, *Computers and Geotechnics* 81 (2017) 239–248.
- [59] D. W. Holmes, J. R. Williams, P. Tilke, Smooth particle hydrodynamics simulations of low reynolds number flows through porous media, *International Journal for Numerical and Analytical Methods in Geomechanics* 35 (2011) 419–437.
- [60] A. Farrokhpanah, M. Bussmann, J. Mostaghimi, New smoothed particle hydrodynamics (sph) formulation for modeling heat conduction with solidification and melting, *Numerical Heat Transfer, Part B: Fundamentals* (2017) 1–14.
- [61] K. Szewc, J. Pozorski, J.-P. Minier, Simulations of single bubbles rising through viscous liquids using smoothed particle hydrodynamics, *International Journal of Multiphase Flow* 50 (2013) 98–105.
- [62] M. Shadloo, G. Oger, D. Le Touzé, Smoothed particle hydrodynamics method for fluid flows, towards industrial applications: Motivations, current state, and challenges, *Computers & Fluids* 136 (2016) 11–34.
- [63] L. Chen, S. V. Garimella, J. A. Reizes, E. Leonardi, The development of a bubble rising in a viscous liquid, *Journal of Fluid Mechanics* 387 (1999) 61–96.
- [64] T. Bonometti, J. Magnaudet, Transition from spherical cap to toroidal bubbles, *Physics of Fluids (1994-present)* 18 (2006) 052102.
- [65] J. Hua, J. Lou, Numerical simulation of bubble rising in viscous liquid, *Journal of Computational Physics* 222 (2007) 769–795.
- [66] A. Zainali, N. Tofghi, M. S. Shadloo, M. Yildiz, Numerical Investigation of Newtonian and non-Newtonian Multiphase Flows Using ISPH Method, *Computer Methods in Applied Mechanics and Engineering* 254 (2013) 99–113.
- [67] M. Sussman, P. Smereka, S. Osher, A level set approach for computing solutions to incompressible two-phase flow, *Journal of Computational physics* 114 (1994) 146–159.
- [68] M. Shadloo, A. Zainali, M. Yildiz, Simulation of single mode rayleigh–taylor instability by sph method, *Computational Mechanics* (2012) 1–17.
- [69] A. Zainali, N. Tofghi, M. Shadloo, M. Yildiz, Numerical investigation of newtonian and non-newtonian multiphase flows using isph method, *Computer Methods in Applied Mechanics and Engineering* 254 (2013) 99–113.
- [70] D. Saville, Electrohydrodynamics: the taylor-melcher leaky dielectric model, *Annual review of fluid mechanics* 29 (1997) 27–64.
- [71] J. Melcher, G. Taylor, Electrohydrodynamics: a review of the role of interfacial shear stresses, *Annual Review of Fluid Mechanics* 1 (1969) 111–146.

- [72] L. B. Lucy, A numerical approach to the testing of the fission hypothesis, *The Astronomical Journal* 82 (1977) 1013–1024.
- [73] J. J. Monaghan, Smoothed particle hydrodynamics, *Reports on Progress in Physics* 68 (2005) 1703.
- [74] M. B. Liu, G. R. Liu, Smoothed particle hydrodynamics (sph): an overview and recent developments, *Archives of Computational Methods in Engineering* 17 (2010) 25–76.
- [75] N. Tofghi, M. Yildiz, Numerical simulation of single droplet dynamics in three-phase flows using ISPH, *Computers and Mathematics with Applications* 66 (2013) 525–536.
- [76] A. Zainali, N. Tofghi, M. S. Shadloo, M. Yildiz, Numerical investigation of Newtonian and non-Newtonian multiphase flows using ISPH method, *Computer Methods in Applied Mechanics and Engineering* 254 (2013) 99–113.
- [77] R. I. Issa, Solution of the implicitly discretised fluid flow equations by operator-splitting, *Journal of computational physics* 62 (1986) 40–65.
- [78] S. V. Patankar, D. B. Spalding, A calculation procedure for heat, mass and momentum transfer in three-dimensional parabolic flows, *International journal of heat and mass transfer* 15 (1972) 1787–1806.
- [79] M. Shadloo, M. Yildiz, Numerical modeling of kelvin–helmholtz instability using smoothed particle hydrodynamics, *International Journal for Numerical Methods in Engineering* 87 (2011) 988–1006.
- [80] N. Tofghi, M. Ozbulut, A. Rahmat, J. Feng, M. Yildiz, An incompressible smoothed particle hydrodynamics method for the motion of rigid bodies in fluids, *Journal of Computational Physics* 297 (2015) 207–220.
- [81] J. Zhang, D. Y. Kwok, A 2d lattice boltzmann study on electrohydrodynamic drop deformation with the leaky dielectric theory, *Journal of Computational Physics* 206 (2005) 150–161.
- [82] D. A. Saville, Electrohydrodynamics: The Taylor-Melcher Leaky Dielectric Model, *Annual Review of Fluid Mechanics* 29 (1997) 27–64.
- [83] Rayleigh, Investigation of the Character of the Equilibrium of an Incompressible Heavy Fluid of Variable Density, *Proceedings of the London Mathematical Society* s1-14 (1882) 170–177.
- [84] G. Taylor, The Instability of Liquid Surfaces when Accelerated in a Direction Perpendicular to their Planes. I, *Proceedings of the Royal Society of London. Series A. Mathematical and Physical Sciences* 201 (1950) 192–196.
- [85] S. Chandrashekhar, *Hydrodynamic and Hydromagnetic Stability*, Dover Publications, New York, 1981.
- [86] K. Mikaelian, Effect of Viscosity on Rayleigh-Taylor and Richtmyer-Meshkov Instabilities, *Physical Review E* 47 (1993) 375–383.

-
- [87] V. Goncharov, Analytical Model of Nonlinear, Single-Mode, Classical Rayleigh-Taylor Instability at Arbitrary Atwood Numbers, *Physical Review Letters* 88 (2002).
- [88] S. Abarzhi, K. Nishihara, J. Glimm, Rayleigh-Taylor and Richtmyer-Meshkov Instabilities for Fluids with a Finite Density Ratio, *Physics Letters A* 317 (2003) 470–476.
- [89] M. J. Gross, J. E. Porter, Electrically Induced Convection in Dielectric Liquids, *Nature* 212 (1966) 1343–1345.
- [90] R. J. Raco, Electrically Supported Column of Liquid, *Science* 160 (1968) 311–312.
- [91] A. E. M. A. Mohamed, E. S. F. E. Shehawy, Nonlinear Electrohydrodynamic Rayleigh-Taylor Instability. Part 1. A Perpendicular Field in the Absence of Surface Charges, *Journal of Fluid Mechanics* 129 (1983) 473–494.
- [92] J. Dong, V. de Almeida, C. Tsouris, Formation of Liquid Columns on Liquid-Liquid Interfaces Under Applied Electric Fields, *Journal of Colloid and Interface Science* 242 (2001) 327–336.
- [93] A. Joshi, M. C. Radhakrishna, N. Rudraiah, Rayleigh-Taylor Instability in Dielectric Fluids, *Physics of Fluids* 22 (2010).
- [94] L. L. Barannyk, D. T. Papageorgiou, P. G. Petropoulos, Suppression of Rayleigh-Taylor Instability Using Electric Fields, *Mathematics and Computers in Simulation* 82 (2012) 1008–1016. 6th IMACS International Conference on Nonlinear Evolution Equations and Wave Phenomena - Computation and Theory, Athens, GA, MAR 23-26, 2009.
- [95] A. Tartakovsky, P. Meakin, A Smoothed Particle Hydrodynamics Model for Miscible Flow in Three-Dimensional Fractures and the Two-Dimensional Rayleigh-Taylor Instability, *Journal of Computational Physics* 207 (2005) 610–624.
- [96] X. Y. Hu, N. A. Adams, An Incompressible Multi-Phase SPH Method, *Journal of Computational Physics* 227 (2007) 264–278.
- [97] N. Grenier, M. Antuono, A. Colagrossi, D. Le Touze, B. Alessandrini, An Hamiltonian Interface SPH Formulation for Multi-Fluid and Free Surface Flows, *Journal of Computational Physics* 228 (2009) 8380–8393.
- [98] M. Yildiz, R. A. Rook, A. Suleman, SPH with the Multiple Boundary Tangent Method, *International Journal for Numerical Methods in Engineering* 77 (2009) 1416–1438.
- [99] T. Takahashi, T. Miyahara, Y. Nishizaki, Separation of oily water by bubble column., *Journal of Chemical Engineering of Japan* 12 (1979) 394–399.
- [100] A. Al-Shamrani, A. James, H. Xiao, Separation of oil from water by dissolved air flotation, *Colloids and Surfaces A: Physicochemical and Engineering Aspects* 209 (2002) 15–26.
- [101] H. Y. Yoon, S. Koshizuka, Y. Oka, Direct calculation of bubble growth, departure, and rise in nucleate pool boiling, *International Journal of Multiphase Flow* 27 (2001) 277–298.

- [102] F. Pigeonneau, Mass transfer of a rising bubble in molten glass with instantaneous oxidation–reduction reaction, *Chemical Engineering Science* 64 (2009) 3120–3129.
- [103] R. Clift, J. Grace, M. Weber, Bubbles, drops and particles, Vol. 5. Nos. 1-4, 1988 *Modelling of Three Phase Sparged Catalytic Reactors* 5 (1978).
- [104] W. Han, Z.-y. Zhang, Y.-m. Yang, H.-s. Zhang, Viscosity effects on the behavior of a rising bubble, *Journal of Hydrodynamics, Ser. B* 22 (2010) 81–89.
- [105] R. B. Fdhila, P. Duineveld, The effect of surfactant on the rise of a spherical bubble at high reynolds and peclet numbers, *Physics of Fluids* (1994-present) 8 (1996) 310–321.
- [106] D. Dey, J. Boulton-Stone, A. Emery, J. Blake, Experimental comparisons with a numerical model of surfactant effects on the burst of a single bubble, *Chemical Engineering Science* 52 (1997) 2769–2783.
- [107] E. Emmanuel, K. Hanna, C. Bazin, G. Keck, B. Clément, Y. Perrodin, Fate of glutaraldehyde in hospital wastewater and combined effects of glutaraldehyde and surfactants on aquatic organisms, *Environment International* 31 (2005) 399–406.
- [108] M. S. Korlie, A. Mukherjee, B. G. Nita, J. G. Stevens, A. D. Trubatch, P. Yecko, Modeling bubbles and droplets in magnetic fluids, *Journal of Physics: Condensed Matter* 20 (2008) 204143.
- [109] Q. Yang, B. Q. Li, J. Shao, Y. Ding, A phase field numerical study of 3d bubble rising in viscous fluids under an electric field, *International Journal of Heat and Mass Transfer* 78 (2014) 820–829.
- [110] S. Hysing, S. Turek, D. Kuzmin, N. Parolini, E. Burman, S. Ganesan, L. Tobiska, Quantitative benchmark computations of two-dimensional bubble dynamics, *International Journal for Numerical Methods in Fluids* 60 (2009) 1259–1288.
- [111] D. Bhaga, M. Weber, Bubbles in viscous liquids: shapes, wakes and velocities, *Journal of Fluid Mechanics* 105 (1981) 61–85.
- [112] P. Kumar, S. Vanka, Effects of confinement on bubble dynamics in a square duct, *International Journal of Multiphase Flow* 77 (2015) 32–47.
- [113] P. Brazier-Smith, S. Jennings, J. Latham, The interaction of falling water drops: coalescence, in: *Proceedings of the Royal Society of London A: Mathematical, Physical and Engineering Sciences*, volume 326, The Royal Society, pp. 393–408.
- [114] Y. Jiang, A. Umemura, C. Law, An experimental investigation on the collision behaviour of hydrocarbon droplets, *Journal of Fluid Mechanics* 234 (1992) 171–190.
- [115] R.-H. Chen, Diesel–diesel and diesel–ethanol drop collisions, *Applied thermal engineering* 27 (2007) 604–610.
- [116] C. Planchette, E. Lorenceau, G. Brenn, Liquid encapsulation by binary collisions of immiscible liquid drops, *Colloids and Surfaces A: Physicochemical and Engineering Aspects* 365 (2010) 89–94.

-
- [117] N. Ashgriz, J. Poo, Coalescence and separation in binary collisions of liquid drops, *Journal of Fluid Mechanics* 221 (1990) 183–204.
- [118] J. Adam, N. Lindblad, C. Hendricks, The collision, coalescence, and disruption of water droplets, *Journal of Applied Physics* 39 (1968) 5173–5180.
- [119] M. Nobari, G. Tryggvason, Numerical simulations of three-dimensional drop collisions, *AIAA journal* 34 (1996) 750–755.
- [120] K. Sun, M. Jia, T. Wang, Numerical investigation of head-on droplet collision with lattice boltzmann method, *International Journal of Heat and Mass Transfer* 58 (2013) 260–275.
- [121] J. Qian, C. Law, Regimes of coalescence and separation in droplet collision, *Journal of Fluid Mechanics* 331 (1997) 59–80.
- [122] G. B. Footte, The water drop rebound problem: dynamics of collision, *Journal of the Atmospheric Sciences* 32 (1975) 390–402.
- [123] T. Inamuro, S. Tajima, F. Ogino, Lattice boltzmann simulation of droplet collision dynamics, *International journal of heat and mass transfer* 47 (2004) 4649–4657.
- [124] S. Tanguy, A. Berlemont, Application of a level set method for simulation of droplet collisions, *International journal of multiphase flow* 31 (2005) 1015–1035.
- [125] N. Nikolopoulos, K.-S. Nikas, G. Bergeles, A numerical investigation of central binary collision of droplets, *Computers & Fluids* 38 (2009) 1191–1202.
- [126] Y. Meleán, L. D. G. Sigalotti, Coalescence of colliding van der waals liquid drops, *International Journal of Heat and Mass Transfer* 48 (2005) 4041–4061.
- [127] T. Inamuro, T. Ogata, S. Tajima, N. Konishi, A lattice boltzmann method for incompressible two-phase flows with large density differences, *Journal of Computational Physics* 198 (2004) 628–644.
- [128] N. Nikolopoulos, A. Theodorakakos, G. Bergeles, Off-centre binary collision of droplets: A numerical investigation, *International Journal of Heat and Mass Transfer* 52 (2009) 4160–4174.
- [129] X. Yang, M. Liu, S. Peng, Smoothed particle hydrodynamics modeling of viscous liquid drop without tensile instability, *Computers & Fluids* 92 (2014) 199–208.
- [130] B. Lafaurie, C. Nardone, R. Scardovelli, S. Zaleski, G. Zanetti, Modelling merging and fragmentation in multiphase flows with surfer, *Journal of Computational Physics* 113 (1994) 134–147.
- [131] X. Jiang, A. James, Numerical simulation of the head-on collision of two equal-sized drops with van der waals forces, *Journal of Engineering Mathematics* 59 (2007) 99–121.
- [132] A. Sheludko, Thin liquid films, *Advances in Colloid and Interface Science* 1 (1967) 391–464.
- [133] A. Jones, S. Wilson, The film drainage problem in droplet coalescence, *Journal of Fluid Mechanics* 87 (1978) 263–288.

- [134] S. Abid, A. Chesters, The drainage and rupture of partially-mobile films between colliding drops at constant approach velocity, *International journal of multiphase flow* 20 (1994) 613–629.
- [135] A. Saboni, C. Gourdon, A. Chesters, Drainage and rupture of partially mobile films during coalescence in liquid-liquid systems under a constant interaction force, *Journal of colloid and interface science* 175 (1995) 27–35.
- [136] E. Lizarraga-Garcia, J. Buongiorno, M. Bucci, An analytical film drainage model and breakup criterion for Taylor bubbles in slug flow in inclined round pipes, *International Journal of Multiphase Flow* 84 (2016) 46–53.
- [137] E. Klaseboer, J. P. Chevaillier, C. Gourdon, O. Masbernat, Film drainage between colliding drops at constant approach velocity: experiments and modeling, *Journal of colloid and interface science* 229 (2000) 274–285.
- [138] D. Y. Chan, E. Klaseboer, R. Manica, Film drainage and coalescence between deformable drops and bubbles, *Soft Matter* 7 (2011) 2235–2264.
- [139] M. Kwakkel, W.-P. Breugem, B. J. Boersma, Extension of a CLSVOF method for droplet-laden flows with a coalescence/breakup model, *Journal of Computational Physics* 253 (2013) 166–188.
- [140] S. B. Choi, J. S. Lee, Film drainage mechanism between two immiscible droplets, *Microfluidics and nanofluidics* 17 (2014) 675–681.
- [141] P. Janssen, P. Anderson, G. Peters, H. Meijer, Axisymmetric boundary integral simulations of film drainage between two viscous drops, *Journal of Fluid Mechanics* 567 (2006) 65–90.
- [142] L. G. Leal, *Advanced transport phenomena: fluid mechanics and convective transport processes*, Cambridge University Press, 2007.
- [143] A. Rahmat, N. Tofghi, M. Yildiz, Numerical simulation of the electrohydrodynamic effects on bubble rising using the SPH method, *International Journal of Heat and Fluid Flow* 62 (2016) 313–323.
- [144] Z. Ekemen, Z. Ahmad, E. Stride, D. Kaplan, M. Edirisinghe, Electrohydrodynamic bubbling: An alternative route to fabricate porous structures of silk fibroin based materials, *Biomacromolecules* 14 (2013) 1412–1422.
- [145] M. Singh, H. M. Haverinen, P. Dhagat, G. E. Jabbour, Inkjet printing-process and its applications, *Advanced materials* 22 (2010) 673.
- [146] N. M. Muhammad, S. Sundharam, H.-W. Dang, A. Lee, B.-H. Ryu, K.-H. Choi, Cis layer deposition through electrospray process for solar cell fabrication, *Current Applied Physics* 11 (2011) S68–S75.
- [147] J.-U. Park, M. Hardy, S. J. Kang, K. Barton, K. Adair, D. Kishore Mukhopadhyay, C. Y. Lee, M. S. Strano, A. G. Alleyne, J. G. Georgiadis, et al., High-resolution electrohydrodynamic jet printing, *Nature materials* 6 (2007) 782–789.
- [148] H. Wijshoff, The dynamics of the piezo inkjet printhead operation, *Physics reports* 491 (2010) 77–177.

-
- [149] H. T. Yudistira, V. D. Nguyen, P. Dutta, D. Byun, Flight behavior of charged droplets in electrohydrodynamic inkjet printing, *Applied Physics Letters* 96 (2010) 023503.
- [150] J. Zeleny, The electrical discharge from liquid points, and a hydrostatic method of measuring the electric intensity at their surfaces, *Physical Review* 3 (1914) 69.
- [151] J. Zeleny, Instability of electrified liquid surfaces, *Physical Review* 10 (1917) 1.
- [152] G. Taylor, Disintegration of water drops in an electric field, in: *Proceedings of the Royal Society of London A: Mathematical, Physical and Engineering Sciences*, volume 280, The Royal Society, pp. 383–397.
- [153] A. Barrero, A. Ganan-Calvo, J. Davila, A. Palacios, E. Gomez-Gonzalez, The role of the electrical conductivity and viscosity on the motions inside taylor cones, *Journal of electrostatics* 47 (1999) 13–26.
- [154] F. Higuera, Flow rate and electric current emitted by a taylor cone, *Journal of Fluid Mechanics* 484 (2003) 303–327.